3-14-2006

Assessing the Potential for Improved Scramjet Performance through Application of Electromagnetic Flow Control

Martin F. Lindsey

Assessing the Potential for Improved Scramjet Performance
Through Application of Electromagnetic Flow Control

DISSERTATION

Martin Forrester Lindsey, Major, USAF

AFIT/DS/ENY/06-05

AFIT/DS/ENY/06-05

Assessing the Potential for Improved Scramjet Performance Through Application of Electromagnetic Flow Control

DISSERTATION

Presented to the Faculty

Department of Aeronautical and Astronautical Engineering

Graduate School of Engineering and Management

Air Force Institute of Technology

Air University

Air Education and Training Command

In Partial Fulfillment of the Requirements for the

Degree of Doctor of Philosophy

Martin Forrester Lindsey, B.S., M.A.E., M.S.

Major, USAF

March 2006

ASSESSING THE POTENTIAL FOR IMPROVED SCRAMJET
PERFORMANCE THROUGH APPLICATION OF ELECTROMAGNETIC
FLOW CONTROL

Martin Forrester Lindsey, B.S., M.A.E., M.S.

Major, USAF

Approved:

Richard J. McMullan, USAF (Chairman)	14 Mar 06 — date
Kenneth W. Bauer (Dean's Representative)	14 MAR 06 — date
Paul I. King (Member)	14 Mar 06 — date
William F. Bailey (Member)	14 Mar 2006 — date
José A. Camberos (Member)	14 MAR 2006 — date

Accepted:

M. U. Thomas   14 Mar 2006
M. U. Thomas   Date
Dean, Graduate School of Engineering and Management

AFIT/DS/ENY/06-05

Abstract

Sustained hypersonic flight using scramjet propulsion is the key technology bridging the gap between turbojets and the exoatmospheric environment where a rocket is required. Recent efforts have focused on electromagnetic (EM) flow control to mitigate the problems of high thermomechanical loads and low propulsion efficiencies associated with scramjet propulsion. This research effort is the first flight-scale, three-dimensional computational analysis of a realistic scramjet to determine how EM flow control can improve scramjet performance. Development of a quasi-one dimensional design tool culminated in the first open source geometry of an entire scramjet flowpath. This geometry was then tested extensively with the Air Force Research Laboratory's three-dimensional Navier-Stokes and EM coupled computational code. As part of improving the model fidelity, a loosely coupled algorithm was developed to incorporate thermochemistry. This resulted in the only open-source model of fuel injection, mixing and combustion in a magnetogasdynamic (MGD) flow controlled engine. In addition, a control volume analysis tool with an electron beam ionization model was presented for the first time in the context of the established computational method used. Local EM flow control within the internal inlet greatly affected drag forces and wall heat transfer but was only marginally successful in raising the average pressure entering the combustor. The use of an MGD accelerator to locally increase flow momentum was an effective approach to improve flow into the scramjet's isolator. Combustor-based MGD generators proved superior to the inlet generator with respect to power density and overall engine efficiency. MGD acceleration was shown to be ineffective in improving overall performance, with all of the bypass engines having approximately 33% more drag than baseline and none of them achieving a self-powered state.

Acknowledgements

As in all things, I would like to begin by thanking God, the source of all blessings, including this opportunity. I would like to express my never ending gratitude and love for my wife for always taking care of the truly important things in life, so I could pursue this study. I would like to thank my son who always motivates me to do my best. Without even knowing it, he has always brought balance to my life, a constant reminder that I should 'maintain an even strain.' I would also like to thank my mother, father, and sister whose love and support throughout my life have sustained and equipped me to reach this point. It is to all of them that I dedicate this work.

No student succeeds without the support and mentoring of his teacher, and in this I am forever in the debt of my advisor Maj Jeff McMullan. Whenever my efforts would diverge from the goal, he would refocus me, especially when the inevitable setbacks would cause me to question my own motivation and ability. In this same manner, I would like to thank the entire research committee. Their guidance ensured the scope of this effort did not exceed my reach. While not an official member of my committee, I owe a great debt of gratitude to Dr. Datta Gaitonde, Air Force Research Laboratory, who not only provided the computational code which formed the basis of this research but also served as an invaluable source of technical advice.

I received support from several other individuals whom I would like to recognize. Lt Col Ray Maple taught me as much about CFD and the correct way to write code as anyone. Dr Ralph Anthenien literally taught me everything I know about combustion and was always ready to answer my questions. Dave Doak and Jason Speckman provided top-notch computational support for my use of the Unix cluster. Likewise, Dr Alan Minga of Cray, Inc., did the same regarding use of the Cray X1 at both the ERDC and AHPCRC. Finally, I would like to thank *ALL* of my fellow PhD students whose camaraderie and fellowship made this shared journey enjoyable.

Martin Forrester Lindsey

Table of Contents

List of Figures

List of Tables

List of Symbols

xiv

List of Abbreviations

Assessing the Potential for Improved Scramjet Performance Through Application of Electromagnetic Flow Control

I. Introduction

1.1 Scramjet Operation, Design Challenges, and a Brief History

Jet engines of all varieties depend on the compression of ambient air to provide the oxidizer needed for combustion. This is in contrast to a rocket engine which must carry its own oxidizer at a substantial vehicle performance penalty. Probably the most widely known application of a jet engine is the turbojet which relies on a compressor driven by a turbine in the engine exhaust flow to perform this function. This method is particularly efficient for subsonic and low supersonic applications and as a concept dates back to the work of Guillame in 1921 [25]. By contrast, a ramjet compresses the ambient air entirely through deceleration of the freestream flow, typically by one or more inlet shockwaves. Therefore, the ram compression process is one of conversion of freestream kinetic energy to internal energy as manifested by increased temperature, pressure, and density and lower relative Mach number. The ramjet concept is actually seven years older than the turbojet, but because a ramjet does not provide compression as efficiently at low speed flows, it wasn't until 1928 that a patent for a ramjet for supersonic flight was issued to Albert Fono of Hungary [25]. Ramjets are most efficient when operated in a freestream regime of approximately Mach 3 - 6. At speeds approaching Mach 6, the aerodynamic losses (e.g. total pressure, drag), heating, and increased structural requirements that accompany compression of the flow to subsonic combustion speeds render the ordinary ramjet excessively inefficient. Thus, to extend the airbreathing performance envelope to higher Mach numbers, supersonic combustion has been pursued.

The supersonic combustion ramjet, or scramjet, is by definition then a ramjet engine where the entire combustion process occurs under locally supersonic conditions. A typical scramjet or ramjet flowpath as shown in Figure 1.1 can be distinguished by three primary processes: compression, combustion, and expansion. First, the freestream air is compressed externally and/or internally. This is usually accomplished by a series of oblique shockwaves but may also include isentropic compression. The goal of the compression process is to attain high enough static pressure to sustain combustion while minimizing aerodynamic losses and limiting the static temperature increase. The second limitation is necessary to minimize flow energy losses due to molecular vibration and dissociation. Combustion heat release then increases the flow energy which is exchanged for an overall flow momentum increase through an expansion process, producing net positive thrust. For such a simple thermodynamic process, several formidable technical issues have precluded a scramjet-powered flight vehicle until quite recently.
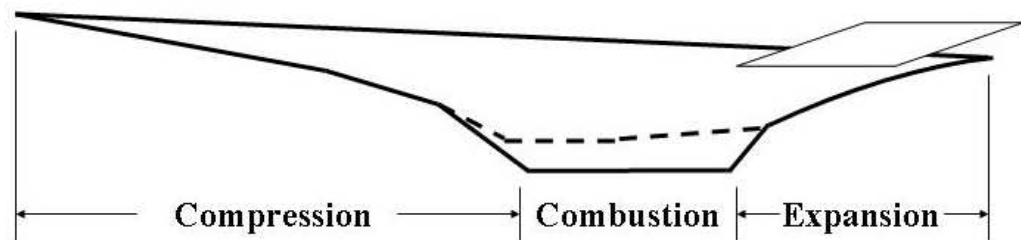
Figure 1.1:   Typical Scramjet Engine Schematic

Contrary to popular thinking, the scramjet is not a new concept but instead can trace its history back as far as the work of M.M. Roy in 1946, with Mach 3 steady combustion demonstrated as early as 1958. As early as the 1950's the major technical issues had been identified: "fuel injection and mixing without severe shock losses, combustor gasdynamic phenomena, wall cooling and frictional losses, and nozzle performance [12]." Several efforts in the United States throughout the 1960s laid the foundations to address these issues and culminated in the mid-1970s with NASA's Hypersonic Research Engine (HRE), a flightweight, hydrogen-fueled engine originally

envisioned for the X-15 program. Upon the cancellation of the X-15 program, two HRE prototypes were converted to ground test articles that throughout the 1970s established a comprehensive database on inlet and combustor performance in the low hypersonic range (Mach 5-7) [25]. Concurrent efforts by the U.S. Air Force and Navy to develop scramjets for potential missile applications came together with the HRE. Technology from the HRE evolved into the National Aerospace Plane (NASP) program of the 1980s. NASP's goal was to to develop the X-30 Single-Stage-To-Orbit vehicle which would rely on a hydrogen-fueled scramjet for operation in the Mach 4-15 range [12]. Although the NASP program produced a wealth of designs and ground test data, the X-30 was never built and by 1995 the program had been terminated due to lack of funding.

An offshoot of the NASP, NASA's X-43 program began in the late 1990s and, with its successful flight test in March 2004, currently represents the state-of-the-art in scramjet propulsion [11]. The X-43A uses a hydrogen-fueled scramjet engine which is highly integrated with the airframe. This flight demonstration vehicle is released from a B-52 and accelerated to flight test conditions by the first stage of a Pegasus expendable launch vehicle. Upon reaching these conditions, the X-43 is released from its booster and is then self-propelled by its scramjet engine. On 27 March 2004, the vehicle became the first scramjet device to demonstrate net thrust [16] and set a world speed record for airbreathing aircraft with its 11 second flight at Mach 6.83 and 100,000 feet [57]. By 16 November 2004, a second X-43A pushed the speed record even further, achieving Mach 9.6 during a 10-second burn of its engine after being "boosted to an altitude of 33,223 meters (109,000 feet) by a Pegasus rocket launched from beneath a B52-B jet aircraft." [58]

Although a great milestone has been reached with the X-43, all of the broad technical challenges quoted above remain. Of these, the greatest issues continue to be thermal control, maximizing component and system efficiencies and achieving adequate fuel mixing and combustion within typical combustor residence times measured in milliseconds. Various flow control mechanisms have been proposed, especially with
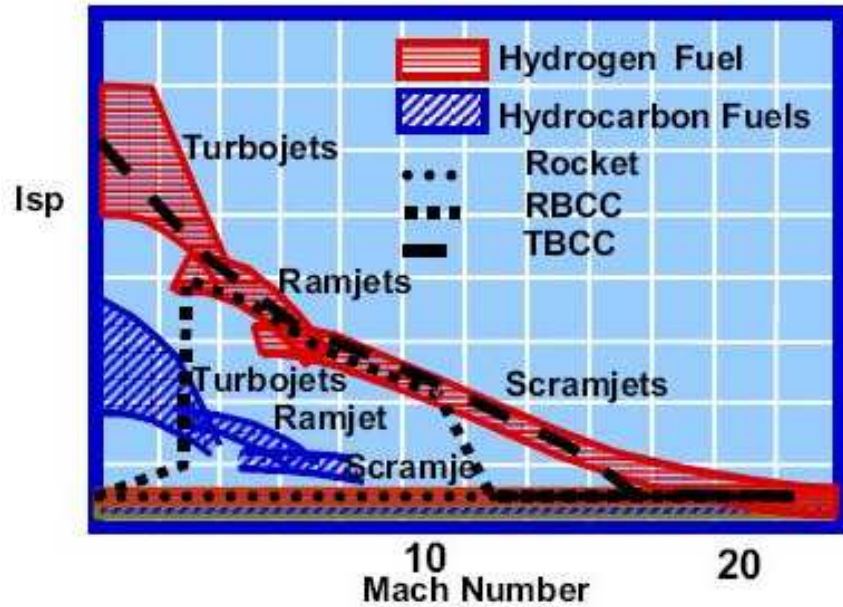
Figure 1.2:   Airbreathing Engine Performance Regimes [11]

respect to better conditioning of the flow entering the combustor. These mechanisms have had varying success which will be discussed further in Section 1.2. As a final issue, there is much uncertainty in the scaling of an X-43 type flight demonstrator into the design of an operational flight vehicle. However, as evidenced in Figure 1.2, what is certain is that the air breathing scramjet (and in particular one which is hydrogen-fueled) is the key technology to achieving sustained hypersonic cruising vehicles and affordable, on-demand access to the low earth orbit environment.

1.2   A Review of Flow Control Concepts with an Emphasis on Magnetogasdynamics

Many approaches to controlling the flow momentum and thermodynamic properties through scramjet engines have been considered over the past several decades. Most of these approaches are well known and accepted practices in the sense they have proven effective in regimes slower than the hypersonic speeds encountered by scramjets. An example of this would be the presence in the inlet of slots or other devices to bleed off some of the low momentum boundary layer flow [19] that, due

to the high area contraction ratios in scramjet inlets, tends to cause large regions of flow separation and extreme wall heating in the inlet [65]. These same devices can also be effective in lowering the overall mass flow rate into the engine to promote engine starting. The downside of this approach is a structure and drag penalty due to the bleed plenum as well as a loss of some of the freestream mass flow. In a different approach to the same issue, some experiments, including the X-43A wind tunnel models, have used boundary layer trip devices on the external compression surfaces to induce a turbulent boundary layer [6] and likewise prevent flow separation. However, turbulent flow has more drag than laminar flow, which again decreases vehicle performance. Although these examples have focused on conditioning the inlet flow, just as much if not more effort, has focused on using various geometries to control fuel mixing and combustion [4,5,15,24]. What is obvious is that all of these methods have drawbacks and thus in the past several years researchers have begun to turn towards more exotic flow control methods.

As far back as the 1960s, practical magnetogasdynamic (MGD) applications were studied in earnest, not only for terrestrial electrical power generation [70] but also for electrical propulsion and aerodynamic control [75]. Magnetogasdynamics (also referred to as magnetohydrodynamics or magnetofluidmechanics by various authors) is broadly defined by Hughes and Young in their seminal textbook as "the study of the flow of electrically conducting fluids in the presence of a magnetic field under certain special assumptions [30]." In short, the fluid flow is coupled to Maxwell's equations for electromagnetism through an electromagnetic body force known as the Lorentz Force and its associated energy interaction. This coupling is defined in detail in the equations presented in Chapter II. In the infancy of hypersonic flight, it was recognized that the air within the hypersonic shock layer surrounding the vehicle could become appreciably ionized. This fact "prompted research on methods of magnetically interacting with the flow to produce various effects, including control of drag or angle of attack, and boundary-layer control to increase the transition Reynolds number or to reduce the hypersonic heat transfer" [75]. Recent experimental and numerical research

efforts have focused on internal MGD flow control and electrical power generation (i.e. within scramjet engines) as well as the external aerodynamics, with key goals being the mitigation of the high thermomechanical loads and low propulsion efficiencies typical of the examples described in the previous paragraph.

These recent MGD flow control efforts have ranged from basic scientific exploration of the concept to simple analytical and experimental applications. A good example of the former is the MGD flow characterization conducted in the Mach 3 and Mach 4 plasma tunnels at The Ohio State University (OSU) [53, 55, 59]. These experiments are investigating basic unit problems specifically relevant to MGD flow control by exploring three-dimensional supersonic flow in a channel. Specific work at this facility has sought to attain and characterize a sustainable, non-equilibrium plasma. Various approaches using high intensity radio frequency (RF) discharges have been taken to accomplish this ionization. Flowing nitrogen at Mach 3 through a 3-cm wide test section, a sustained RF discharge at 1kW was capable of achieving a conductivity of 0.24mho/m in the presence of a magnetic field of 1.5 Tesla (T). From the standpoint of required ionization power, a more efficient approach demonstrated a pulsed-RF signal with a 20ns duration and 40kHz repetition rate with a peak power approaching 1MW. When combined with a sustaining direct current electric field, both air and nitrogen Mach 4 flows produced uniform, stable plasmas with conductivities of 0.09mho/m and 0.18mho/m, respectively.

Complementing this basic scientific exploration, a significant amount of analytical work exists with respect to both creating/sustaining a non-equilibrium plasma as well as putting this plasma to work through MGD interaction. However, it should be immediately noted that in order to make most practical analytical problems tractable, significant simplifying assumptions must be made. For example, the analytical work described in the remainder of this section was either 1D or 2D and assumed inviscid flow. Furthermore, except for some of the electron ionization models, chemical composition is assumed fixed, and typically the assumption of a calorically perfect gas is made. With this in mind, a large body of work to this effect has been produced

by Macheret and associates at Princeton University. In 1997, they proposed using a 30keV electron beam to ionize a Mach 10.6 wind tunnel flow and then use the Lorentz force to accelerate the flow to Mach 14.3 [44]. In 2001 and 2002, they put forward several detailed papers focused on non-equilibrium ionization methods with application toward supersonic MGD power generation. Two years prior to the OSU work described above, they explored both electron beams and steady and pulsed electric fields, concluding high energy electron beams (order of 10–1000s of eV) required 1-2 orders of magnitude lower input power than a comparable ionization produced by an electric field [48]. Applying this conclusion to a simplified 2D analysis of a MGD-controlled scramjet inlet, they predicted the ability to maintain the shock-on-cowl-lip condition for Mach numbers of two greater than the geometrical design Mach number [47]. Although some of this effect was attributable to heating, the work done by the Lorentz force was shown to be a significant contributor as well. This same work also demonstrated more electrical power was generated by the MGD interaction than was required to power the electron beam ionization source. Similar calculations for a 3x0.25x0.25-meter inlet at flight Mach numbers of 4–10, subjected to a 7T magnetic field, generated several MW of excess power by converting approximately 1/3 of the flow enthalpy to electrical power [45, 46]. In the past two years, 1D and 2D analytical work has predicted MW-class power generation using more moderate 1T magnetic fields in potassium-seeded combustor flows; power that would then be made available for applications such as the control of inlet shock location using virtual cowl shapes created by MGD and/or plasma-controlled external combustion [50, 73, 74]. Finally, recent research has extended these concepts to wind tunnel models of simple aerodynamic structures [7] providing evidence to support the basic science and analytical work and reinforcing the need to continue exploration of flight vehicle-sized applications such as the MGD-energy bypass discussed next.

The most ambitious overall MGD system application is without a doubt the MGD-energy bypass method which has been examined in several contexts by multiple researchers [10, 21, 43, 54, 60, 67]. However, the most frequently cited example of

the application of an MGD energy bypass method remains that originally espoused by Russian researchers led by A.L. Kuranov at the Hypersonic Systems Research Institute (HSRI) in St. Petersburg. HSRI researchers developed a conceptual hypersonic aircraft, known as AJAX, which relied on their Magneto-Plasma Chemical Engine (MPCE) for both power and propulsion [8, 9, 35]. The conceptual work on the AJAX vehicle was among the first to show the potential for electromagnetic-fluid interactions to improve the performance of scramjet engines. Specific to the AJAX approach was the use of a parameter-based quasi-1D analysis (as well 2D inlet-specific numerical studies). This analysis utilized the inviscid subset of the Navier-Stokes fluid flow equations (i.e. the Euler equations) coupled to a source term formulation of Maxwell's equations for electromagnetic fields [35]. The latter equations were cast in terms of the applied magnetic flux density, $\vec{B}$, the load factor, k, and a scalar electrical conductivity, σ. In addition, the model assumed a calorically perfect gas existed throughout the flow. A final, critical supposition was that the flow sustained a level of ionization sufficient to ensure appreciable MGD interaction. Assuming all of the enthalpy extracted from the flow was made available to the MGD accelerator, the MPCE was shown in some cases to produce 5-10 percent higher specific impulse (I_{SP}) than a conventional scramjet of the same geometry when approximately 10 percent of the freestream enthalpy was extracted from the flow. Further studies defined the self-powered MGD bypass system envelope for a Mach 6 engine in terms of the magnetic field, ionization power and relative effectiveness of the electromagnetic interaction [34]. In this model, self-powered operation was attained for magnetic fields stronger than about 0.8T when the ionization power was on the order of 2W/cm^3. As pointed out by the authors' conclusions though, the "extent of magnetohydrodynamic (MHD) influence on scramjet performance essentially depends on the type of MHD generator, inlet characteristics, load factors, Hall parameter, ionizer parameters, and flow parameters [33]."

Regarding the components of a typical MGD bypass system, Figure 1.3 presents a simplified schematic of the MPCE with its key features. One or more MGD gen-
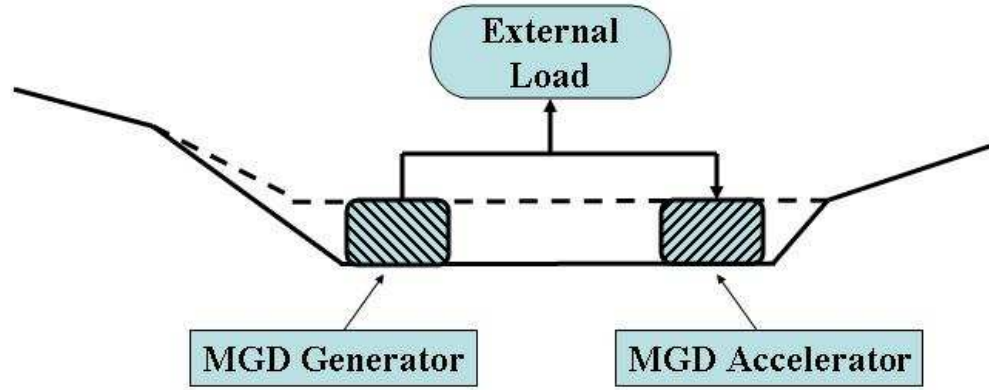
Figure 1.3:   Magneto-Plasma Chemical Engine (MPCE) Schematic

erators perform two key functions. First, a portion of the freestream enthalpy is extracted and converted to electrical power, and second, more efficient flow compression is obtained than through the use of shock-trains alone [33, 78]. A portion of the extracted electricity is used to power a flow ionization system, which for AJAX was always assumed to be accomplished by a high energy electron beam source [36] described in greater detail in Section 2.7. The remaining electrical energy is available for onboard electrical power requirements to include the use of an MGD accelerator, if desired. The MGD accelerator is installed downstream of the combustion chamber to convert electrical energy back into flow enthalpy, thereby increasing the thrust. In the work referenced here, all power left over after flow ionization, which varied anywhere from 0.0 to $100W/cm^3$ was returned as flow enthalpy in an MGD accelerator [36]. Bypassing a portion of the inlet flow energy around the combustor in this manner, may also also allow the combustor to operate more efficiently. This is possible because the flow enters the combustor of an MGD bypass equipped scramjet at both higher pressure and lower Mach number.

1.3   Thesis

As with all prior work in this field, the AJAX vehicle design and related concepts have used incomplete analytical treatments and reduced dimensional numerical stud-

ies. As a consequence, not all of the pertinent flow physics have been captured and thus the conclusions previously reached are uncertain at best. *The purpose of this research, then, is to apply the first comprehensive three-dimensional computational analysis to a flight-sized, Mach 10 cruise scramjet engine to determine if, and under what circumstances, electromagnetic flow control can improve performance.* Both localized MGD flow control applications and the MGD energy bypass system are explored. Comparisons are made to a baseline geometry without flow control. In addition, numerous metrics exist for determining performance, and a portion of this research explores which ones provide the most insight into the impacts of the flow control applications. Unlike prior computational efforts in this field, this research has removed many of the simplifying assumptions utilized in previous approaches (e.g. unrealistic flowpath geometries, calorically perfect gases, and inviscid, 2D flow solvers). In a significant new development, a finite rate chemistry model is applied to this computational method for the first time, providing the only accurate model of fuel injection, mixing and combustion in an MGD flow controlled engine. By doing this and removing the other assumptions mentioned, these electromagnetic (EM) flow control concepts are more fully examined and the viability of a flight-scale system determined.

1.4 Document Scope and Organization

This document is organized into seven chapters, including this introduction. The foundation of the research effort is provided in Chapter II, including a presentation of the governing equations used in the computational model. The other major features of this chapter are the description of available efficiency metrics with their advantages and disadvantages and the adoption of an existing ionization model to the computational method. Chapter III provides a detailed description of the preliminary research that resulted in defining the engine flowpath geometry based on the requirements for an operationally sized Mach 10 cruise vehicle. The addition of finite rate thermochemistry to the computational model, a key prerequisite underpinning

suitable model fidelity, is discussed in Chapter IV. Electromagnetic flow control is addressed in two separate chapters. First, localized control is investigated in Chapter V with respect to mitigating flow separation within the inlet. Then, the MGD energy bypass method of improving engine efficiency and providing auxiliary electrical power is explored in VI. Finally, Chapter VII summarizes the results of this research and answers the fundamental question presented by the thesis: can electromagnetic flow control improve the performance of a flight-representative scramjet engine?

II. Research Foundations and Governing Equations

2.1 Description of the Computational Method

Inspired in part by AJAX and related efforts, Air Force Research Laboratory (AFRL) researchers extended the capability to analyze MGD flow control applications by developing a computational fluid dynamics (CFD) code to model the full, three-dimensional set of coupled Navier-Stokes and Maxwell's equations for a non-ideal gas [20]. (As an aside, 'non-ideal' in this context refers to the non-uniform conductivity found in the weakly ionized, less than perfectly conducting fluid typical of the altitudes and low hypersonic Mach numbers encountered by scramjets.) However, the code did not address chemical kinetics but instead relied on a calorically perfect gas model.

Initial work achieved success by using a compact spatial discretization based on Padé type formulas and a traditional fourth order Runge-Kutta for temporal integration [20]. The compact differencing approach was chosen as it would work for nearly all values of the magnetic Reynold's number, Re_m, which may be considered the ratio of the induced magnetic field to the total magnetic field. Also, it would provide up to sixth order accuracy, a necessity for discerning fine wave structures. However, two drawbacks to this approach were the overall code complexity and the diffusiveness of the central difference approach, especially when treating certain phenomena like shock waves. This code was first verified against accepted analytical results for unit problems such as simple Alfvén wave propagation [20]. With the code verified, further studies continued by examining external flows around hypersonic blunt bodies, specifically an axisymmetric, spherical-nosed body with an imposed magnetic dipole field [61]. Again, the numerical results compared well with the analytical solution. First, it was shown for the levels of thermal ionization typical of reentry ($\sim$100mho/m) that magnetic flux densities greater than 1T could slow the flow in the shock layer, increase drag, and increase the shock standoff distance. Then the same fields were demonstrated to lower the wall heat flux in the stagnation point region, an effect

that increased with increasing magnetic field and decreased whenever the electrical conductivity was non-ideal [62, 63].

Having developed an approach to handle the full equation set, including the generalized diffusivity terms, efforts commenced to increase the fidelity and efficiency of the code [22], especially with respect to the flow regime dictated by the MGD approximations (which are presented in their entirety in Subsection 2.3.3). The MGD approximations are ideally suited for the hypersonic flows of practical interest to scramjet design. This is because they are certainly non-relativistic and occur at sufficient dynamic pressure to maintain the gas as a dense, collision-dominated plasma. The latter property ensures that although the plasma is conductive, the high frequency of collisions promote both ionization and recombination, keeping both charge separation and the conductivity relatively small (what is referred to commonly as a *weakly ionized* plasma). Under these conditions, if the MGD interaction is to be appreciable, the applied magnetic field has to be relatively large to make up for the low conductivity. In fact, the applied magnetic field significantly influences the fluid motion. However, the flow distorts the induced magnetic field which is assumed to be relatively small compared to the externally applied field. This set of circumstances is embodied in the low Re_m condition which is expressed mathematically by Equation 2.1 where V_0, L_0, σ_0, and μ_e are the reference values for velocity, length, conductivity, and magnetic permeability, respectively. As an example, a one meter nose radius blunt body, flying at 8 km/s at an altitude of 61 km would produce only $\sigma = 300$ mho/m in the equilibrium flow downstream of the bow shock, resulting in $Re_m \sim 3$ [62]. This example corresponds to a re-entry vehicle at a Mach number (M) greater than 20. At the lower altitudes and Mach numbers envisioned for scramjets, $Re_m << 1$ is a valid assumption.

$$Re_m = V_0 L_0 \sigma_0 \mu_e \tag{2.1}$$

The conclusion to be drawn from the combination of low σ and high $\vec{B}$ that defines the low Re_m regime is that electromagnetic effects may be added directly to the

Navier-Stokes equations as simple source terms. This approach proved conducive to allowing traditional upwind spatial discretization schemes such as the Roe flux difference scheme that, while lower in order of spatial accuracy, were much less diffusive in capturing flow discontinuities such as shocks. A Poisson solver was then incorporated to provide the option of either calculating the electric field, $\vec{E}$, or simply specifying its vector components at every point [23]. When taking the former, higher fidelity, approach, the scalar electric potential, ϕ, on the boundaries is specified and subsequently $\vec{E} = -\nabla\phi$ is solved by enforcing current continuity as given by Equation 2.2 where the conduction current, $\vec{j}$, is given by Ohm's Law in the form of Equation 2.3. (In Equation 2.3, $\vec{V}$ is the velocity and the other variables are as previously defined.) As an aside, the generalized Ohm's law, which is presented in Subsection 2.3.1, can be applied to account for the Hall effect and ion-slip typically encountered in flows with extremely high applied magnetic fields [22]. However, in this research, Hall Effect was not factored into the results.

$$\nabla \cdot \vec{j} = 0 \tag{2.2}$$

$$\vec{j} = \sigma \left[\vec{E} + \vec{V} \times \vec{B} \right] \tag{2.3}$$

Finally, two more tools were added to the method, the first to improve stability and the second to address turbulent flows. Regarding the former, an approximately-factored Beam-Warming implicit method was developed to overcome the time-step stability limitation of the previously used 4th order Runge-Kutta (RK4) scheme that was encountered, especially when using highly stretched meshes [22]. The implicit method, while limited to second-order accuracy, demonstrated several important advantages. These advantages were demonstrated on two sample problems of electromagnetic field diffusion and wave propagation which were also solved analytically and with the explicit RK4 scheme. Both computational methods compared well with the analytical solution, however the implicit method had a stable time step size three orders of magnitude greater than the RK4 scheme, and each implicit time step required

only 5% more computational time than its explicit counterpart. As far as turbulent flows were concerned, the magnetic field's impact on turbulence presented a significant challenge. This is due primarily to the anisotropy brought about the preferential damping of turbulent fluctuations normal to the magnetic field [71]. Therefore, an engineering-based approach using a two equation $k - \epsilon$ turbulence model based on liquid metal flows was incorporated to "mimic some of the anticipated effects of the magnetic field in a simple yet effective manner [22]." The $k - \epsilon$ equations are also integrated implicitly in time but are loosely coupled to the flow equations. This loose coupling considerably reduces the expense of computing the flux Jacobians. Several calculations of turbulent flow over a flat plate were made to characterize the effect of a transverse magnetic field on the flow. Among other things, decreases in the local skin friction coefficient in the vicinity of the magnetic dipole were observed. In addition, it was "evident that in the context of the present model the dominant effect of the magnetic field is on the interaction with the mean flow" [22] as demonstrated by a thickening of the boundary layer and corresponding reduction in surface gradient. Having all of these tools, the code was sufficiently developed to attempt modelling problems of practical engineering interest.

With the code matured and verified, the first ever attempt was made to numerically model an entire 3D scramjet flowpath to "explore the fluid dynamics of scramjet internal flows, and their interaction with a specified plasma and combustion environment [21]." The electromagnetic source term form of the governing equations was used with combustion accounted for by a volumetric heating rate source term in the energy equation. Both laminar and turbulent cases were explored. Using freestream reference conditions for the Reynold's number (Re), Mach number (M), and temperature (T), respectively, of $Re = 1.6 \times 10^6$, $M_0 = 8.0$ and $T_0 = 250$K, the flowpath, as shown in Fig 2.1, began with a dual-plane compression system with an MGD generator in the horizontal compression surface. This was followed by a combined, constant-area isolator and combustor, and finally a two ramp internal/external expansion surface. This model geometry was intentionally simplified to prevent adverse

effects like thermal choking, and no attempt at performance optimization was made. Modelling simplifications were made to allow for the fact that detailed ionization and thermochemistry models were not part of the code. In effect, flow conductivity and combustion heat addition were modelled using Gaussian distributions that were placed in the inlet/exit and combustor, respectively [21].
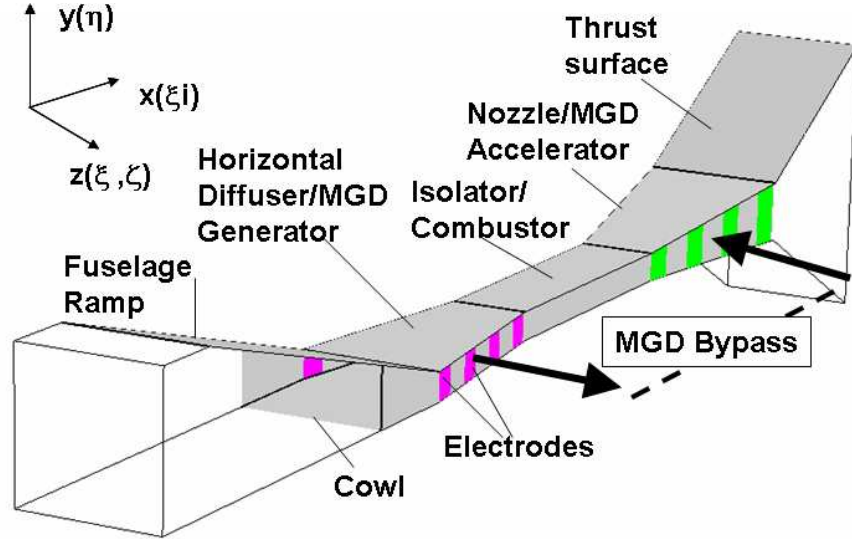
Figure 2.1:   AFRL/VA Scramjet Model [21]

Even with these simplifications and assumptions, sometimes unexpected results were obtained [21]. For example, the 3D viscous interaction effects altered the structure of the current and Lorentz fields in the MGD component regions. Vortical structures due to the sidewall compression (readily evident in Figure 2.2(a)) also gave rise to several non-uniform current features in the flow. Several of these features can be seen in Figure 2.2(b) such as the eddy currents and current 'pinch' in the inlet. In the boundary layer, the applied $\vec{E}$-field exceeded that induced by the flow motion ($\vec{V} \times \vec{B}$) causing the local reversal of the current and Lorentz Force (e.g. flow acceleration vice deceleration in the MGD generator). Finally, spanwise (i.e. yawing) force components were observed, although the geometry was symmetric about the vertical plane. In spite of all these effects, overall MGD generation efficiently reduced inlet flow speed, indicating enthalpy was extracted, but also a net drag penalty was
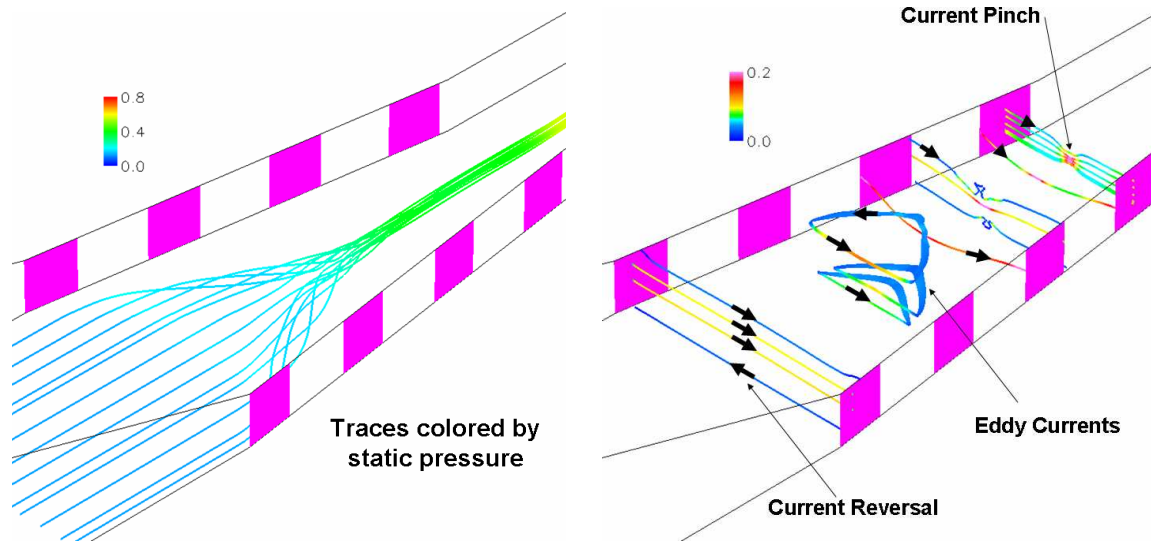
(a) Streamtrace of Vortical Structures due to Sidewall Interaction

(b) 3D-Flow Induced Effects on Current Path

Figure 2.2:   Examples of 3D MGD-Flow Interaction in AFRL Scramjet Inlet Model[21]

accrued. Conversely, the MGD accelerator operation, as configured, experienced significant heating in the boundary layer due to Joulean dissipation [21]. This loss, given by $\left|\overline{\overline{j}}\right|^2/\sigma$, is an inevitable consequence of the plasma having a finite conductivity, and can be a significant concern for the weakly ionized plasmas under consideration.

It was this preliminary investigation that revealed just how little was understood about how this technology would apply to and impact an operational scramjet engine. Therefore, the research documented herein was undertaken to expand upon the limited knowledge of this subject. Before presenting this research, a few more items must be presented. First, a brief presentation of the MGD equations and assumptions is made along with how the computational code implements them. This is followed by the control volume formulation of the equations as well as the electron beam ionization model used. These two subjects are needed in order to determine the performance of the flow control systems tested.

2.2 The Governing Equations of Magnetogasdynamics

The MGD equations are derived from the fully coupled Navier-Stokes and Maxwell's equations, the former equation set governing fluid flow from the continuum perspective and the latter governing the propagation of electromagnetic fields. There are a multitude of sources for the derivation of these equations. The presentation that follows draws primarily from References [14, 17, 30, 75].

2.2.1 Navier-Stokes Equations. These equations are based on the laws of the conservation of mass, momentum, and energy as applied to a continuous medium. Neglecting radiative heat transfer and, for the moment, body forces, these three laws can be expressed in the following differential form for Cartesian coordinates, respectively:

$$\frac{\partial \rho}{\partial t} + \frac{\partial (\rho V_i)}{\partial x_i} = 0 \tag{2.4}$$

$$\frac{\partial (\rho V_i)}{\partial t} + \frac{\partial (\rho V_i V_j)}{\partial x_j} + \frac{\partial (p\delta_{ij})}{\partial x_j} - \frac{\partial \tau_{ij}}{\partial x_j} = 0 \tag{2.5}$$

$$\frac{\partial (\rho e_t)}{\partial t} + \frac{\partial (\rho h_t V_j)}{\partial x_j} - \frac{\partial (q_j + \tau_{ji} V_i)}{\partial x_j} = 0 \tag{2.6}$$

In the above equations, ρ is the density, and P is the pressure. The velocity vector, $\vec{V}$, is composed of u, v, w components in the x, y, z directions, respectively. V_i, V_j, or V_k also represents one of these components. The stress tensor, τ_{ij}, and the heat flux vector, q_j, are defined below:

$$\tau_{ij} = \mu_f \left(\frac{\partial V_i}{\partial x_j} + \frac{\partial V_j}{\partial x_i} \right) - \frac{2}{3} \delta_{ij} \mu_f \frac{\partial V_k}{\partial x_k} \tag{2.7}$$

$$q_j = \kappa_f \frac{\partial T}{\partial x_j} \tag{2.8}$$

The computational code uses Sutherland's Law to determine the molecular viscosity, μ_f, and thermal conductivity, κ_f, transport properties based on local temperature. It should be noted that these are empirically based expressions typically tabulated for a single species (e.g. molecular oxygen) or fixed composition mixture (e.g. low-temperature air).

$$\mu_f \approx \mu_{0,f} \left(\frac{T}{T_0} \right)^{\frac{3}{2}} \frac{T_0 + S_{\mu_f}}{T + S_{\mu_f}} \tag{2.9}$$

$$\kappa_f \approx \kappa_{0,f} \left(\frac{T}{T_0} \right)^{\frac{3}{2}} \frac{T_0 + S_{\mu_f}}{T + S_{\kappa_f}} \tag{2.10}$$

In the above equations, typical reference values for air are given by $\mu_{0,f} = 1.716 \times 10^{-5} \text{kg/(m–s)}$, $T_0 = 273\text{K}$, $S_{\mu_f} = 111\text{K}$, $\kappa_{0,f} = 2.41 \times 10^{-2} \text{J/(s–m–K)}$, and $S_{\kappa_f} = 194\text{K}$ [84]. The total enthalpy, $(h_t$, and total energy, e_t, which appear in the energy equation are defined as follows:

$$h_t = h + \frac{1}{2} V_i V_i \tag{2.11}$$

$$e_t = h_t - \frac{p}{\rho} \tag{2.12}$$

In addition, for flows where chemical reactions occur among n species, $n - 1$ species mass conservation equations are also needed to supplement the global mass conservation equation above. The species conservation equation for each species, s, is given by:

$$\frac{\partial \rho_s}{\partial t} + \frac{\partial (\rho_s V_i)}{\partial x_i} - \frac{\partial}{\partial x_i} \left(D_s \frac{\partial \rho_s}{\partial x_i} \right) - \dot{W}_s = 0 \tag{2.13}$$

where the first two terms are the same as in the global equation, the third term represents the species diffusion (as governed by the diffusion coefficient, D_s), and the

final term, $\dot{W}_s$, represents the rate of species production or depletion due to chemical reaction. As currently implemented, this code assumes the effect of species diffusion may be neglected relative to the species convection and production terms.

2.2.2 Ideal Gas Equation of State. Excluding the species mass conservation equations, the Navier-Stokes' and associated equations presented above have six unknowns, (ρ, u, v, w, p, e_t). One additional independent equation is needed to close the system. With the assumption that the medium behaves as an ideal gas, the ideal gas equation of state is used, wherein R is the specific gas constant for the medium:

$$p = \rho R T \tag{2.14}$$

2.2.3 Vector Form of the Navier-Stokes Equations. To use the NSE given above in a computational method, it is common to express them in the conservative vector form as follows:

$$\frac{\partial \mathbf{U}}{\partial t} + \frac{\partial \mathbf{E}}{\partial x} + \frac{\partial \mathbf{F}}{\partial y} + \frac{\partial \mathbf{G}}{\partial z} = \mathbf{S} \tag{2.15}$$

where $\mathbf{U}$ is the vector of conservative variables:

$$\mathbf{U} = \begin{bmatrix} \rho & \rho u & \rho v & \rho w & \rho e_t \end{bmatrix}^T \tag{2.16}$$

$\mathbf{E}$, $\mathbf{F}$, $\mathbf{G}$ are the total fluxes in the x, y, and z-directions, respectively, which decompose into inviscid and viscous flux vectors:

$$\mathbf{E} = \mathbf{E_i} - \mathbf{E_v} = \begin{bmatrix} \rho u \\ \rho u^2 + p \\ \rho u v \\ \rho u w \\ \rho h_t u \end{bmatrix} - \begin{bmatrix} 0 \\ \tau_{xx} \\ \tau_{xy} \\ \tau_{xz} \\ u\tau_{xx} + v\tau_{xy} + w\tau_{xz} + q_x \end{bmatrix} \tag{2.17}$$

2-9

$$\mathbf{F} = \mathbf{F_i} - \mathbf{F_v} = \begin{bmatrix} \rho v \\ \rho uv \\ \rho v^2 + p \\ \rho vw \\ \rho h_t v \end{bmatrix} - \begin{bmatrix} 0 \\ \tau_{xy} \\ \tau_{yy} \\ \tau_{yz} \\ u\tau_{xy} + v\tau_{yy} + w\tau_{yz} + q_y \end{bmatrix} \qquad (2.18)$$

$$\mathbf{G} = \mathbf{G_i} - \mathbf{G_v} = \begin{bmatrix} \rho w \\ \rho uw \\ \rho vw \\ \rho w^2 + p \\ \rho h_t w \end{bmatrix} - \begin{bmatrix} 0 \\ \tau_{xz} \\ \tau_{yz} \\ \tau_{zz} \\ u\tau_{xz} + v\tau_{yz} + w\tau_{zz} + q_z \end{bmatrix} \qquad (2.19)$$

and $\mathbf{S}$ is the source term:

$$\mathbf{S} = \begin{bmatrix} 0 & 0 & 0 & 0 & 0 \end{bmatrix}^T \qquad (2.20)$$

2.3 Maxwell Equations

The governing equations of electromagnetics are known as Maxwell's equations (ME). According to the Theory of Relativity, these equations are the same within any non-accelerated reference frame, however, two frames are commonly considered. The 'laboratory' frame is such that the media moves relative to the stationary observer, and the 'rest' frame is defined by the observer moving with the media (i.e. the observer is "at rest" with respect to the moving media). This latter reference frame will be denoted by a prime. Because of the invariance described above, these equations are defined as follows and are changed to the rest frame simply by the addition of a prime to all terms [30]:

$$\nabla \cdot \vec{D} = \rho_e \qquad (2.21)$$

$$\nabla \cdot \vec{B} = 0 \qquad (2.22)$$

$$\nabla \times \vec{E} = -\frac{\partial \vec{B}}{\partial t} \tag{2.23}$$

$$\nabla \times \vec{H} = \vec{j} + \frac{\partial \vec{D}}{\partial t} \tag{2.24}$$

where $\vec{D}$ is the electric flux density, ρ_e is the space charge density, $\vec{B}$ is the magnetic flux density, $\vec{E}$ is the electric field, $\vec{H}$ is the magnetic field, and $\vec{j}$ is the conduction current.

2.3.1 Ohm's Law. Just as the NSE require auxiliary relationships to close the system, so do Maxwell's Equations. The first of these is the constitutive relation given by Ohm's law which relates the conduction current to the electric field. It is defined for linear isotropic media in the rest frame as follows:

$$j'_i = \sigma_{ji} E'_j \tag{2.25}$$

where σ is the conductivity.

The Maxwell-Lorentz transformations (MLT) are used to transform the Maxwell equations from the rest frame to the laboratory frame, which is more commonly used in MGD applications. When the media is nonuniform in all directions, i.e. anisotropic, and $V^2 << c^2$ (where c is the speed of light), Ohm's law for a nonlinear media is as follows [30]:

$$j_i = \sigma_{ji}[E_j + (\vec{V} \times \vec{B})_j] + \rho_e V_i \tag{2.26}$$

2.3.2 Additional Constitutive Relations. The constitutive relations are also required to close the system. For linear, isotropic dielectrics and magnetic materials, these relations are expressed in the rest frame as follows [30]:

$$\vec{E}' = \frac{\vec{D}'}{\epsilon_e} \tag{2.27}$$

$$\vec{B}' = \mu_e \vec{H}' \tag{2.28}$$

where μ_e is the permeability, and ϵ_e is the permittivity. The MLT are also used to transform these constitutive relations to the laboratory frame. When $|\vec{V}|^2 << c^2$, and the medium is isotropic, the constitutive relations are as follows [30]:

$$\vec{D} = \epsilon_e[\vec{E} + (1 - \frac{1}{\frac{\epsilon_e}{\epsilon_{e,0}} \frac{\mu_e}{\mu_{e,0}}})\vec{V} \times \vec{B}] \tag{2.29}$$

$$\vec{B} = \mu_e[\vec{H} - (1 - \frac{1}{\frac{\epsilon_e}{\epsilon_{e,0}} \frac{\mu_e}{\mu_{e,0}}})\vec{V} \times \vec{D}] \tag{2.30}$$

Note, that in media in which μ_e and ϵ_e both have their free space values, $\mu_{e,0}$ and $\epsilon_{e,0}$, the constitutive relations also become frame invariant. Since this is nearly always the case with the plasmas used in MGD applications, these relations can be used to explicitly remove $\vec{D}$ and $\vec{H}$ from Maxwell's equations to obtain:

$$\nabla \cdot \vec{E} = \frac{\rho_e}{\epsilon_{e,0}} \tag{2.31}$$

$$\nabla \cdot \vec{B} = 0 \tag{2.32}$$

$$\nabla \times \vec{E} = -\frac{\partial \vec{B}}{\partial t} \tag{2.33}$$

$$\nabla \times \vec{B} = \mu_{e,0}\vec{j} + \mu_{e,0}\epsilon_{e,0}\frac{\partial \vec{E}}{\partial t} \tag{2.34}$$

2.3.3 Magnetogasdynamic Assumptions. When an electrically conducting fluid (or continuum gas) is moving in the presence of a magnetic field, the flow of the fluid is influenced by the field and the field is influenced by the moving fluid. If certain assumptions are made, these interactions can simplify the coupling of the Navier-Stokes' and Maxwell's equations into a form referred to as the magnetogasdynamic equations. These MGD assumptions are as follows [17, 30]:

MGD Assumption 1: $|\vec{V}|^2 << c^2$, the magnitude of the velocities dealt with in fluid dynamics are much less than the speed of light allowing the $\sqrt{1 - (|\vec{V}|/c)^2}$ term to be set to unity.

MGD Assumption 2: $\vec{E} \approx \mathcal{O}(\vec{V} \times \vec{B})$, the electric field is of the order of any induced effects which implies that the applied magnetic field is much greater than the induced magnetic field. Recall, this assumption defines the low Re_m regime and allows the electromagnetic body force and energy interaction to be coupled to the NSE as source terms.

MGD Assumption 3: High frequency phenomena are not considered such that the conduction current is dominant, i.e. $\frac{\partial \vec{D}}{\partial t} \approx 0$. $\frac{\partial \vec{E}}{\partial t}$ is also zero by the constitutive relations. This assumption then implies that $\nabla \times \vec{B} = \mu_{e,0} \vec{j}$. Finally, the assumption implies the media is a conductor and not a dielectric. In an ionized gas, this assumption holds up to microwave frequencies [30].

MGD Assumption 4: $\epsilon_{e,0} \vec{E}^2 << \frac{\vec{B}^2}{\mu_{e,0}}$, the electric energy is insignificant compared to the magnetic energy. When combined with Assumption 3, this assumption ensures the main interaction is between the magnetic field and the fluid.

MGD Assumption 5: The space charge may be neglected in Ohm's Law, such that in the laboratory frame it is given by $\vec{j} = \sigma(\vec{E} + \vec{V} \times \vec{B})$. The conductivity is also considered independent of magnetic field and constant with frequency. This assumption implies that $\vec{j}' = \vec{j}$.

MGD Assumption 6: The electromagnetic body force can be simplified to: $\vec{f}^L = \rho_e \vec{E} + \vec{j} \times \vec{B}$. Furthermore, assuming the overall gas is electrically neutral (i.e. a plasma), the space charge term may be neglected such that $\vec{f} = \vec{j} \times \vec{B}$

Although not an independent approximation, assumptions 1 and 3 may be combined to get the current conservation equation $\nabla \cdot \vec{j} + \frac{\partial \rho_e}{\partial t} = 0$. Assuming a dense, collision-dominated plasma, or a conducting gas, the space charge derivative, $\frac{\partial \rho_e}{\partial t}$, may again be neglected and the current conservation equation in the form of Eqn 2.2 may be used in place of Eqn 2.31.

2.3.4 Maxwell Equations for Magnetogasdynamic Flow. When the MGD approximations above are applied to the ME, a new set of equations which govern electromagnetic fields are formed. These equations in the laboratory frame are [30]:

$$\nabla \times \vec{E} = -\frac{\partial \vec{B}}{\partial t} \tag{2.35}$$

$$\nabla \times \vec{B} = \mu_{e,0}\vec{j} \tag{2.36}$$

$$\nabla \cdot \vec{j} = 0 \tag{2.37}$$

$$\nabla \cdot \vec{B} = 0 \tag{2.38}$$

and Ohm's law, as given by Assumption 5, becomes:

$$\vec{j} = \sigma(\vec{E} + \vec{V} \times \vec{B}) \tag{2.39}$$

NOTE: All subsequent equations are written in the laboratory frame unless otherwise noted.

2.4 The Magnetogasdynamic Equations: Source Term Formulation

The source term formulation of the Magnetogasdynamic Equations (MGDE) result from the combination of the NSE and the ME subject to the MGD assumptions. In other words, these equations describe the interaction between electromagnetic fields and electrically conducting gases in a continuum governed by the MGD assumptions, and in particular Assumption 2 regarding a low Re_m. The MGDE are defined as follows:

$$\frac{\partial \rho}{\partial t} + \frac{\partial(\rho V_i)}{\partial x_i} = 0 \tag{2.40}$$

$$\frac{\partial(\rho V_i)}{\partial t} + \frac{\partial(\rho V_i V_j)}{\partial x_j} - \frac{\partial(p\delta_{ij})}{\partial x_j} - \frac{\partial \tau_{ij}}{\partial x_j} = f_i{}^L \tag{2.41}$$

$$\frac{\partial(\rho e_t)}{\partial t} + \frac{\partial(\rho h_t V_j)}{\partial x_j} - \frac{\partial(q_j + \tau_{ji}V_i)}{\partial x_j} = \dot{W}_{EM} \tag{2.42}$$

In Eqn 2.41, $\vec{f}^L = (\vec{j} \times \vec{B})$ is known as the Lorentz force and is the body force brought about by the electromagnetic fields acting on the moving, charged particles (i.e. the conduction current) in the plasma. This phenomena also gives rise to the electromagnetic energy interaction given in Eqn 2.42 as $\dot{W}_{EM} = \vec{E} \cdot \vec{j}$. This energy interaction can be broken down into the sum of its two constituent parts by using the MLT for the electric field and Ohm's Law. When this is done, the first term is the Joulean dissipation, given by $|\vec{j}|^2/\sigma$, which is always energy put into the gas. The second term is the rate at which $\vec{f}^L$ does work on the fluid as given by $\vec{V} \cdot (\vec{j} \times \vec{B})$. Roughly speaking, this term is positive when $\vec{f}^L$ acts to accelerate the flow and negative when it is decelerating the flow.

2.4.1 Non-dimensionalization of the Magnetogasdynamic Equations. By non-dimensionalizing the equations, problems of different scale can be compared independent of the reference conditions. The dimensionless quantities used in the normalization of the MGDE are as follows where an asterisk represents a dimensionless quantity [30]:

$$
\begin{aligned}
L^* &= \frac{L}{L_0} & \vec{V}^* &= \frac{\vec{V}}{V_0} \\
\rho^* &= \frac{\rho}{\rho_0} & T^* &= \frac{T}{T_0} \\
\vec{E}^* &= \frac{\vec{E}}{E_0} & \vec{B}^* &= \frac{\vec{B}}{B_0}
\end{aligned}
\tag{2.43}
$$

These initial dimensional quantities of L_0, V_0, ρ_0, T_0, E_0, and B_0 are used to non-dimensionalize the other variables, and all dimensionless variables are substituted into the MGDE. Several dimensionless parameters are formed during the non-dimensionalization which help to characterize the MGD problem. The Reynolds number, Re, is the ratio of inertial forces to viscous forces, defined as follows:

$$Re = \frac{\rho_0 V_0 L_0}{\mu} \tag{2.44}$$

The magnetic Reynolds number, Re_m, introduced in Section 2.1, is a measure of the magnitude of the induced magnetic field compared to the total magnetic field. Recall, it is given by Equation 2.1 as $Re_m = V_0 L_0 \sigma_0 \mu_e$.

The reference Mach number, M_0, is the ratio of the reference flow speed to the speed of sound and is therefore defined as follows:

$$M_0 = \frac{V_0}{a_0} \tag{2.45}$$

The Prandtl number (Pr) is the ratio of kinematic viscosity to thermal diffusivity:

$$Pr = \frac{c_P \nu_f \rho_0}{\kappa_f} \tag{2.46}$$

The interaction parameter, Q, is used when the applied magnetic field is much larger than the induced field, i.e. $Re_m \ll 1$, and is defined as the ratio of the ponderomotive force to the inertial force. In MGD applications it is typically $\mathcal{O}(1)$, and increasing values typically correspond to increasing values of the applied magnetic field.

$$Q = \frac{\sigma_0 B_0^2 L_0}{\rho_0 V_0} \tag{2.47}$$

The load factor, k, is defined by Equation 2.48 as the ratio of the applied electric field to the field induced by the conducting fluid moving through the magnetic field. An increase in k signifies a larger electric load placed on the system. The negative sign in the following equation assumes that E_0 is applied in a direction opposite to $V_0 B_0$, such that k is always positive. With this convention, when $k < 1$ the electrical load is powered by the current generated by the conducting plasma moving through the magnetic field, commonly referred to as MGD power generation. $k > 1$ means the applied electric field produces a current that exceeds that induced by the plasma

motion and thus net electrical power is put back into the flow, a concept referred to as MGD acceleration. Two special cases for k should also be kept in mind. $k = 0$ implies that there is no electrical load, or in other words, there is a short-circuit condition. When this occurs, the current generated by MGD interaction sets up entirely within the flow and thus all the electrical energy generated must be dissipated within the flow as heating. On the other hand, $k = 1$ conforms to the open-circuit case, where the applied load exactly matches the current produced in the flow, and the overall MGD interaction is minimized. Finally, it should be noted the definition of k given here is based on the reference velocity and EM field values. However, in a real flow field, the actual value of k is a typically a variable, as at the very least the velocity is always changing.

$$k = \frac{-E_0}{B_0 V_0} \tag{2.48}$$

The non-dimensional MGDE are identical to their dimensional counterparts except for the use of non-dimensional quantities and the differences in the stress tensor, heat flux, and MGD source terms.

$$\tau_{ij}^* = \frac{\mu_f^*}{Re} \left[\left(\frac{\partial V_i^*}{\partial x_j^*} + \frac{\partial V_j^*}{\partial x_i^*} \right) - \frac{2}{3} \delta_{ij} \frac{\partial V_k^*}{\partial x_k^*} \right] \tag{2.49}$$

$$q_j^* = \frac{\mu_f^*}{(\gamma - 1) M_0^2 Re Pr} \frac{\partial T^*}{\partial x_j^*} \tag{2.50}$$

The MGD source terms are now multiplied by the interaction parameter. The resulting non-dimensional Lorentz force is $Q(\vec{j}^* \times \vec{B}^*)$, and the energy interaction is $Q(\vec{E}^* \cdot \vec{j}^*)$. The non-dimensional ideal gas law is defined by:

$$T^* = \frac{\gamma M_0^2 p^*}{\rho^*} \tag{2.51}$$

with

$$p^* = (\gamma - 1)\rho^* e^* \tag{2.52}$$

For the remainder of this document the * is dropped and all quantities are dimensionless unless otherwise noted.

2.4.2 Vector Form of the Magnetogasdynamic Equations.   The equations resulting from the non-dimensionalization can then be written in a conservative vector form with the electromagnetic effects in the source term as follows:

$$\frac{\partial \mathbf{U}}{\partial t} + \frac{\partial \mathbf{E}}{\partial x} + \frac{\partial \mathbf{F}}{\partial y} + \frac{\partial \mathbf{G}}{\partial z} = \mathbf{S} \tag{2.53}$$

The only change from the non-dimensional conservative vector form of the NSE is in the source term $\mathbf{S}$, where:

$$\mathbf{S} = \begin{bmatrix} 0 \\ Q(j_y B_z - j_z B_y) \\ Q(j_z B_x - j_x B_z) \\ Q(j_x B_y - j_y B_x) \\ Q(E_x j_x + E_y j_y + E_z j_z) \end{bmatrix} \tag{2.54}$$

2.4.3 Curvilinear Transformation.   In order to accurately model most physical problems, the grid created for the physical domain has non-uniform spacing in at least one direction. This mesh might also be body-fitted involving a non-orthogonal coordinate system. To account for this, the vector form of the MGDE presented above is transformed to a generalized coordinate system (ξ,η,ζ).

$$\begin{aligned}
\xi &= \xi(x, y, z) \\
\eta &= \eta(x, y, z) \\
\zeta &= \zeta(x, y, z) \\
\tau &= t
\end{aligned} \tag{2.55}$$

The differential expressions for this coordinate transform are as follows:

$$\begin{aligned}
d\xi &= \xi_x dx + \xi_y dy + \xi_z dz \\
d\eta &= \eta_x dx + \eta_y dy + \eta_z dz \\
d\zeta &= \zeta_x dx + \zeta_y dy + \zeta_z dz \\
d\tau &= dt
\end{aligned} \tag{2.56}$$

Similarly, the differential expressions for the inverse transformation are as follows:

$$\begin{aligned}
dx &= x_\xi d\xi + x_\eta d\eta + x_\zeta d\zeta + x_\tau d\tau \\
dy &= y_\xi d\xi + y_\eta d\eta + y_\zeta d\zeta + y_\tau d\tau \\
dz &= z_\xi d\xi + z_\eta d\eta + z_\zeta d\zeta + z_\tau d\tau \\
dt &= d\tau
\end{aligned} \tag{2.57}$$

The transformation metrics are defined using Equation 2.56 and Equation 2.57 [76]:

$$\begin{aligned}
\xi_x &= J(y_\eta z_\zeta - y_\zeta z_\eta) \\
\xi_y &= -J(x_\eta z_\zeta - x_\zeta z_\eta) \\
\xi_x &= J(y_\eta y_\zeta - y_\zeta y_\eta)
\end{aligned} \qquad (2.58)$$

$$\begin{aligned}
\eta_x &= -J(y_\xi z_\zeta - y_\zeta z_\xi) \\
\eta_y &= J(x_\xi z_\zeta - x_\zeta z_\xi) \\
\eta_x &= -J(y_\xi y_\zeta - y_\zeta y_\xi)
\end{aligned} \qquad (2.59)$$

$$\begin{aligned}
\zeta_x &= J(y_\xi z_\eta - y_\eta z_\xi) \\
\zeta_y &= -J(x_\xi z_\eta - x_\eta z_\xi) \\
\zeta_x &= J(y_\xi y_\eta - y_\eta y_\xi)
\end{aligned} \qquad (2.60)$$

where the Jacobian of transformation, J, is defined as follows [76]:

$$J = \frac{1}{x_\xi(y_\eta z_\zeta - y_\zeta z_\eta) - x_\eta(y_\xi z_\zeta - y_\zeta z_\xi) + x_\zeta(y_\xi z_\eta - y_\eta z_\xi)} \qquad (2.61)$$

Applying the transformations to Eqn 2.53 and manipulating the equation into strong conservation form, the new terms $\hat{\mathbf{U}}$, $\hat{\mathbf{E}}$, $\hat{\mathbf{F}}$, $\hat{\mathbf{G}}$, and $\hat{\mathbf{S}}$ are formed.

$$\hat{\mathbf{U}} = \frac{\mathbf{U}}{J}$$

$$\hat{\mathbf{E}} = \frac{1}{J}(\mathbf{E}\xi_x + \mathbf{F}\xi_y + \mathbf{G}\xi_z)$$

$$\hat{\mathbf{F}} = \frac{1}{J}(\mathbf{E}\eta_x + \mathbf{F}\eta_y + \mathbf{G}\eta_z) \qquad (2.62)$$

$$\hat{\mathbf{G}} = \frac{1}{J}(\mathbf{E}\zeta_x + \mathbf{F}\zeta_y + \mathbf{G}\zeta_z)$$

$$\hat{\mathbf{S}} = \frac{\mathbf{S}}{J}$$

with the resulting vector equation [76]:

$$\frac{\partial \hat{\mathbf{U}}}{\partial \tau} + \frac{\partial \hat{\mathbf{E}}}{\partial \xi} + \frac{\partial \hat{\mathbf{F}}}{\partial \eta} + \frac{\partial \hat{\mathbf{G}}}{\partial \zeta} = \hat{\mathbf{S}} \qquad (2.63)$$

2.5 Summary of the Numerical Methods Used to Implement the Computational Model

As discussed in Section 2.1, the computational code was subjected to a substantial development and verification process that resulted in multiple computational techniques to span the magnetogasdynamic regime. This process has been well documented in numerous papers, key among them being References [20, 22, 23, 61–63]. Since in the research conducted here, the influence of the magnetic and electric fields contributions are restricted to the source terms of the governing equations, conventional CFD techniques were incorporated to discretize the inviscid and viscous fluxes. Specifically, this research used the solver based on the Roe flux difference splitting scheme for determining the inviscid fluxes in each generalized coordinate direction. Typically, a 1st order solver was initially used to quickly converge a case, and then MUSCL variable extrapolation was used to refine the solution to a nominal 3rd order spatial accuracy. Solution monotonicity was assured with the use of the van-Leer harmonic limiter. The viscous fluxes in each generalized coordinate direction

were discretized using central differences. The approximately factored implicit Beam-Warming scheme was used for temporal integration. Finally, the predominance of the work was accomplished using the $k - \epsilon$ turbulence model. All results should be considered turbulent unless laminar flow is explicitly specified.

The MGDE resolve the flow within the domain, but boundary conditions must be specified to define the flow conditions along the computational boundary. For these simulations, the inflow boundary incorporated a supersonic inflow boundary condition, in which all variables at inlet were set to a constant value. No-slip boundary conditions were enforced along the tunnel walls, with the wall temperature limited to a peak of 2000K. In addition, a zero normal pressure gradient was applied along the wall. Likewise, for cases with thermochemistry, a zero normal gradient in species mass fraction (i.e. non-catalytic wall) was enforced. Because the nominal flow was supersonic everywhere except in the small, subsonic portion of the boundary layers, the outflow boundary was set to supersonic extrapolation from the domain.

2.6   The Control Volume Approach and Performance Analysis

The control volume (CV) formulation of the governing equations of motion lends itself to the determination of system-level interactions and overall performance. These equations can be derived directly from the differential form of the equations by application of Reynold's transport theorem to a fixed control volume [83]. Furthermore, if the flow properties can be assumed constant across the flow cross-section, then the quasi-1D approach reduces the flow to dependence on a single spatial coordinate. Even though the inlet flow considered here has a complex 3D character, by taking area and volumetric averaging of the grid point flow properties, the quasi-1D approach can provide reasonable, conservative results. Finally, two more assumptions are made to obtain the equations that follow: (1) a single CV average value for the thermochemical properties can be taken (e.g. γ, C_V, C_p, etc) and (2) the flow is steady in the sense that the influence of any $\partial/\partial t$ terms is negligible with respect to the steady terms. With this in mind, the CV equation for mass conservation is given by Equation 2.64.

Similarly, the momentum conservation equations are given by Equations 2.65– 2.67, and energy conservation is given by Equation 2.68.

$$(\rho A u)_e - (\rho A u)_i = \dot{m}_e - \dot{m}_i = \sum \dot{m}_o \tag{2.64}$$

where the subscripts e, i, and o refer to the exit plane, inlet plane, and any mass flow through the other boundaries (e.g. cowl spillage, fuel), respectively.

$$F_x = -\dot{m}_i u_i + \dot{m}_e u_e + \sum \dot{m}_o u_o + p_e A_e - p_i A_i \tag{2.65}$$

$$F_y = -\dot{m}_i v_i + \dot{m}_e v_e + \sum \dot{m}_o v_o \tag{2.66}$$

$$F_z = -\dot{m}_i w_i + \dot{m}_e w_e + \sum \dot{m}_o w_o \tag{2.67}$$

where the force components F_x, F_y, and F_z represent the total forces acting on the CV other than the inlet and exit boundaries, including those due to the Lorentz Force, if present.

$$\frac{dE}{dt} = \dot{Q}_{ht} + \dot{W}_{EM} = \dot{m}_e \left(h_e + \frac{V_e^2}{2} \right) - \dot{m}_i \left(h_i + \frac{V_i^2}{2} \right) + \sum \dot{m}_o \left(h_o + \frac{V_o^2}{2} \right) \tag{2.68}$$

where $\dot{W}_{EM}$ is the electromagnetic interaction term, defined in Section 2.4 as the algebraic sum of the work done on the control volume by the Lorentz force and the Joulean dissipation. The final result is given by Equation 2.69. Note, that by convention, the rate of heat energy crossing the CV boundary in Equation 2.68, $\dot{Q}_{ht}$, is considered positive for heat entering the control volume.

$$\dot{W}_{EM} = \vec{E} \cdot \vec{j} = \frac{\left| \vec{j} \right|^2}{\sigma} + \vec{V} \cdot \left(\vec{j} \times \vec{B} \right) \tag{2.69}$$

Four measures are commonly used to describe performance: the total pressure ratio, π_c, the kinetic energy efficiency, η_{KE}, the dimensionless entropy increase, $\Delta s/C_p$, and the adiabatic compression efficiency, η_c [25]. π_c and $\Delta s/C_p$ both rely on constant (or averaged) thermochemical properties to obtain analytical expressions from the solution of Gibbs' equation. Thus, while these measures by themselves will lose some accuracy for the high stagnation enthalpy flows that characterize the scramjet flowpath, they remain useful in determining trends when varying flow parameters. These two performance measures are given by Equations 2.70 and 2.71.

$$\pi_c = \frac{p_{t,e}}{p_{t,i}} = \frac{p_e}{p_i} \left\{ \frac{1 + \frac{\gamma-1}{2}M_e^2}{1 + \frac{\gamma-1}{2}M_i^2} \right\}^{\frac{\gamma}{\gamma-1}} \tag{2.70}$$

$$\frac{\Delta s}{C_p} = \ln\left(\frac{T_e}{T_i}\right) - \frac{\gamma-1}{\gamma} \ln\left(\frac{P_e}{P_i}\right) \tag{2.71}$$

η_{KE} and η_c are both referenced to the freestream static conditions and thus are generally preferred for this type of flow. η_{KE} (Equation 2.72) is defined as the ratio of the square of the velocity the exit flow would achieve if isentropically expanded to freestream conditions to the square of the freestream velocity. Similarly, η_c (Equation 2.73) is the ratio of the isentropic change in enthalpy to the actual change in enthalpy, when both changes are referenced to the same change in static pressure.

$$\eta_{KE} = \frac{V_e^2}{V_i^2} + \frac{2C_p T_e}{V_i^2}\left[1 - \left(\frac{p_i}{p_e}\right)^{\frac{\gamma-1}{\gamma}}\right] \tag{2.72}$$

$$\eta_c \doteq \frac{h_e - h_x}{h_e - h_i} \tag{2.73}$$

where the subscript x denotes the conditions that would exist upon an isentropic change in enthalpy across the actual static pressure change.

There is an additional performance measure commonly encountered when examining MGD flows. The enthalpy extraction/addition ratio or η_g is simply the ratio of the change in stagnation enthalpy across the MGD region to the value at the be-

ginning of the MGD region [35, 42]. In order to obtain a simpler analytical model, total enthalpy is often assumed conserved aside from the EM-interaction due to the MGD device. However, as applied to this research, η_g includes not only the enthalpy change due to this EM-interaction but also the change due to any other effects (e.g. geometric compression, heat of combustion). Because of this it may be difficult or impossible to separate out the EM contribution, especially when multiple factors are acting synergistically. Therefore, η_g, is best viewed relative to similar flows as done, for example, in the inlet comparisons of Chapter V.

2.7   *Approximating the Non-Equilibrium Ionization with a Simplified Electron Beam Model*

Freestream flight conditions of $\rho_0 = 0.01022\text{kg/m}^3$, $V_0 = 3060\text{m/s}$ and the leading edge width reference length of 3.602m meant that $\sigma B^2 \approx 8.684Q$ or a maximum of 43.4 for $Q = 5$. While large, these values are consistent with other proposed values [21, 47]. Figure 2.3 presents the required magnetic field for a given value of conductivity at the values of Q used. By way of comparison, the natural conductivity of air at the freestream conditions was estimated to be approximately 0.03 mho/m, implying that some form of non-equilibrium ionization is required to substantially reduce the required magnetic field.

The computational code as currently implemented does not specify an ionization method, but rather depends on the interaction parameter, Q, and the spatial distribution of the non-dimensionalized electro-magnetic field quantities to solve the coupled equations. However, with this research, a first-order approximation of the average magnitudes of σ_0 and B_0 is presented, as well as the required ionization power, P_{ion}, and generated electrical power, P_{gen}. To accomplish this, a model to approximate the ionization was needed that could be adapted to the results generated by the existing 3D computational code. Based on the wealth of previous work done by many in the field, it was decided the electron beam model provided a realistic approach to approximating the non-equilibrium ionization that could be readily adapted to the existing
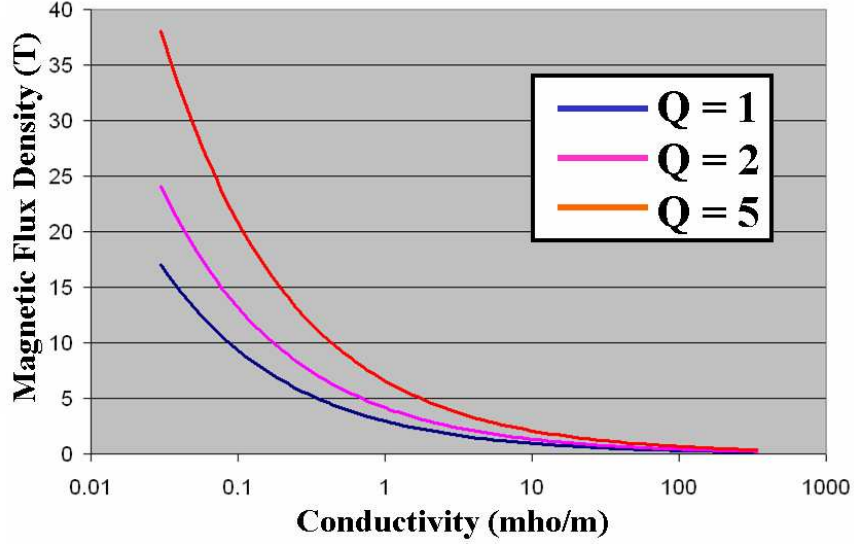
Figure 2.3:   Magnetic Field Requirements for Varying Q,σ

computational method. Specifically, the model of Kuranov and Sheikin [34–36] was used to determine the power spent on ionizing a unit volume of air, q_i, as given by Equation 2.74 where $j_b \approx 1.0$mA [45] is the electron beam current, e is the electron charge, ρ is the flow density and $Y(E_b) = 7.567$MeV-cm^2/gm is the electron stopping power as a function of the electron energy. This last quantity was taken from tabulated data for dry air with an electron energy of $E_b = 30$keV [1].

$$q_i = (j_b/e)\,\rho Y(E_b) \tag{2.74}$$

The resulting conductivity is found from Equation 2.75 where m_e is the electron mass, $k_e = 2 \times 10^{-8}$cm^3/s is the electron scattering constant [8], and n_e/N is an empirically-based expression for the ionization fraction as given by Equation 2.76 [36]. The number density, N, can be related to the density by $N = \left(\frac{RN_A}{R_u}\right)\rho$ where R is the specific gas constant, R_u is the universal gas constant, and N_A is Avogadro's number.

$$\sigma = \frac{e^2}{m_e k_e}\left(\frac{n_e}{N}\right) \tag{2.75}$$

2-26

$$\frac{n_e}{N} = 1.17 \times 10^{-5} \cdot \left(10^{34} \frac{q_i}{N^2}\right)^{0.6} \tag{2.76}$$

Having a value of q_i and σ at each point, it is a simple matter to integrate over the plasma volume defined by the modified Gaussian [21] to arrive at the total power required for ionization, P_{ion}, and an overall mean value for σ_0. Then Equation 2.77 is used to obtain a corresponding value for the mean magnetic flux density where the asterisked quantities are the non-dimensional values produced by the computational code. In a similar manner, the electrical power generated is simply found by integrating Equation 2.78 over the plasma volume.

$$(\sigma B^2)_0 = \left(\sigma^* B^{*2}\right) \left(\frac{\rho V}{L}\right)_0 Q \tag{2.77}$$

$$P_{gen} = \int \int \int \left(\bar{j} \cdot \overline{E}\right) d\left(Vol\right) \tag{2.78}$$

III. Scramjet Flowpath Development

3.1   Flowpath Design Methodology

The effort to construct a realistic flowpath began with gaining a deep understanding of the physical nature of scramjet flows. With regard to this goal, initial work focused on an in-depth literature review. Specific references are annotated where they were used, but there were also several sources of general information that proved invaluable [12, 13, 25, 27, 51, 64, 77]. Following this review was the creation of a quasi-1D computational scramjet analysis tool. This computational code was then applied to meet the requirements of a proposed Air Force program for a hypersonic vehicle with global reach. Various methods taken from the literature were then applied to convert the quasi-1D engine design to a 3D geometry. Finally, computational runs of the flowfield, to include a grid convergence study, were completed and an analysis of this model was conducted to determine where improvements to the geometry could be made subsequent to establishing the baseline performance model. This baseline model would become the starting point for the ensuing EM flow control reseach.

3.2   Quasi-1D Flowpath Design and Performance Analysis Code

The preliminary effort in developing the 3D engine flowpath focused on creation of a quasi-1D tip-to-tail scramjet engine analyzer that would both examine existing geometries and create optimum geometries through rapid parametric study.   The quasi-1D approach allows one to take advantage of much simpler analytical techniques while preserving the general nature of the scramjet flow physics. The approach used here followed that taken by William Heiser and David Pratt (H-P) [25]. In summary, for a given design point of free stream Mach number and dynamic pressure, the flow path is divided into three subsystems or components: compression, combustion, and expansion. The compression component is represented by a user-determined series of oblique shock waves that are constrained by keeping the isolator inlet temperature below a pre-determined maximum value. The combustion component is of the dual-mode type, that is the ram-to-scramjet transition is attained by creating a thermally

choked flow or "throat" within the combustion chamber. This dual-mode design consists of an isolator upstream of a fuel injection region, which is followed by a burner that may be modelled with either constant area or with built-in adverse pressure gradient relief. The expansion component is currently modelled by a simple adiabatic expansion process where the user specifies either the area or pressure ratio with respect to freestream. In addition to determining the detailed component thermodynamic states and variations in cross-sectional area along the axial coordinate, the tip-to-tail performance of the model is determined by performing a stream thrust analysis for the uninstalled specific thrust. From this primary relationship, other relationships provide various performance measures, including I_{SP} and engine efficiency.

The approach described above was implemented as a Fortran 95 code which was verified at the component level by comparing results with software available with the H-P text [25]. Figures 3.1(a) and 3.1(b) demonstrate this verification for the most complicated system, the dual-mode combustor. In these two figures, H-P's results from their *HAP Burner* design tool are depicted by the solid curves while the results of this research code are shown by the discrete symbols. The reference conditions for non-dimensionalization are taken at the isolator entrance (Station 2 in the figure legends). The minor differences in the results are attributed to the fact that the method of specifying the combustion heat addition was different than the method used by the *HAP Burner* software.

Some of the capabilities implemented in this approach, not available in the original *HAP* software, included:

1. combining the detailed component level and overall stream thrust analysis into a single simulation,

2. adding a capability to analyze constant area burners in the context of the overall flowpath analysis,

3. adding the ability to rapidly run parametric studies for any desired design variable,
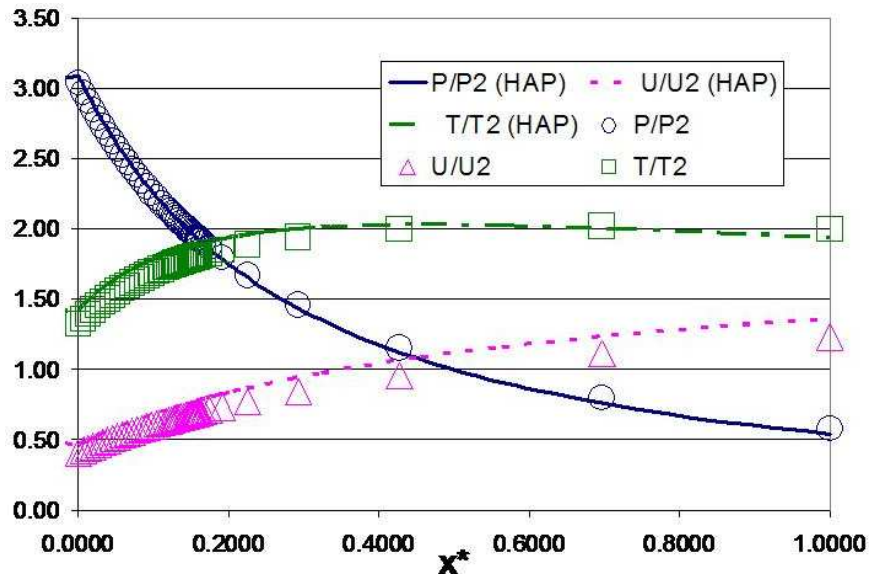
(a) Ramjet Operation. $M_0 = 7.2$
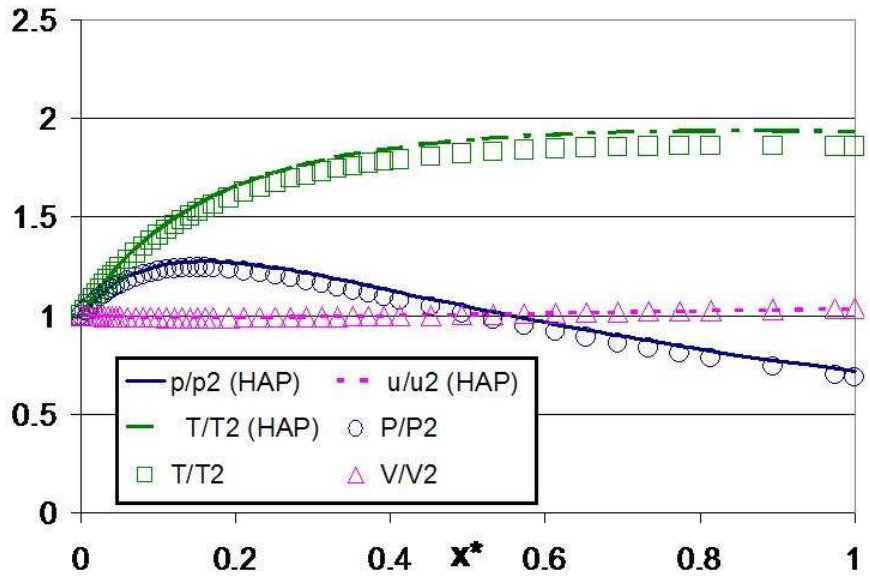
(b) Scramjet Operation. $M_0 = 12.0$

Figure 3.1: Comparison of HAP Burner Model to Quasi-1D Code for H_2-Air Combustion at Lean Conditions (f=0.02)

Table 3.1: Comparison of Quasi-1D and 3D Model Results at $M_0 = 8.0$

Station	Value wrt Free Stream	Quasi-1D Model	3D Model		% Difference from Q-1D Results	
			CL	Off CL	CL	Off CL
Isolator Entrance	P_2/P_0	35.6	31.50	34.0	-11.5	-4.49
	T_2/T_0	3.38	6.952	3.2	106	-5.33
	V_2/V_0	0.902	0.605	0.912	-32.9	1.11
	M_2	3.92	1.91	4.10	-51.3	4.59
Burner Entrance	P_3/P_0	86.4	43.70	49	-49.4	-43.3
	T_3/T_0	5.24	7.191	3.3	37.3	-37.0
	V_3/V_0	0.818	0.606	0.916	-25.9	12.0
	M_3	3.09	1.25	4.20	-59.5	35.9
Exit	P_4/P_0	86.4	58.55	58.2	-32.2	-32.6
	T_4/T_0	7.67	7.370	4.8	-3.91	-37.4
	V_4/V_0	0.842	0.749	0.894	-11.0	6.18
	M_4	2.43	2.08	3.31	-14.4	36.2
Expansion Exit	P_{10}/P_0	2.84	2.181	2.7	-23.2	-4.93
	T_{10}/T_0	3.44	3.225	1.75	-6.25	-49.1
	V_{10}/V_0	1.02	0.960	1.02	-5.88	0
	M_{10}	4.34	3.87	6.31	-10.8	45.4

4. and creating an enhanced input-output interface that supported graphical post-processing.

As an example of using these capabilities, the 3D model geometry previously published by Gaitonde (see Section 2.1) was simplified to quasi-1D by taking representative component cross-sectional areas along the axial coordinate. The quasi-1D code feature allowing analysis of existing geometries was then used to compare results with those obtained with the far more computationally expensive 3D CFD solver discussed in Chapter II. Results were calculated using identical reference conditions of $M_0 = 8$, $T_0 = 250K$, $P_0 = 1184Pa$, and $\gamma = 1.4$. Table 3.1 presents comparison data between these models with both centerline and off-centerline data collection taken from the 3D CFD results as presented in Figures 13 and 14 of Ref [21]. The percent difference was taken as the 3D value difference from the quasi-1D, divided by the quasi-1D value.

As can be seen in Table 3.1, the quasi-1D results agree very well in some places and not well in others, but all differences are readily explainable. The centerline results differ substantially at the isolator entrance; a discrepancy due largely to a centerline vortical structure that develops in the horizontal diffuser/isolator sections

of the 3D model [21]. This vorticity creates a relatively large momentum deficit along the centerline through the isolator and past the burner entrance and causes a corresponding local spike in temperature. Substantial differences occur within the burner itself, as well, primarily with higher static pressure values in the quasi-1D model. This is attributed to the different methods by which combustion is modelled. The quasi-1D model uses a semi-empirical polynomial of added total temperature as a function of axial location [Ref [25], Chapter 6]. This model predicts peak burner static temperatures to occur at the burner exit for a constant area burner. The heat addition in the Gaitonde model is represented by a Gaussian distribution of the heat release density source term in the energy equation [21]. This results in high centerline temperature values at the center of the distribution that rapidly fall off by burner exit. If the heat addition in the quasi-1D approach creates a large enough adverse pressure gradient to cause boundary layer separation, then the flow is considered to have an inviscid core region of constant pressure equal to the maximum pressure within the burner. This is what occurred in the case shown here and to a great extent explains why the quasi-1D burner pressure values are so much greater than their 3D counterparts. For such dramatic differences in computational method, the similarity of these results reinforces their validity and lends credibility to parameter studies such as the one discussed in the next example.

As a final result regarding this first example, the quasi-1D method was repeated allowing for distinct specific heat ratios for the compression, combustion, and expansion flowpath components, respectively ($\gamma_c = 1.36, \gamma_b = \gamma_e = 1.24$). The code has a tip-to-tail performance calculator built-in, and for all other inputs being equal, this change in gas properties from the constant $\gamma = 1.4$ case resulted in a performance loss of 7% in uninstalled specific thrust and overall engine efficiency.

As a second example, parameter studies of free stream Mach number from 5 to 25 at stoichiometric combustion were used to predict the performance envelope of the existing geometry. For reference purposes, the burner entry limits established by H-P of 0.5atm $< P_3 <$ 10atm were used [25]. The lower pressure limit is related to

the minimum pressure required for efficient mixing and combustion, and the upper pressure limit is for structural considerations. One additional limit is set on combustor exit temperature as well, that of $T_4 < 2500K$. This is also due to structural/material considerations.

For the same burner heat input used in the AFRL scramjet and component-specific γ, Figure 3.2 shows the envelope to be $M_0 = 5.0 - 11.5$, where the minimum pressure limit is reached. Note, that in this figure, τ_b represents the ratio of the combustor exit plane stagnation temperature to its inflow plane value. Within this envelope, the uninstalled specific thrust and overall engine efficiency ranged from $132.4 - 184.6$m/s and $0.056 - 0.187$, respectively. No other limit was approached and as the figure shows, significant additional heat input could be applied in the burner to improve performance. This, in fact, was done, and the results are presented in Figure 3.3. In this case, the only change was the application of the maximum amount of heat the burner geometry could handle without thermally choking. Even so, the model geometry would not support ramjet mode below $M_0 = 7.4$ due to inlet unstarting. Although performance above $M_0 = 7.4$ was much higher than the previous case, it should be obvious from Figure 3.3 the burner geometry allows a far greater heat input than the structure could withstand, i.e. T_4 is > 4000K along the entire range. Therefore, a final computation was obtained wherein the applied burner heat was limited such that the T_4 limit wouldn't be exceeded.

Figure 3.4 shows the results of limiting the burner exit temperature to a more realistic 2500K. The same issues exist as in ramjet mode, thus the performance envelope extends from $M_0 = 7.4$ up to $M_0 = 12.3$. Substantial improvements in performance over the baseline case were seen with the uninstalled specific thrust and overall engine efficiency ranging now from $442.5 - 218.0$m/s and 0.282–0.238, respectively.

For all of these cases, the performance remained lower than the analytical results suggested by Heiser and Pratt's work, so as a final example the quasi-1D code was executed using a feature allowing an optimum geometry to be determined for the
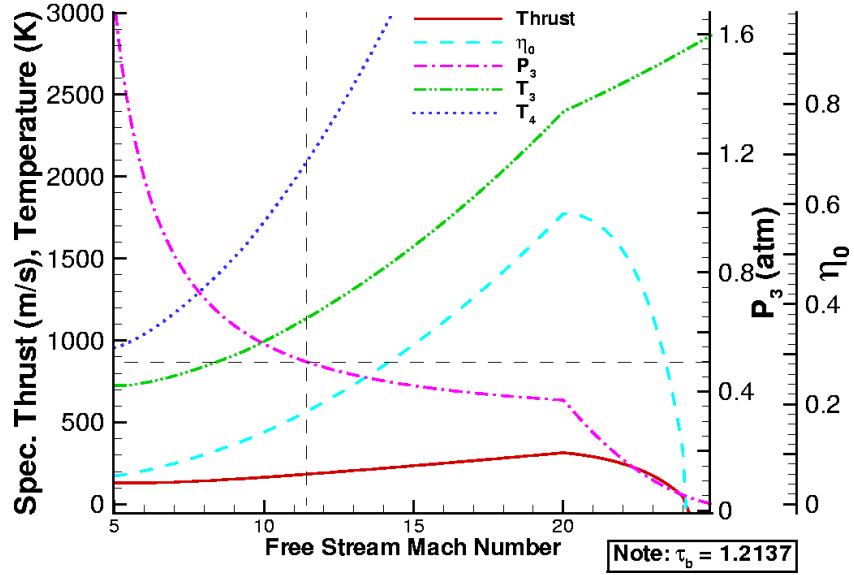
Figure 3.2:   Performance Envelope for AFRL Engine as given by Author in AIAA 2003-0172.
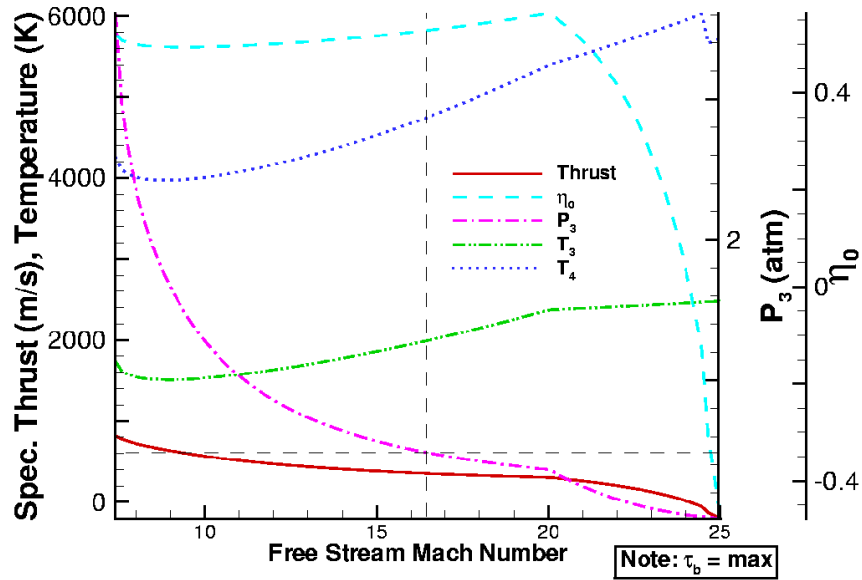
Figure 3.3:   Performance Envelope for Engine as given by Author in AIAA 2003-0172 except maximum heating applied in burner.
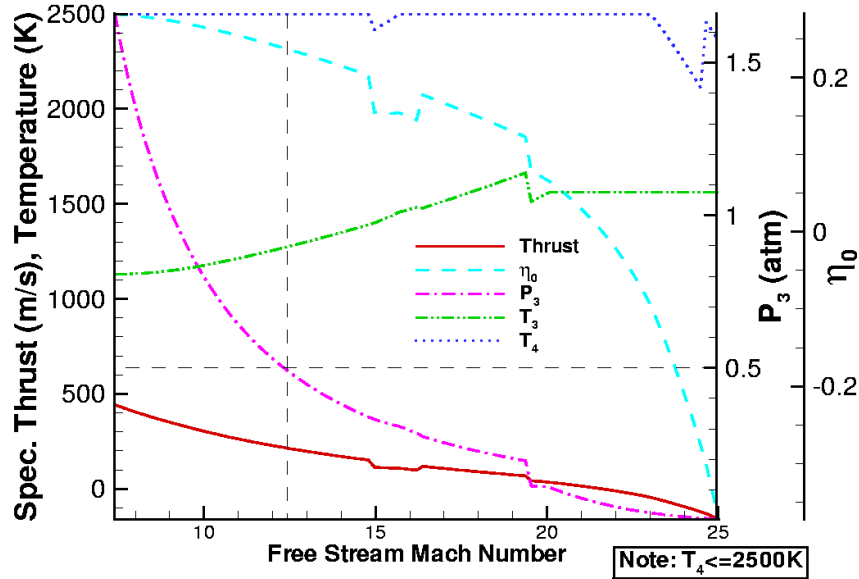
Figure 3.4: Performance Envelope for Engine as given in AIAA 2003-0172 except maximum burner temperature capped at 2500K.

identical free stream conditions presented in Reference [21]. Table 3.2 is a summary comparison of the geometry and performance of two optimized geometries to the baseline model of Figure 3.2. The first optimized geometry used the same heat input as the baseline case, and the second optimized geometry increased the heat input such that $T_4 = 2500K$. This final geometry was then held fixed and its performance envelope was determined as shown in Figure 3.5.

Table 3.2: Quasi 1D Method Comparison of Baseline and Optimized Geometries

Station	Value wrt Free Stream	Baseline Model ($\eta_b = 1.2137$)	Optimized Geometry ($\eta_b = 1.2137$)	Optimized Geometry with T4 = 2500K
Isolator				
Entrance	A_2/A_0	0.1053	0.0296	0.0296
Burner				
Entrance	A_3/A_0	0.1053	0.0296	0.0296
Exit	A_4/A_0	0.1053	0.0764	0.0764
Expansion				
Exit	A_{10}/A_0	1.233	3.212	3.821
Performance				
Spec Thrust	(m/s)	143.7	264.0	498.9
Efficiency		0.0994	0.191	0.387
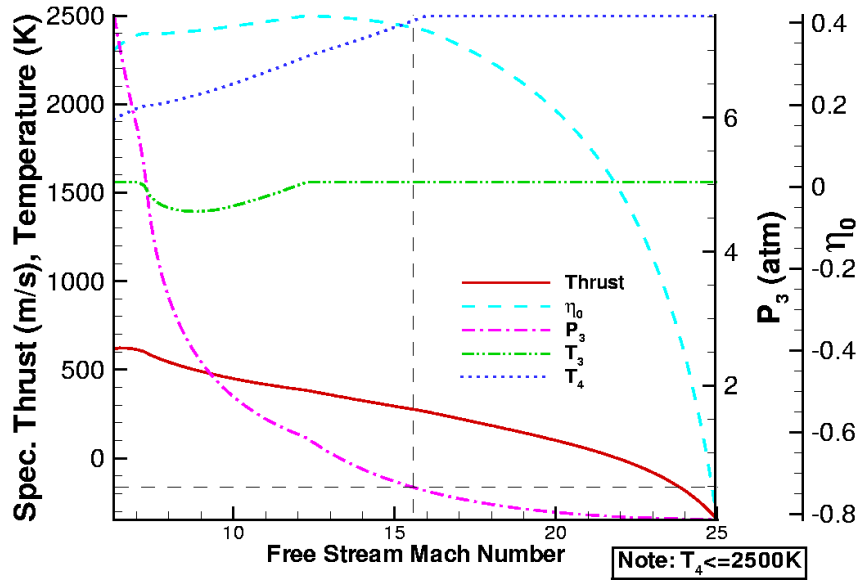
Figure 3.5: Performance Envelope for optimized geometry engine with maximum burner temperature capped at 2500K.

With optimized geometry, the overall performance envelope was extended from $M_0 = 6.3$ to $M_0 = 15.3$. Substantial improvements over the baseline case were seen with uninstalled specific thrust ranging now from $619.4 - 282.8 \mathrm{m/s}$ and peak overall engine efficiency of 0.417 occurring at $M_0 = 12.23$. The quasi-1D design tool, though simple in concept, proved itself invaluable in providing the physical insight necessary to optimizing the 3D, flight scale model. Further discussions of this quasi-1D analysis as it pertained to development of the model geometry may be found in Sections 3.3 and 3.4.

3.3 Vehicle Sizing to Support the Military Spaceplane Concept

The first step in designing a flight-scale geometry was to determine what requirements such a scramjet powered vehicle would have. Because the point of this research is not to perform the systems analysis to design an entirely integrated vehicle, the decision was made to use existing mission requirements for a concept of Air Force interest and estimate what scramjet engine performance would satisfy them. The concept chosen for this research was the Military Spaceplane (MSP) which was

established in the mid-1990s as an effort to have industry develop the technology that was required for operationally responsive space access [82]. The program was to have four demonstration phases that would continually improve on key performance parameters such as payload delivered to orbit.

The pertinent requirements used for this research correspond to the MSP Mark I, or non-orbital, demonstrator [82]. Specifically, these were to have a payload bay of size 10'x5'x5', with a weight capacity of 10,000 lbs (4540 kg), and the ability to deliver at least 1-3klbs to any terrestrial location. In addition, the vehicle was to have a sub-orbital "pop-up" capability of approximately Mach 16 at 300kft. To meet these requirements, it was decided to size the engine for a hypersonic cruise configuration at a design point of M_0=10 and q_0=1000lb/ft^2($\sim$ 48kPa), where q_0 is the freestream dynamic pressure. Hypersonic vehicles tend to be optimized for a q_0 in the range of 500–2000lb/ft^2(20 − 95kPa) [25]. Exceeding the high end of this range would cause excessive vehicle drag and heating, and on the low end it would be very difficult to generate enough lift with a reasonably-sized wing area. The freestream Mach number was chosen on the bases that it would ensure scramjet operation vice ramjet or dual-mode operation and that it would be operationally responsive. For example, an unrefueled flight from New York to Melbourne, Australia ($\sim$ 10,000mi or 16,700km) could be accomplished in approximately 1.5 hours. Because the cruise speed chosen exceeds the typical maximum operating speed of a hydrocarbon-fueled scramjet, hydrogen was chosen as the fuel. The remaining freestream conditions corresponding to this design point were calculated by the quasi-1D code, using the 1976 Standard Atmosphere. These are presented in Table 3.3. Note, the stream thrust definition used is the ratio of the uninstalled thrust, F, to the freestream air mass flow rate into the engine, $\dot{m}_0$. These were the design point conditions which served as the basis for the quasi-1D optimum engine sizing described in the following paragraphs.

The essence of sizing the vehicle's scramjet was determining the total thrust needed to meet the performance specifications, in turn leading to the required mass

Table 3.3:   Freestream Properties at Design Point

Freestream Property	Value
Pressure, P	684 Pa
Temperature, T	233 K
Density, ρ	0.0102 kg/m^3
Velocity, V	3061 m/s
Streamthrust, S	3083 m/s
Altitude, h	33.8 km

capture area. The method used was taken from Chapter 3 of Heiser and Pratt's text [25] and relied on developing the Breguèt Range Equation. The fundamental assumption is for unaccelerated cruise flight over a "flat" earth, which results in balancing the drag, D, to the installed thrust, T, which is less than the uninstalled thrust by the factor, D_e (the external drag due to the engine installation on the airframe). This is reflected in Equation 3.1, where $\phi_e = D_e/F$ is commonly referred to as the engine installation penalty.

$$T = D = F - D_e = F(1 - \phi_e) \tag{3.1}$$

Incorporating the definition of overall engine efficiency, η_0, (i.e. the ratio of the thrust power generated by the engine to the rate chemical energy released by combustion), Equation 3.1 can be recast as:

$$T = D = \frac{\eta_0 h_{pr}(1 - \phi_e)}{V_0} \dot{m}_f \tag{3.2}$$

where h_{pr} is the potential combustion heat released by the given fuel and $\dot{m}_f$ is the fuel mass flow rate. The fundamental assumption also implies lift, L, equals weight, mg_0. Additionally, $V_0 = dR/dt$, where R is the vehicle range. Since, by definition, $C_L/C_D = L/D$, this can be rearranged as $D = (mg_0) \cdot C_D/C_L$. Equation 3.2, therefore, is equivalent to:

$$mg_0 \frac{C_D}{C_L} = \frac{\eta_0 h_{pr}(1 - \phi_e)}{dR/dt} \frac{dm_f}{dt} \tag{3.3}$$

Finally, noting the fuel flow rate in the previous equation is the same as the rate at which the vehicle mass is decreasing (i.e., $dm_f/dt = -dm/dt$), Equation 3.3 can be rearranged to provide the governing differential equation for thrust power versus drag:

$$\frac{dm}{m} = -\left[\frac{g_0}{\eta_0 h_{pr} \left(1 - \varphi_e\right) \frac{C_L}{C_D}} \right] dR = -C_1 dR \tag{3.4}$$

If the term C_1 is a constant, which is a good first order approximation for the fundamental assumption given, then the solution to 3.4 is the Breguèt Range Equation:

$$\frac{m_{final}}{m_{initial}} = e^{-C_1 R} \tag{3.5}$$

Introducing the concept of fuel mass fraction, $\Pi_f = \frac{m_i - m_f}{m_i}$, Equation 3.5 can be rearranged one last time to get:

$$\eta_0 = \left[\frac{g_0 R}{h_{pr} \left(1 - \varphi_e\right) \frac{C_L}{C_D} \ln\left(\frac{1}{1 - \Pi_f} \right)} \right] \tag{3.6}$$

or in terms of the uninstalled specific thrust, $\frac{F}{\dot{m}_o}$, and the fuel-to-air mass flow ratio, f,

$$\frac{F}{\dot{m}_o} = \left[\frac{f g_0 R}{V_0 \left(1 - \varphi_e\right) \frac{C_L}{C_D} \ln\left(\frac{1}{1 - \Pi_f} \right)} \right] \tag{3.7}$$

To solve Equations 3.6 and 3.7 a few conditions beyond the design point needed to be decided. First, the range was set at 10,000 miles to satisfy the MSP requirements [82]. For molecular hydrogen fuel, $h_{pr} = 1.2 \times 10^8 \, \text{J/kg}$ and $f = 0.029$ for stoichiometric conditions. Finally, $(1 - \phi_e)\frac{C_L}{C_D} = 5$ was assumed in accordance with Heiser and Pratt [25]. With these factors in place, a short parameter study was undertaken to discover the threshold performance values that would satisfy Equations 3.6 and 3.7 for a range of Π_f. Based on this study, the results of which are reproduced in Ta-

Table 3.4:   MSP Scramjet Threshold Performance Values

$F/\dot{m}_o$ (m/s)	η_0	Π_f
1047	0.921	0.25
844.9	0.743	0.30
699.5	0.615	0.35
589.9	0.519	0.40
504.0	0.443	0.45
434.7	0.382	0.50
377.4	0.332	0.55

ble 3.4, $\Pi_f = 0.55$ was selected as it required the lowest engine performance while maintaining a fuel mass fraction comparable to modern long range military combat aircraft. Assuming the empty (structural) mass fraction is $\Pi_e = 0.30$, the remaining payload fraction must be $\Pi_p = 0.15$.

Increasing the MSP requirements for payload mass by a factor of 75% for added margin and knowing the payload mass fraction, $\Pi_p = 0.15$, the problem was worked back to the final engine size. First, the total vehicle mass was found to be 52,880 kg (or about 60% that of a Boeing 727-200 commercial jet). Then from the unaccelerated cruise flight and $(1 - \phi_e)\frac{C_L}{C_D} = 5$ assumptions, the total vehicle drag was found to be $93,468$N. Thus, by Equation 3.1 where an installation penalty of $\phi_e = 0.1$ was assumed, the minimum uninstalled thrust required to complete the mission was found to be on the order of 103,850N. Dividing this by the threshold value for uninstalled specific thrust, $\frac{F}{\dot{m}_0}$, the minimum mass flow of air was found to be $\dot{m}_0 = 275.2$(kg/s). Finally, the steady, one-dimensional form of the continuity equation (3.8) for the freestream conditions was used to arrive at the minimum freestream mass capture area, $A_0 = 8.797$m^2. With this area known, the 3D geometry design process was begun.

$$\rho_0 A_0 V_0 = \dot{m}_0 \tag{3.8}$$

3.4   Construction of a Flight-Sized 3D Flowpath Geometry

3.4.1   Pertinent design conditions from quasi-1D results.   The construction of the 3D geometry began with a parameter optimization study of quasi-1D configurations for the design point discussed in Section 3.3. This was done in consultation with scramjet experts in AFRL's Propulsion Directorate (AFRL/PR) [41]. Results from the quasi-1D code of this research were compared to an existing AFRL/PR code which included a simple chemistry model for hydrogen combustion [41]. From this collaboration several model parameters were established. First, it was decided to limit the inlet and combustor static temperatures to 1700K and 3000K, respectively, to prevent excessive molecular vibration and dissociation losses. Similarly for the combustor, at temperatures greater than 3000K, most of the heat of combustion is lost to these same molecular modes. When this occurs, the added heat energy can not be effectively recovered during the mostly frozen expansion process. In addition, based on the combustor flow chemistry results of the AFRL/PR code, it was decided to change the specific heat ratio and gas constant in the combustor of this research code from $\gamma_b = 1.238$ to $\gamma_b = 1.223$ and $R_b = 287$ Joule/(kg–Kelvin) to $R_b = 314.5$ J/(kg–K). When these changes were inserted, the two independent codes produced nearly identical results for the same design point. Finally, with the added confidence in the quasi-1D results, a two-parameter variation study was performed wherein 100 cases were run for maximum allowed inlet and combustor temperatures in the range of 1200-1700K and 2500-3000K, respectively. All cases were run for a constant pressure combustor geometry, that is the combustor cross-sectional area expands in the streamwise direction to balance the pressure rise due to total temperature increase and prevent thermal choking. The results of this study can be seen in Figure 3.6 for η_0 and Figure 3.7 for the actual maximum burner temperature that occurred.

An analysis of these two figures quickly led to a conclusion of an optimum starting point for designing the 3D geometry. From Figure 3.7, it was seen that on the low end of peak inlet temperature, the flow was undercompressed and for a constant pressure burner geometry it was not possible to approach peak allowable combustor

3-14
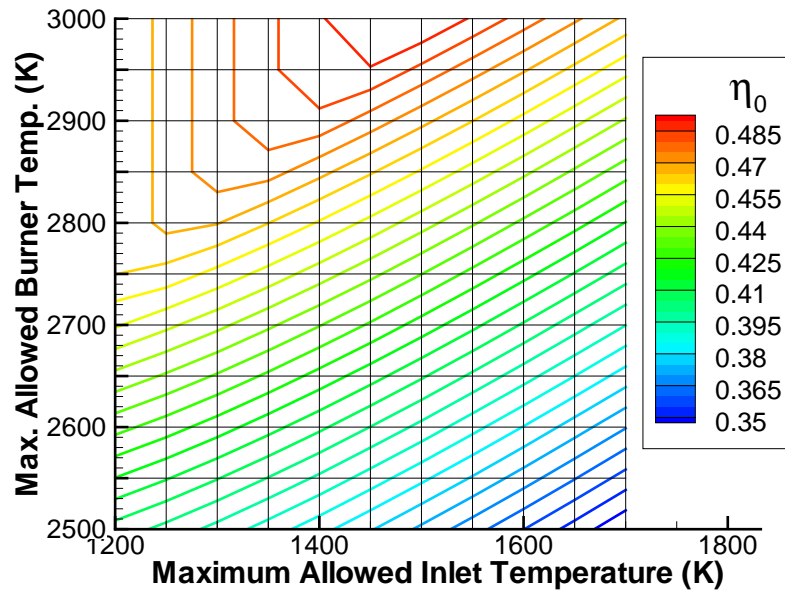
Figure 3.6:   Overall Efficiency Contours for 2-Parameter Study of Mach 10 Engine
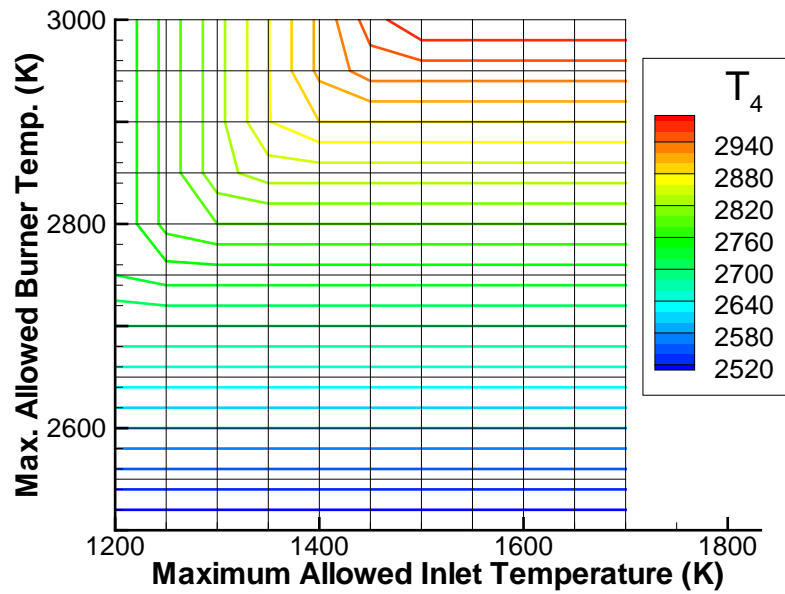
Figure 3.7:   Combustor Exit Temperature Contours for 2-Parameter Study of Mach 10 Engine

temperature. In fact, this condition held until inlet temperatures reached around 1450K. In addition, a review of Figure 3.6 revealed that peak engine efficiencies occurred in the range of $1300 - 1550K$ for peak inlet temperatures. Therefore, assuming there was still some level of uncertainty in the quasi-1D code and erring on the conservative side, it was decided to take as the starting geometry that case which produced a peak inlet temperature of 1300K and combustor temperature of 2850K.

3.4.2 Design of the 3D inlet.

"The goal in the design of any hypersonic inlet system is to define a minimum weight geometry that provides an efficient compression process, generates low drag, produces nearly uniform flow entering the combustor, and provides these characteristics over a wide range of flight and engine operating conditions [13]."

With this in mind, several potential designs and their implications were considered in the course of the literature review on this topic. As a small sampling of this review, VanWie and Ault performed several experiments on a blunted 5° wedge followed by 5° of isentropic compression and a single cowl lip shock to realign the flow [3]. All compression was performed in the pitch plane only. They showed that several factors including Reynold's number, leading edge bluntness, and wall cooling directly impacted the boundary layer thickness, playing a vital role in determining the placement of the cowl lip shock and the extent to which it was cancelled on the inlet expansion shoulder [3, 80]. Holland devoted his dissertation to the experimental and numerical study of sidewall compression inlets, demonstrating among other things the improvement in startability attained by sweeping the sidewall leading edge [27, 28]. The results of his research have seen practical application in the design of the X-43A [29]. Finally, Mahoney's text, *Inlets for Supersonic Missiles*, provided an excellent reference for design methodology [51].

In the end, the design approach for the inlet followed that of Mahoney, using a combination of results from the quasi-1D case previously selected and scaled sizing of the published data for the X-43A [6] and its publicly released cousin, the Hyper-
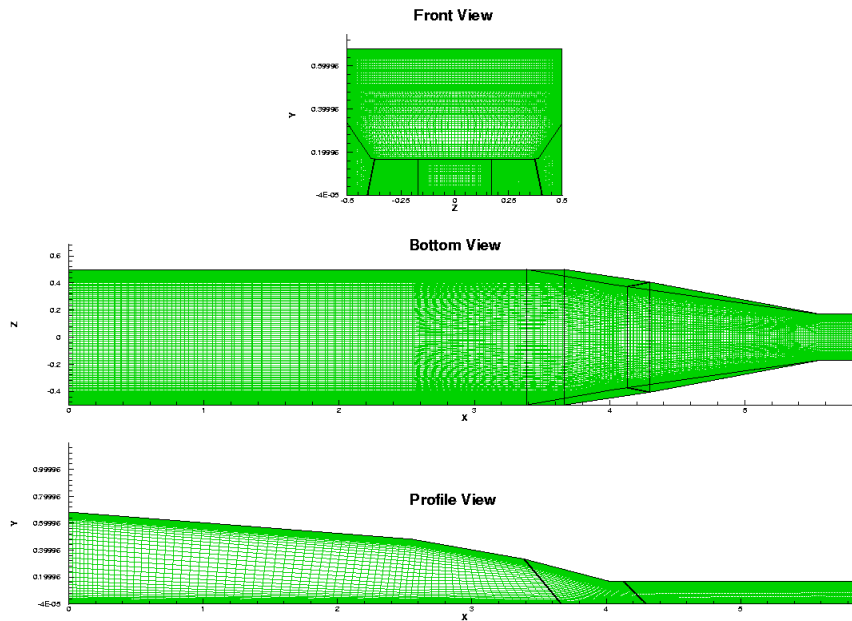
Figure 3.8:   Scramjet Inlet Grid Normalized by Freestream Capture Width

X [72]. It was determined from this that the inlet (see Figure 3.8) would be of mixed external-internal compression. The freestream capture area was already determined to be 8.797m^2 which was defined as a rectangle in the Y-Z plane of 2.442m×3.602m. Note, the width of the freestream capture area also served as the reference length, L_0, for non-dimensionalization purposes. External compression came from three pitch plane ramps of 4.5°, 5.5°, and 3° which was identical to the X-43A when that vehicle's flight angle-of-attack was included. Sidewalls with a 45° leading edge sweep and 9.24° of lateral compression were placed just downstream of the expansion shoulder. This sidewall compression continued until reaching the inlet throat which had a cross-sectional area of 0.6m×1.22m, for an overall inlet contraction ratio of 12, which is within the operating limits for Mach 10 as presented by VanWie [13]. The overall inlet length from tip-to-throat was calculated to be 20.522m, 5.242m of which was totally internal flow from the cowl lip to the throat, which also served as the interface with the constant area isolator.

3.4.3 Design of the 3D isolator/combustor. It became quickly apparent in the literature review that the most widely studied and versatile scramjets had *dual-mode* combustion elements. A dual-mode scramjet is one that can be made to operate as either a ramjet or scramjet. This is made possible by two design concepts: the thermal throat, which is only needed for ramjet flow, and the isolator. The thermal throat works by varying the heat input into the aft end of the combustor (e.g. by adding fuel injectors further downstream in the combustor), thus modulating the local pressure and thereby constricting or relaxing the core burner flow as needed to maintain subsonic flow in the combustor. Optimum design of a thermal throat mechanism for a particular dual-mode scramjet application is beyond the scope of this work and will not be discussed further. For both modes, however, the isolator plays an important role, increasingly so for lower Mach numbers such as those typically encountered in engine starting. Simply put, the first purpose of the isolator is to prevent combustion-induced pressure instabilities from propagating upstream (in the boundary layer for supersonic flow) into the inlet and causing inlet unstart. A second role is to allow the flow to transition from the lower pressures of the inlet throat to the higher pressures of the combustion chamber by passing through a series of oblique shocks. As can be seen in Equation 3.9 [25], the isolator length-to-height ratio increases inversely with inlet Mach number, M_i, and directly with the combustor-to-inlet pressure ratio, p_e/p_i. The isolator length for this 3D geometry was determined by applying Equation 3.9 to the inlet throat conditions that would exist at ramjet speeds ($\sim M_0 = 6$), and then rounding up to 2.80m to be conservative.

$$\frac{L}{H} = \frac{\sqrt{\frac{\theta}{H}}}{\sqrt[4]{Re_\theta}} \frac{\left\{ 50 \left(\frac{p_e}{p_i} - 1 \right) + 170 \left(\frac{p_e}{p_i} - 1 \right)^2 \right\}}{(M_i^2 - 1)} \tag{3.9}$$

It was also readily obvious from the literature the *constant-pressure* combustor offered greater performance than the constant-area design. By allowing the combustor cross-sectional area to increase in the flow direction, the adverse effects of the combustion-induced pressure rise could be somewhat mitigated. For a given heat ad-

dition profile and combustor inlet pressure (shown in the equation below in terms of total temperature, T_t, and Mach number), the quasi-1D code integrated the generalized differential equation given by Equation 3.10 [25] to obtain the axially varying cross-sectional area profile. For the case under study, the resulting ratio of combustor exit to inlet area was 2.1 and the corresponding pressure ratio was 1.03. To achieve the desired area ratio, a rectangular cross-section was maintained and was increased equally in the $+Y$ and $\pm Z$ directions (see Figure 3.9). The $-Y$ dimension wasn't changed to maintain a constant cowl contour. A $2°$ divergence angle was chosen for the remaining sides as a balance between a reasonably short combustor length and minimizing combustor flow divergence from the axial direction. Thus, the overall combustor length, from the beginning of the divergence to the beginning of the internal expansion nozzle was found to be 7.881m. The combustor exit plane cross-sectional area was 0.871m×1.766m.

$$\frac{dM}{dx} = M \left(\frac{1 + \frac{\gamma_b + 1}{2} M^2}{1 - M^2} \right) \left\{ -\left(\frac{1}{A} \frac{dA}{dx} \right) + \frac{1 + \gamma_b M^2}{2} \left(\frac{1}{T_t} \frac{dT_t}{dx} \right) \right\} \tag{3.10}$$

Between the isolator and the diverging section of the combustor, 10cm of constant area duct was included for the fuel injectors. Numerous possible fuel injection and mixing designs have been proposed for scramjets. Some of these include, strut-mounted, backward facing steps, ramp injectors, and channel or cavity flow mixers [2, 4, 5, 15, 24, 32, 56]. Because the computational code required a stuctured-grid, it was decided to use a simplified slot injector and forego the complexity of a flameholding cavity or similar device. Sizing the fuel injectors began with determining the total fuel flow rate required by using the stoichiometric fuel-to-air ratio, $f = 0.029126$, and the mass flow rate of air, $\dot{m}_a$, entering the combustor. The latter amount was determined to be $\dot{m}_0$ minus any air spillage around the inlet cowl, which during the inlet flow control analysis (see Chapter V) was found to be approximately 60kg/s. Thus, the required fuel mass flow rate was $\dot{m}_f$=6.3kg/s. From a thermody-
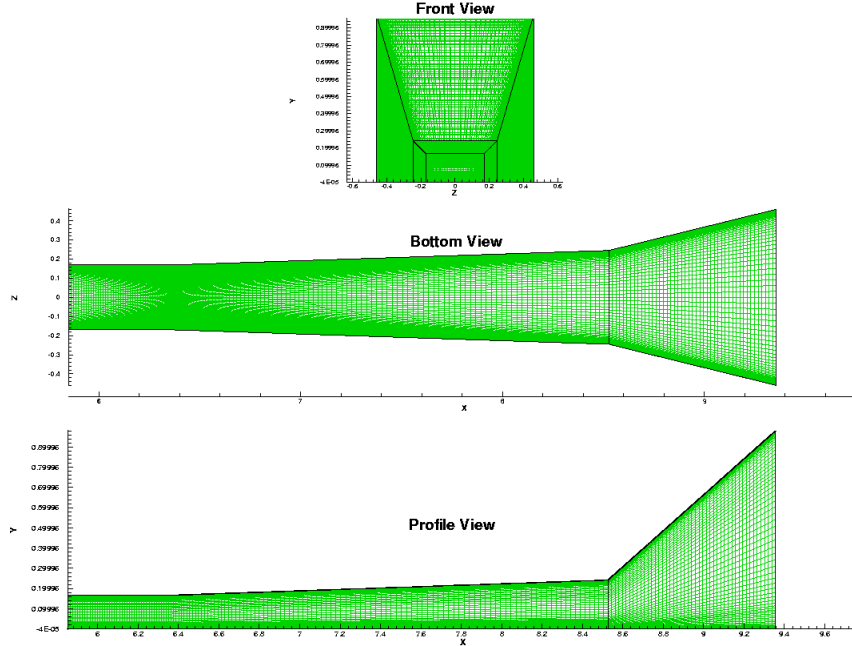
Figure 3.9:   Scramjet Isolator-Combustor, Internal Nozzle Grid Normalized by Inlet Width

namic standpoint, the fuel was assumed to enter the combustion chamber at similar conditions to those specified in the experimental work given by Goyne, et al [24], such that V_f=2200m/s and P_f=290kPa. Two cases for fuel temperature were considered, T_f=290K and T_f=800K, such that using hydrogen's specific gas constant of R=4124.5J/kg–K and Equation 2.14 resulted in fuel densities of ρ_f=0.2425kg/m^3 and 0.08789kg/m^3, respectively. The injectors were placed on both the top and bottom of the duct and oriented symmetrically about the Z-midplane. The continuous slot injector had dimensions of approximately 1.0×0.013m and was injected at an angle of 27° with respect to the axial flow direction in order to reduce the shock-induced losses due to the impinging fuel stream.

3.4.4   Design of the 3D expansion nozzle and thrust surface.   Although isentropic expansion through a method of characteristics solution to the fluid flow equations provides the greatest recovery of the total flow energy, the length and final cross-sectional area of such a system is unrealistically large. Fortunately, the

majority of the flow energy may be recovered in the initial turning angle, ω, given here by Equation 3.11 [25], where the subscript b, e corresponds to the conditions at the combustor exit and subscript y would be the Mach number at the expansion system exit plane if it were isentropically expanded to freestream. From the quasi-1D estimate for this design, $\omega \simeq 42.02°$, which is clearly visibly at the aft end of Figure 3.9. Although this research focused on the uninstalled engine performance, some limitation must be placed on the total cross-sectional area and thrust surface length at the expense of not expanding fully to free-stream conditions. For this model, it was assumed the engine was centered longitudinally on the overall vehicle center-of-gravity. Thus, it was possible to determine the allowable length of the thrust surface from knowing the lengths of all the other engine components. This length between the combustor exit plane and the end of the thrust surface was found to be 20.5m. A quasi-1D parameter study revealed performance gains diminished rapidly for area ratios, $A_e/A_0 > 2.5$ where the subscript e refers to the expansion surface exit plane area. Finally, a small amount of lateral expansion out of the combustor was allowed to return the width to that found at the cowl lip plane.

$$\omega = \frac{1}{2}\sqrt{\frac{\gamma_e+1}{\gamma_e-1}} \left\{ \tan^{-1}\sqrt{\frac{\gamma_e-1}{\gamma_e+1}\left(M_y^2-1\right)} - \tan^{-1}\sqrt{\frac{\gamma_e-1}{\gamma_e+1}\left(M_{b,e}^2-1\right)} \right\}$$
$$-\frac{1}{2}\left\{ \tan^{-1}\sqrt{\left(M_y^2-1\right)} - \tan^{-1}\sqrt{\left(M_{b,e}^2-1\right)} \right\} \quad (3.11)$$

3.5 Computational Grid Considerations and Convergence Study Results

The grids employed were designed carefully to limit uncertainty in the results analysis while still achieving reasonably fast computational times. Because these structured grids were also designed from the beginning to work with viscous flow, this necessitated a great number of points in the boundary layer. The distribution of points in the boundary layer was initially done in accordance with the work of

Table 3.5:   3D Computational Mesh Sizes

Grid	Dimensions ($\xi \times \eta \times \zeta$)	Total Points
Fine Mesh		
Inlet	$178 \times 112 \times 143$	$2,850,848$
Combustor/Nozzle	$187 \times 112 \times 143$	$2,994,992$
Coarse Mesh		
Inlet	$178 \times 57 \times 71$	$720,366$
Combustor/Nozzle	$187 \times 57 \times 71$	$756,789$

Vassberg, et al [81], utilizing a normalized value of $\Delta s = 5.0 \times 10^{-6}$ off the wall. The grids developed in this manner are referred to as the 'fine mesh.' Computational runs of these fine meshes on a Cray X1E supercomputer still required three or more weeks to converge a solution. The grids were coarsened to a point that cut the computational time to less than half while preserving the flowfield solution. The resulting grid dimensions and total size of each mesh are presented in Table 3.5.

Figure 3.10 demonstrates the coarse mesh spacing did indeed accurately capture the fine mesh results. In the subfigures, selected flow properties as determined by the cross-sectional area-weighted method of Section 2.6 are presented. As can be seen, all differences between the two solutions are less than a few percent. Both solutions were ran to the approximate steady state solution as determined by negligible changes in the computed residual and the flow properties as typified by Figure 3.10. Minor differences seen between the two grid sizes are attributed to both the presence of sidewall vortices and other three-dimensional phenomena that prevent truly steady flow from being obtained as well as the difference in grid spacing. In the end, it was felt the significant improvement in computational speed was worth the slight difference in results seen here.

3.6   Summary

At this point, the majority of the background review and research has been presented. The key physical processes common to scramjet engines have been explored and incorporated into the development of a first-of-its-kind open source scramjet

Inlet Grid Comparision Using Static Pressure

(a)

Inlet Grid Comparision Using Mach Number
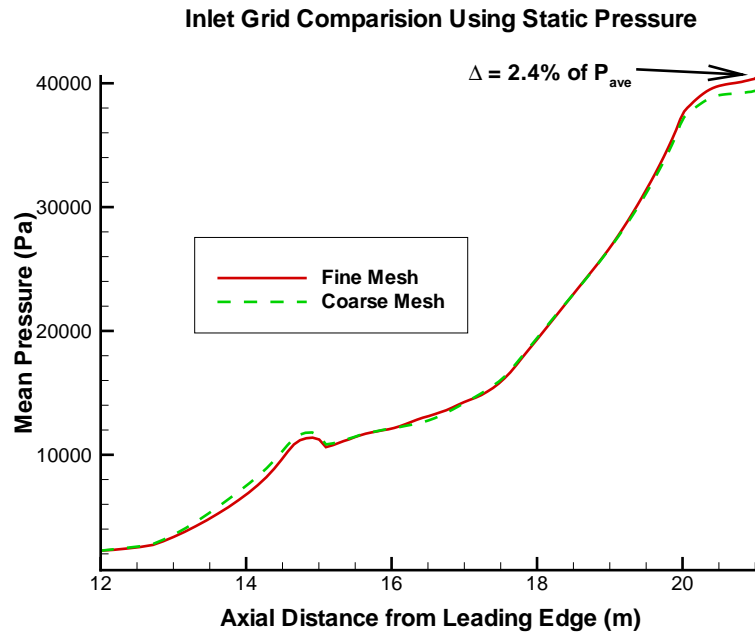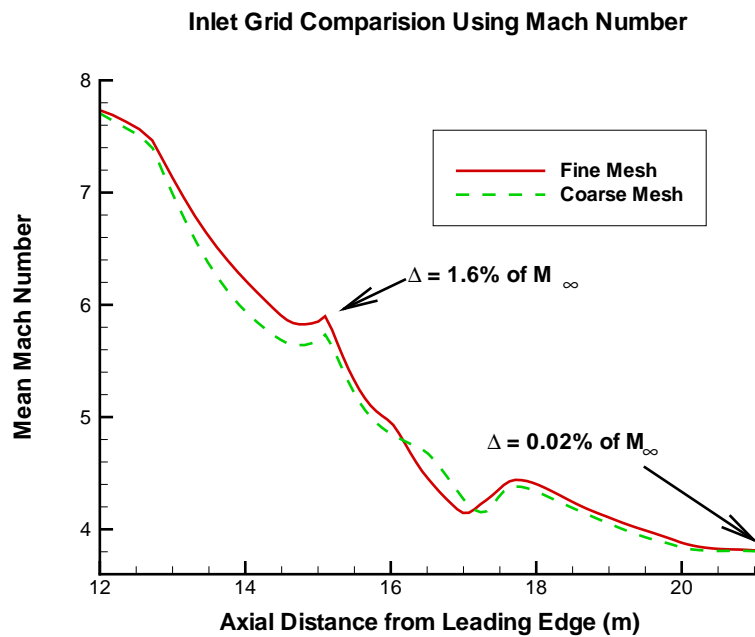
(b)

Figure 3.10:   Grid Convergence Comparison Using Internal Portion of Scramjet Inlet
(a) Difference in pressure normalized by the average of the two values.
(b) Difference in Mach Number normalized by the freestream value.

geometry. First, this was done through the development of the quasi-1D design tool and then to a higher level of detail through the 3D baseline geometry design process. Integral to this effort was sizing the engine to support the requirements of the Military Spaceplane concept. Detailed computational analysis of this engine model will now be presented in the context of the thermochemistry model developed in Chapter IV, the localized flow control explored in Chapter V, and the MGD energy bypass concept study of Chapter VI.

IV. Inclusion of a Thermochemistry Model

4.1   Introduction

Thermochemistry models vary greatly in their complexity and computational expense, ranging from simple curve fits for a constant composition gas, to detailed mass balancing, finite rate reaction mechanisms that include molecular vibration, dissociation, and ionization models. Until very recently the research code used in this work was severely limited with respect to scramjet simulations by the major assumption that the gas was of constant composition and calorically perfect. Furthermore, chemical combustion could only by represented by a simple, heating rate source term in the energy equation. Work done by Earp in 2004 partially addressed the calorically perfect assumption by putting in place a fourth order polynomial curve fit of γ for air that is valid from $50 - 3400K$ [17]. This assumption greatly improved results in cases not involving combustion (e.g. within inlet diffusers), but once fuel was introduced in the combustor this model was no longer valid. Therefore, a major goal of the current research effort was to incorporate a thermochemistry capability into the computational model. This was achieved with the development and verification of a loosely coupled algorithm with the ability to use any finite rate chemical reaction model. However, only two models for hydrogen-air combustion were explored for this research; a quasi-global 2-reaction model [68,79] and a reduced set of 8-reactions [18]. Both models compared favorably with previously published unit problems, but the global model was both computationally slower and in some instances less accurate [38]. Therefore, only the 8-reaction model was incorporated into the scramjet and presented here. Finally, as described in Subsection 3.4.3, a simple, slotted fuel injector was used to introduce the fuel into the airstream. The fuel-injected combustor was compared with both a "cold flow" combustor (i.e. one with no applied heating) and one using the heating rate source term formulation. Based on the results presented in Section 4.4, the fuel-injected model was chosen as the baseline engine for the MGD bypass and combustor-based MGD generators presented in Chapter VI.

4.2 Coupling Thermochemistry with the Computational Code

While many current CFD codes address chemical kinetics in some way, until now there have not been any coupled to an MGD solver and applied to a scramjet flowpath. In addition, the kinetics models that are currently in use vary greatly in their complexity and computational expense and are tailored to specific applications.

Therefore, a portion of the research was devoted to implement a thermochemistry model that addresses all the above issues. The overall goal was to accurately and efficiently calculate the heat release and final composition of a mixture, but not necessarily enforce time accuracy. Additionally, the chemistry model would be implemented in such a way that the code could operate with or without its use, as required. Because of this, a loosely coupled approach somewhat similar to that followed by Hoffman and Chang [26] was taken, where across a given time step the MGD flow equations (Eqns 2.40 - 2.42) were solved separately from the species conservation equation (Eqn 2.13). The subsequent change in chemical composition due to the change in the flow state and chemical reaction was then used to update the mass-averaged thermodynamic properties for the ensuing flow step. A general outline of the algorithm is:

1. Initialize flow variables and chemical composition at each point.

2. At each time step, solve the flow equations, assuming a constant chemical composition. The resulting mixture pressure, p, as well as the mass fluxes, ρu, ρv and ρw, will be considered invariant across the following chemistry step.

3. Calculate the mixture total enthalpy, h_t, at each point. h_t is likewise considered constant across the chemistry step. The definition of the static enthalpy is given in this context by Equation 4.1, which is the summation over all species of the heat of formation, h_s^f, and the change in enthalpy relative to standard conditions, Δh_s^{298K}, weighted by the corresponding species mass fraction, Y_s. Values of Δh_s^{298K} are determined using a temperature-based polynomial curve fit of experimental data as shown in Equation 4.2 [40].

$$h = \sum_{s=1}^{n} \left(h_s^f + \Delta h_s^{298K} \right) [Y_s] \qquad (4.1)$$

$$\Delta h_s^{298K} = A_s T + \frac{B_s}{2} T^2 + \frac{C_s}{3} T^3 + \frac{D_s}{4} T^4 - \frac{E_s}{T} + F_s - H_s \qquad (4.2)$$

4. Determine the change in species density due to reaction (i.e. the production source term, $\dot{W}_s$) by solving the reaction rate equations as given by Equation 4.3. Several terms in this equation require definition. First, the molecular weight of species, s, is given by MW_s. Next, $\left(v_s^{\mathcal{P}} - v_s^{\mathcal{R}} \right)_m$ is the change in stoichiometric coefficient for s and reaction, m, as the reactants, $\mathcal{R}$, are converted to products, $\mathcal{P}$. The third-body efficiency for each reaction, which is specific to the kinetics model used, is given by $\mathcal{M}_{eff,m}$. The forward rate constants, k_{f_m}, and the backward rate constants, k_{b_m}, are likewise dependent on the kinetics model and for this research are defined by Equation 4.7 as discussed below. Finally, the species mole fraction is given by X_i.

$$\dot{W}_s = MW_s \sum_{m=1}^{\#Rxn} \left(v_s^{\mathcal{P}} - v_s^{\mathcal{R}} \right)_m \mathcal{M}_{eff,m} \left\{ k_{f_m} \prod_{i=1}^{n} [X_i]^{v_i^{\mathcal{R}}} - k_{b_m} \prod_{i=1}^{n} [X_i]^{v_i^{\mathcal{P}}} \right\} \qquad (4.3)$$

5. Solve the species continuity equation, Equation 2.13, for updated values of each species density, ρ_s.

6. Use the updated values of ρ_s to get the new value for the mixture gas constant and update the mixture's heat of formation.

7. At this point, the change in temperature can be found from conservation of total enthalpy across the chemistry step as reactants, $\mathcal{R}$, are converted to products, $\mathcal{P}$. Using the assumptions from Steps 2 and 3, this conservation equation can be formulated as an implicit function of the temperature, T, as given by Equation 4.4 and solved through the application of a Newton iteration.

$$h_t^{\mathcal{R}} - h_t^{\mathcal{P}} = 0 = h_t^{\mathcal{R}} - \sum_{s=1}^{\mathcal{P}} \left(h_s^f + \Delta h_s^{298K} \right) [Y_s] - \frac{\left| \overrightarrow{V}^{\mathcal{P}} \right|^2}{2} \tag{4.4}$$

where by Equation 4.5:

$$\left| \overrightarrow{V}^{\mathcal{P}} \right|^2 = \frac{(\rho u)^2 + (\rho v)^2 + (\rho w)^2}{\rho^2} = \left[(\rho u)^2 + (\rho v)^2 + (\rho w)^2 \right] \left(\frac{RT}{p} \right)^2 \tag{4.5}$$

8. Once the new value of T is known, a new value for mixture density, ρ is found from the perfect gas equation of state. The mass fluxes are then divided by this ρ to update the velocity components.

9. Finally, the solver returns to step 2 and repeats the algorithm until the solution converges to steady state.

The chemistry model used for H_2–air combustion was put forth by J.S. Evans and C.J. Schexnayder, Jr. [18] and consisted of a finite rate mechanism of seven species (six reacting species and inert N_2) and eight reactions as given by Equation 4.6, where the third body, $\mathcal{M}$, varies as described in the reference.

$$H_2 + \mathcal{M} \longleftrightarrow 2H + \mathcal{M}$$
$$O_2 + \mathcal{M} \longleftrightarrow 2O + \mathcal{M}$$
$$H_2O + \mathcal{M} \longleftrightarrow OH + H + \mathcal{M}$$
$$OH + \mathcal{M} \longleftrightarrow O + H + \mathcal{M}$$
$$H_2O + O \longleftrightarrow OH + OH$$
$$H_2O + H \longleftrightarrow OH + H_2$$
$$O_2 + H \longleftrightarrow OH + O$$
$$H_2 + O \longleftrightarrow OH + H$$

$$\tag{4.6}$$
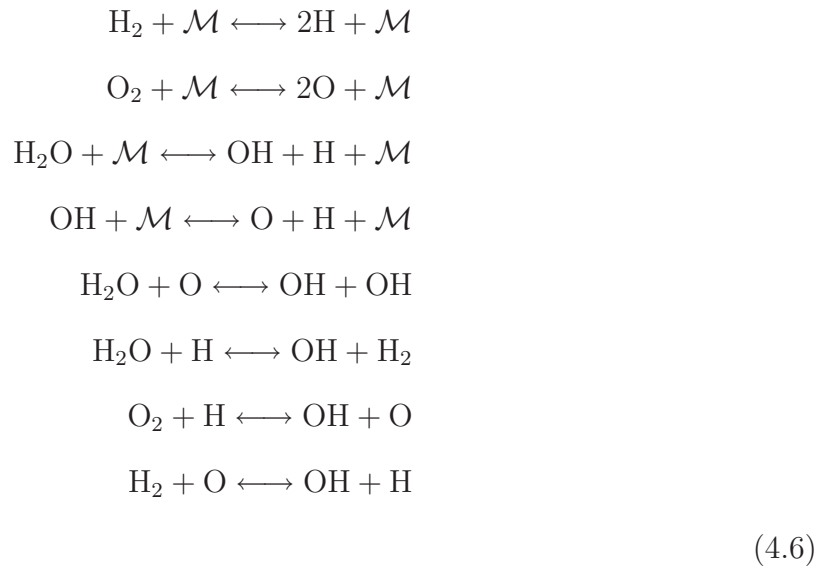
The species forward and backward reaction rate constants were determined for each reaction by an empirically-based Arrhenius rate equation as given by Equation 4.7 for the forward rate constant, k_f, and similarly for the backward rate constant, k_b, where C_{f_m}, η_m and θ_m are all curve fit constants derived from experimental data.

$$k_{f_m}(T) = C_{f_m} T^{\eta_m} e^{-\frac{\theta_m}{T}} \tag{4.7}$$

4.3   Results from a Selected Unit Problem

A hydrogen combustion problem of simplified geometry was selected for testing the thermochemistry addition to the computational code. This case was 1D in nature but was expanded to the 3D computational space for use in the solver. The problem was chosen because it addressed the challenging kinetics problem of ignition in a very lean mixture, and it had been addressed in prior work by Mani, et al, using a similar reaction model [52]. However, it is important to note that in the previously published results the species conservation and flow equations were fully coupled within the solver. The fully coupled approach for chemical kinetics typically increases the computational expense as well as the numerical stiffness of the model.

The problem set-up consisted of $M_0 = 1.82$ flow entering a 0.127m long tube at $T_0 = 1389$K and $P_0 = 1$atm. The flow consisted of a lean, premixed mixture of molecular hydrogen, H_2, and oxygen, O_2, with mole fractions of 0.1 and 0.9, respectively. The flow was assumed inviscid, such that it could be treated as 1D, and thus a square cross-section with sides of 20% of the tunnel length was chosen. The grid dimensions used were 201x5x5 points in the x, y, and z directions, respectively. The boundary conditions were supersonic inflow and outflow, and all solid surfaces were adiabatic, inviscid and non-catalytic (i.e. no species concentration gradients at wall boundary). The convective time scale for the problem, t_{ref}, was given by Equation (4.8), which may be thought of as the time required for a particle to traverse the reference length at the freestream conditions. t_{ref} for this problem was on the order of 97-microseconds (μsec). By way of comparison, Table 4.1 presents selected ignition times as a func-
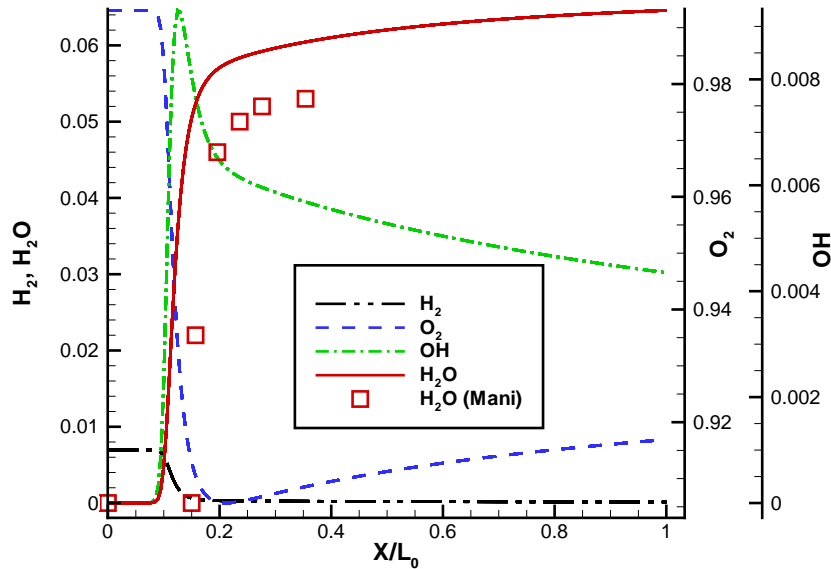
Figure 4.1:   Combustion Nozzle Species Distribution

tion of static pressure and temperature for hydrogen-air combustion [69]. Based upon these values, ignition was predicted to occur at approximately 12% of the domain length for the given thermodynamic conditions.

$$t_{ref} = \frac{L_0}{U_0} \tag{4.8}$$

Table 4.1:   Hydrogen-Air Ignition Times

T (K)	p (atm)	t_{ign} ($10^{-6}sec$)
900	1.0	$> 3E4$
1250	1.0	18
1400	1.0	12
1100	2.0	25

As seen in Figure 4.1, the fuel-air mixture did indeed ignite at approximately $0.12L_0$ as evidenced by the extremely rapid rise in H_2O coinciding with a similar consumption of O_2 and H_2 and spike in the OH, or hydroxyl radical, production. This agrees well with the kinetics model given by Equation 4.6 where it is seen that

Table 4.2:   Comparison of Water Production

Method	Y_{OH}	Y_{H_2O}
Mani, et al	n/a	0.0527
Current Research	0.0043	0.0612
STANJAN	0.0022	0.0609

hydroxyl is required in every reaction directly involving water production. The back of the reaction zone was obtained at approximately $0.2L_0$, resulting in a thickness of about 1cm. This point was recognizable by the sharp decrease in the slopes of both the reactant and product curves towards the post-combustion equilibrium composition. It is worth noting from Figure 4.1 that Mani's results shifted the ignition point downstream roughly 3% with respect to the predicted location.

To provide an independent verification of the kinetics model, the chemical equilibrium solver STANJAN [66] was also used for comparison. STANJAN uses the minimization of the Gibbs free energy in a chemical mixture to determine the equilibrium composition and does not include any effects due to fluid motion. Table 4.2 presents species mass fractions for H_2O and OH for all three models, with the exception of OH, which was not presented in Mani's data. For a better comparison, the finite rate model values are taken at the aft-end of the domain to correspond roughly with the equilibrium composition. As can be seen, the current research model differed by only 0.5% with STANJAN for H_2O, but it was 16% greater than Mani's results. Also, the code failed to match the results for the hydroxyl radical, producing twice as much as the STANJAN results.

A look at how the fluid dynamics impacted the reactions explains the discrepancy seen in the OH production and demonstrated the loosely coupled algorithm accurately captured the relevant combustion physics. Figure 4.2 presents a time history of the flow in the nozzle. Recall the computational domain was initialized uniformly to a lean, but combustible mixture of H_2 and O_2. Therefore, the mixture ignited uniformly throughout the domain downstream of the ignition point as seen in Figure 4.2(a). The induction zone upstream of the ignition point is clearly recognizable

as the region where the temperature remains nearly constant. The hydroxyl radical is gradually increasing during this time, a fact not clearly visible in Figure 4.1 because the relative mass fraction of OH is so low when compared to the reactants. Just prior to the ignition, the temperature drops by a few degrees as the OH radicals spike. This is to be expected as the production of OH is an endothermic reaction. The excess OH is quickly consumed in the exothermic water-production reactions, resulting in a temperature rise of 30K. Although not shown in these curves, the rapid rise in temperature due to combustion occurs in conjunction with a decrease in mixture density. By mass conservation, the flow has to accelerate due to the constant cross-sectional area of the nozzle. This is indeed the case as seen in Figure 4.2(b), with the speed increasing by 110m/s above free stream after 97μsec. Similarly, by momentum conservation, the flow acceleration corresponds to a favorable pressure gradient, pushing the flow along in the axial direction and resulting in a minimum exit pressure of 82kPa. As the initial domain-wide deflagration concludes and is pushed out of the domain by the convecting fluid, the ignition point remains stationary, as it must due to the supersonic inflow.

At this point, the fluid dynamics begins to dominate the physics of the problem. Because the mixture is so lean, barely within flammability limits, there is not much continuous heat release available from combustion. Therefore, what little heat energy that is released is quickly converted into kinetic form. By 194μsec, Figure 4.2(c), the flow is approaching steady state. At this point, the flame location is still clearly recognizable as a slight rise in pressure and drop in speed within the reaction zone. The heat release causes a nearly imperceptible increase in the temperature at the flame front, which is quickly converted into a 12m/s speed increase over the domain and a corresponding pressure decrease of 4kPa. By 310μsec, Figure 4.2(d), the flow has reached a steady state condition. The lack of a significant temperature rise prevents the combustion reaction from reaching completion. This results in excess hydroxyl molecules departing the domain and explains why there is an abundance of OH relative to the STANJAN solution. All these results demonstrate the accuracy of the
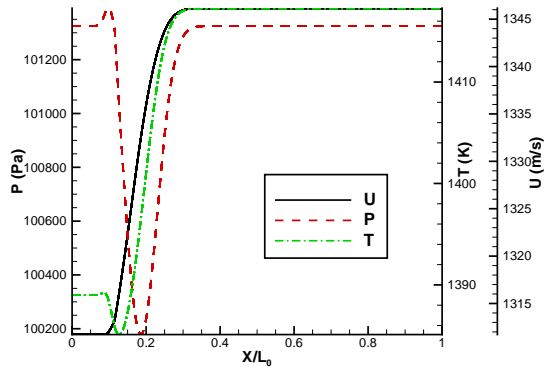
(a) Ignition, 19μsec
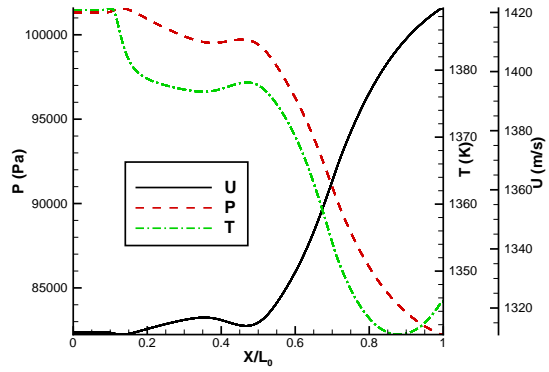
(b) Ignition + 97μsec
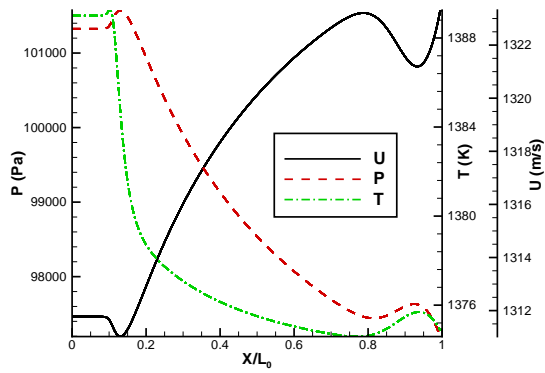
(c) Ignition + 194μsec
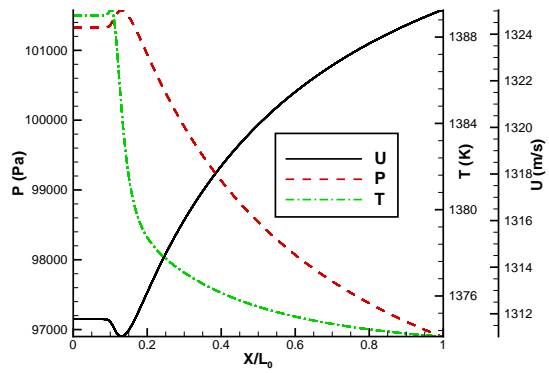
(d) Steady State > 310μsec

Figure 4.2:   Time History of Flow Properties for Combustion Nozzle

loosely-coupled algorithm and the chemical kinetics scheme chosen in the context of supersonic combusting flow. The method was therefore incorporated into the scramjet combustor geometry as discussed in the next section.

4.4   Application to the Scramjet Engine Model

As presented in Chapter III, results from a quasi-1D design tool were scaled to meet the mission requirements of a Mach 10, hydrogen-fueled vehicle with 10,000 mile range. A wide assortment of techniques were implemented to create the final inlet and isolator-combustor geometries presented in Figures 3.8 and 3.9, respectively. In the next subsection, the baseline inlet flowfield without MGD interaction is presented as it is common to all three of the combustors tested in this chapter. This is followed in Subsection 4.4.2 by a comparison of the three combustors. While sharing identical geometries, these combustors differed fundamentally in that they were operated in one of three modes: (1) a "cold" flow simulation, i.e. one without combustion heat release, (2) a volumetric heating rate term using an estimated value of the peak heat release achievable, or (3) the finite rate chemistry algorithm developed in Section 4.2. Based upon these results, the last model of the combustor with chemistry will be shown to most accurately reflect the performance of a real engine.

4.4.1   The Baseline Engine Inlet.   The external-internal compression inlet performed marginally well insofar as it increased the mean static pressure to $57P_0$ at the inlet throat while limiting the static temperature rise to $5.1T_0$ as seen in Figure 4.3. (Recall from Table 3.3, that $P_0 = 684Pa$ and $T_0 = 233K$). However, this result was 23% below the minimum desired combustor inlet pressures of 1/2atm, an outcome directly attributable to the inability of the quasi-1D, inviscid inlet analysis to account for the three-dimensional effects discussed in this subsection. A review of Figure 4.4 reveals that the local cross-sectional average of Mach number decreased fairly uniformly through the inlet from the reference value of $M_0=10$ to an inlet throat value of M=3.81. This value at the throat is still higher than the Mach 1–3 range
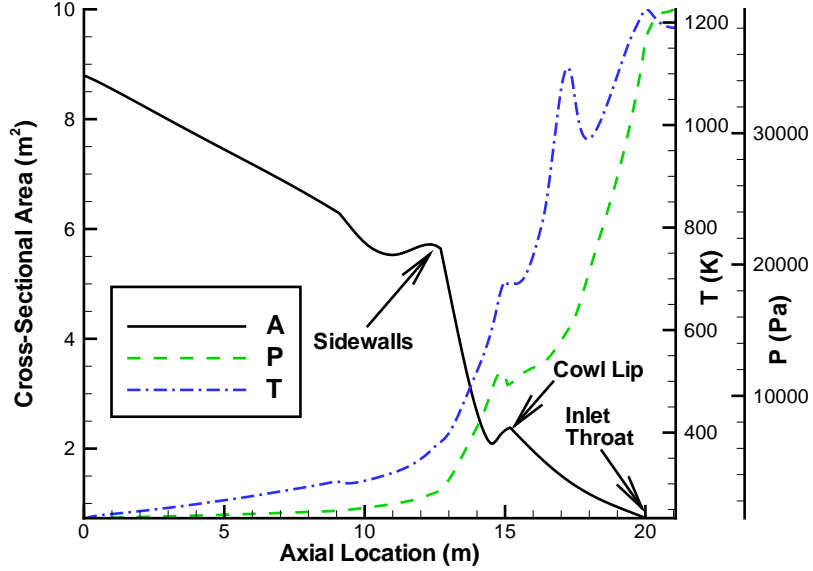
Figure 4.3:   Mean Values of Static Pressure and Temperature within Baseline Inlet

desired for a scramjet combustor, providing an opportunity for improvement through the use of MGD interaction. In addition, Figure 4.4 shows the axial velocity experienced a substantial decrease in the vicinity of a large separation region downstream of the cowl shoulder. This separation region, which also caused the localized temperature spike at x=17.25m in Figure 4.3, is discussed in greater detail below. It also served as the subject of the local flow control efforts presented in Chapter V and was a contributing factor to the baseline heat transfer of 69.6MW out of the inlet walls. Regarding overall inlet performance and efficiency, force balancing using Equations 2.65 – 2.67 revealed a baseline drag of 86kN, lift of -67kN, and yaw of 870N. The negative lift, or down force, was due to a mass flow spillage at the cowl lip which is described in the following paragraph. Because the computational domain did not model the external flow around the cowl, it is not certain how much this down force would contribute to the overall vehicle flow field and force balance. Finally, the system efficiencies were given by: $\pi_c = 0.1519$, $\eta_{KE} = 0.8868$, $\Delta s/C_p = 0.4827$, and $\eta_c = 0.7525$, as defined by Equations 2.70– 2.73, respectively. The last result showed
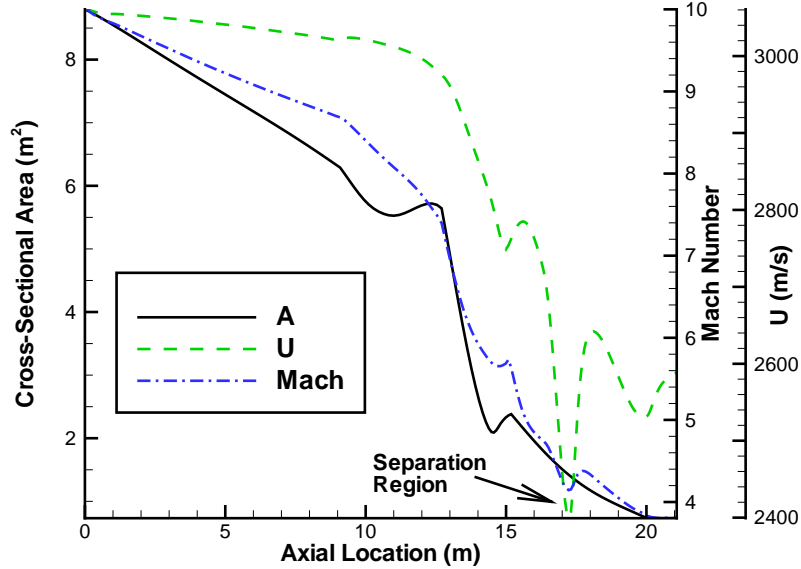
Figure 4.4: Mean Values of Mach Number and Normalized Axial Velocity within Baseline Inlet

the inlet performed somewhat less efficiently than the nominal value of $\eta_c = 0.9$ used by Heiser and Pratt in their analysis [25]; a fact that was attributable to three key inlet flow features.

First and foremost, 59 kg/s, or roughly 22%, of the freestream mass flow was spilled at the bottom cowl lip, never making it into the internal compression portion of the inlet. This spillage loss was a purely 3D effect attributable to the sidewall interaction. The additional sidewall compression caused the flow to seek pressure relief by turning downward, an effect previously documented by Holland [27,28]. This effect was clearly visible in Figure 4.5(a) by the sharp decrease in mass flow rate at the cowl lip and in Figure 4.5(b) by the increase in a negative v-velocity component near the cowl. Normally, this spillage could be countered by moving the cowl lip forward, however, the pressure relief is a desired effect for engine starting which would occur at lower Mach numbers and higher pressures. Therefore, although it was not needed for the cruise test conditions examined in this research, this geometric feature was kept to improve the realism of the overall design.
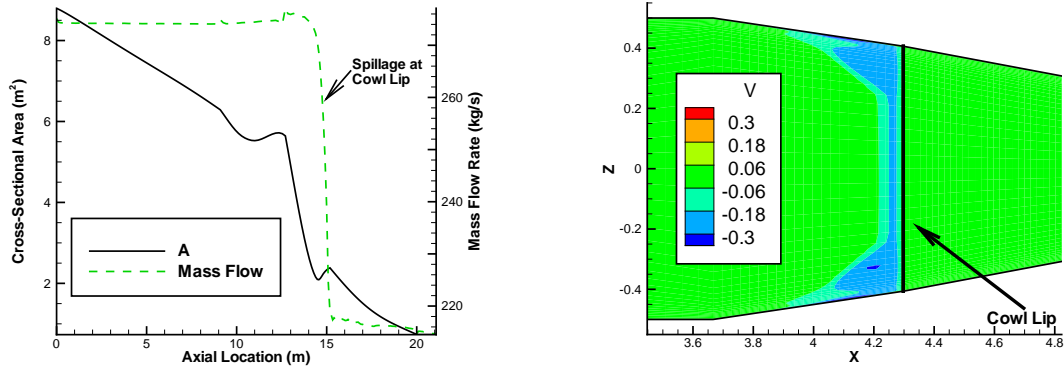
(a) Mass Flow Rate

(b) Normalized v-Velocity Contours Demonstrating Mass Spillage in Cowl Lip Vicinity

Figure 4.5:   Baseline Inlet Mass Flow Emphasizing Cowl Spillage

Second, large areas of expanded flow downstream of the inlet shoulder (opposite of the cowl lip on the body side) and the inlet throat were encountered. These expansions are clearly visible in Figure 4.6(a) as the blue shaded, low pressure regions. Note, the pressure contours in this figure have been normalized by P_0=687Pa. The pitch plane expansion at the cowl shoulder was seen as particularly detrimental to the compression efficiency as a large region of the body-side flow returned to nearly freestream pressure conditions just prior to interacting with the reflected shock off the cowl lip. This interaction created a separation zone as shown in Figure 4.6(b), fairly symmetric about the k-midplane, due to the severe adverse pressure gradient formed where the cowl lip shock reflected off of the body side and was met by the low pressure, high velocity expanded flow around the shoulder. The high pressure tended to locally reverse the flow in the vicinity of the boundary layer and propagate the pressure gradient upstream of the actual shock impingement until equilibrium was reached. This expansion-separation caused an estimated loss of nearly 10kPa in the mean pressure seen at the inlet throat ($x \sim 20$m in Figure 4.3) and a significant amount of heating due to the locally stagnating flow seen in the temperature contours
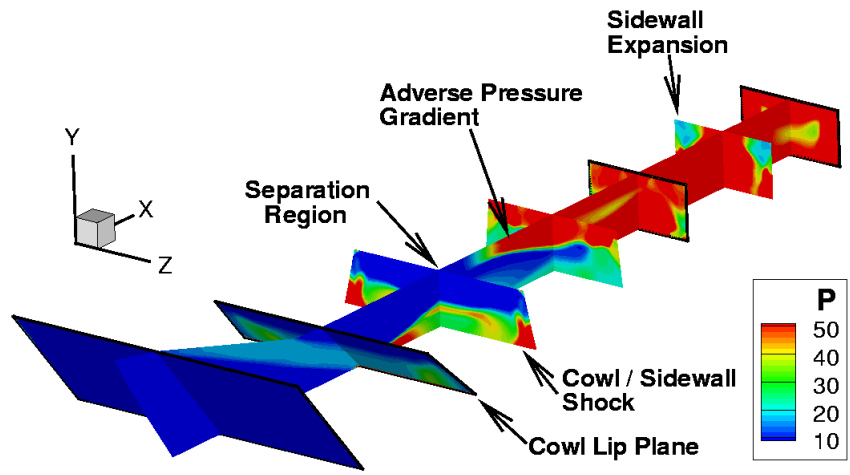
(a) Pressure Contours Normalized by $P_0 = 687$Pa
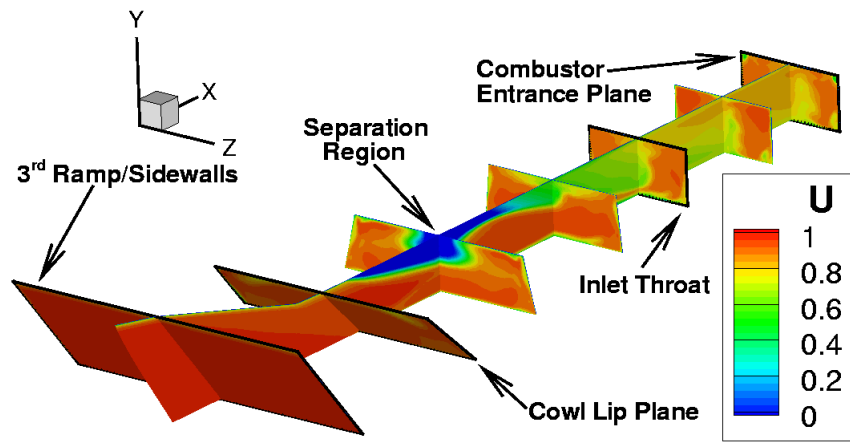
(b) U-Velocity Contours Normalized by $V_0 = 3060$m/s

Figure 4.6:   Baseline Inlet Flow Emphasizing Critical Flow Features

4-14
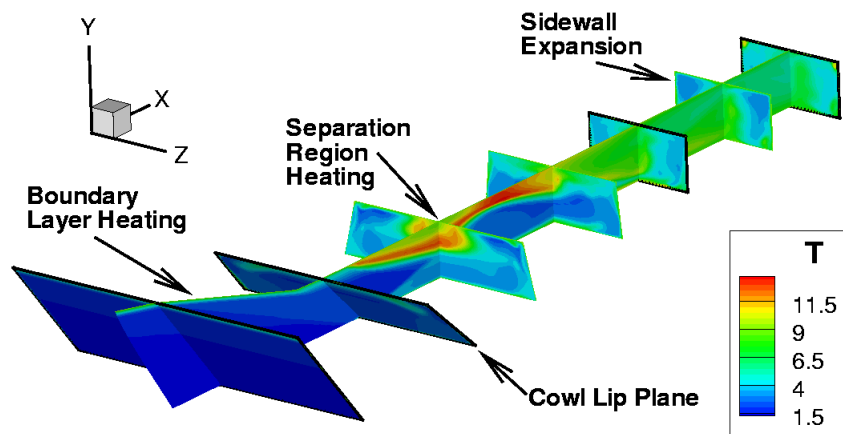
Figure 4.7:   Temperature Contours in Baseline Inlet Normalized by $T_0 = 233K$

of Figure 4.7. A further sidewall expansion into the isolator resulted in an additional 3kPa mean pressure loss.

Finally, vortical structures, similar to the ones reported by Gaitonde [21] as shown in Figure 2.2(a), were observed from just downstream of the third pitch-plane ramp (Figure 4.8(a)) through the rest of the inlet (Figure 4.8(b)). These vortices, were due primarily to the 3D, viscous interaction brought about by the corner flows. This feature was enhanced by the sidewall compression shocks intersecting with those due to the pitch-plane compression. The net effect was an increase in the inlet total pressure loss and entropy rise and a decrease in overall flow momentum and compression efficiency.

4.4.2   A Comparison of Combustion Methods as Applied to the Scramjet Engine.   In order to properly compare the "hot"-fired engine models, it is helpful to first briefly consider the cold-flow engine features in order to recognize how and to what extent the combustor flow is altered by heating/combustion. Reviewing Figure 4.9, it is apparent the flow remained fairly uniform through the combustor until
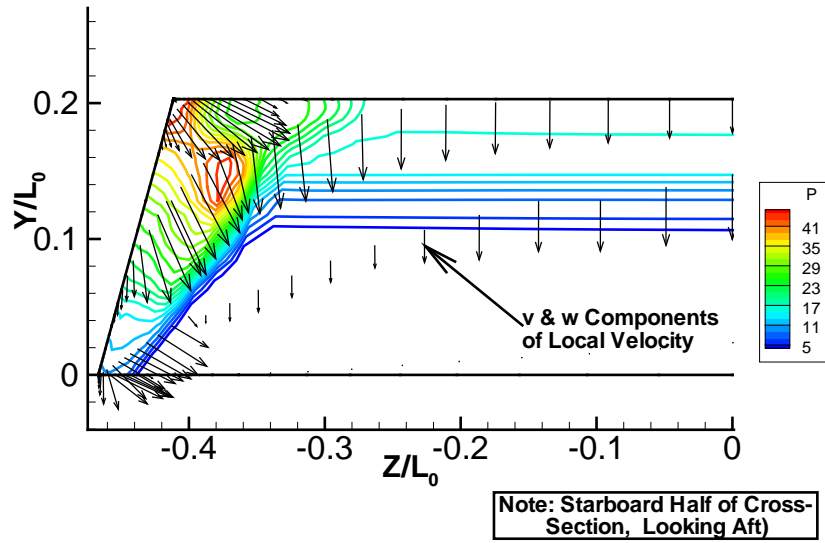
(a) Between 3rd Pitch Ramp and Cowl Plane, x=14.0m
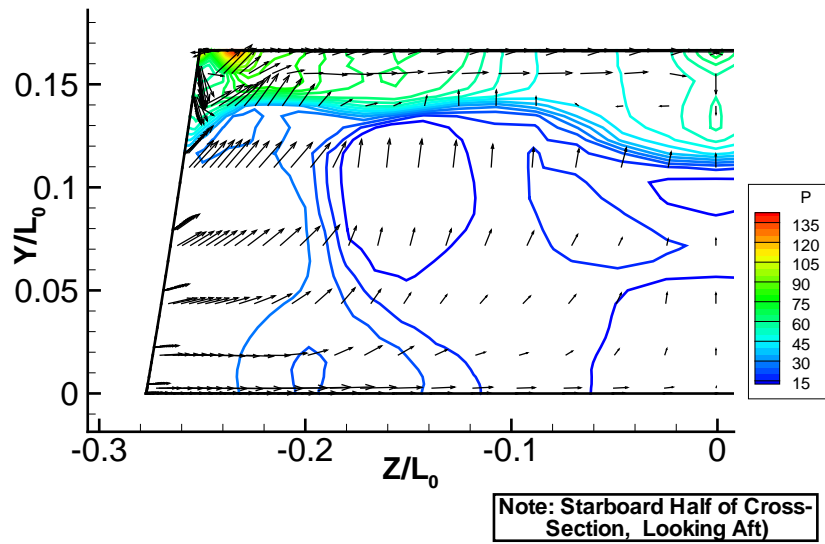
(b) Midway Between Cowl and Throat, x=18.0m

Figure 4.8: Selected Cross-Sections of Baseline Inlet with Pressure Contours Normalized by $P_0 = 684$Pa and Velocity Vectors that Demonstrate Presence of 3D Vortical Flow Structures

reaching the expansion nozzle. The only interesting phenomena observed in the combustor itself was the pressure relief in the upper corners seen within the first 2m (refer to inset of Figure 4.9(a)) and a general dampening of the shock-train-induced pressure variations. This was due to the transition to the slightly expanding geometry intended for maintaining a constant pressure combustion. As an example of the flow uniformity, Mach number contours as seen in Figure 4.9(b) remained fairly constant with changes in the axial direction until reaching the expansion nozzle. Indeed, the cross-sectional averaged Mach number stayed within the high supersonic range across this region increasing from M=3.64 at the inflow plane to M=3.95 at the turn into the expansion nozzle. The slight increase was attributable to the expanding, constant-pressure combustion geometry. At the nozzle exit plane, the average value had increased to M=4.52 with a local peak of M=8.42. Regarding the nozzle expansion, it was clear from the normalized pressure contours of Figure 4.9(a) that the nozzle was significantly overexpanded during cold-flow operation. Nearly the entire upper half of the outflow plane had a ratio of $P/P_0 < 1$ with a planar average of 2.53. This large expansion was verified by the transverse velocity components seen in Figures 4.9(c) and (d) where local outflow values of v and w reached $0.550V_0$ (1683m/s) and $0.254V_0$ (777m/s), respectively. The large transverse velocity components implied a significant portion of the exit plane momentum was not being directed in the axial direction. This was obviously a negative impact to thrust and performance that was expected to only increase with the other two models as additional momentum was imparted by heat release.

As mentioned in Section 4.1, previous combustion modelling efforts were constrained to the use of a volumetric heating rate source term spread over a localized Gaussian distribution, referred to as the Q_C model. Estimating the amount of heating and where to apply it is left to the user's experience and discretion. Therefore, employing the model is almost a matter of trial and error as seen in the results presented here. Implementing the Q_C model with the scramjet consisted of distributing the heat release for the hydrogen-oxygen combustion reaction within the combustor. Since the
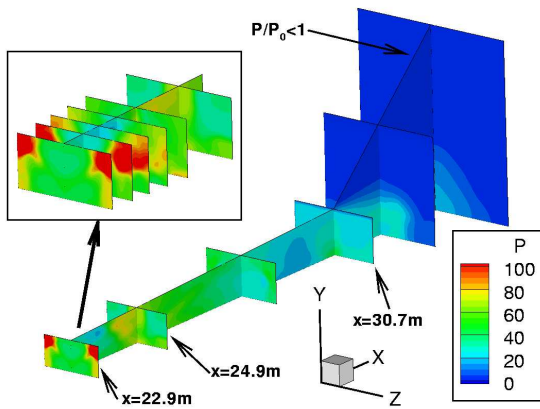
(a) Pressure Contours Normalized by $P_0 =$ 684Pa
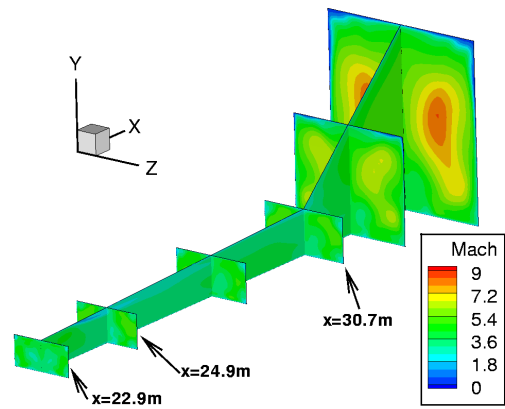
(b) Mach Contours
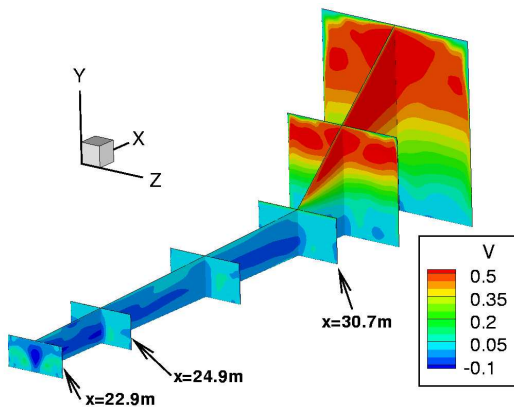
(c) v-Velocity Contours Normalized by $V_0 =$ 3061m/s
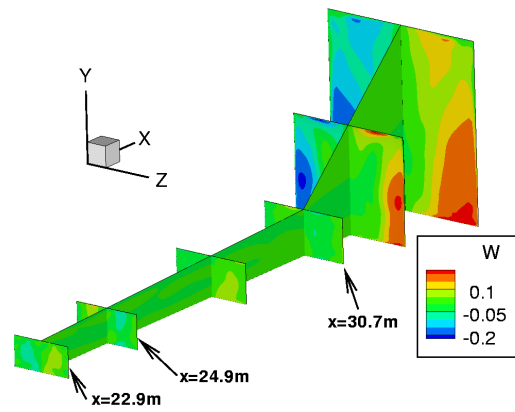
(d) w-Velocity Contours Normalized by $V_0 = 3061$m/s

Figure 4.9:   Normalized Contours of Selected Flow Properties in Cold-Flow Combustor and Expansion Nozzle
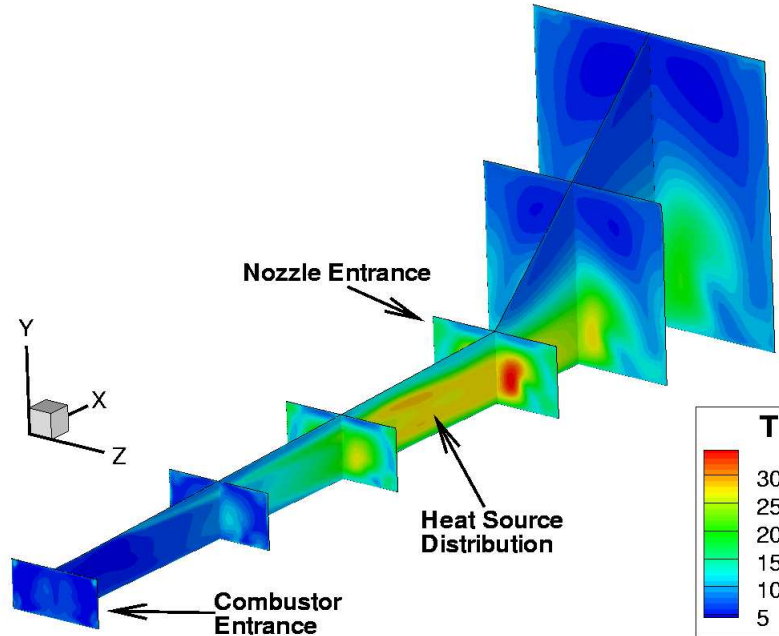
Figure 4.10:   Combustor Temperature Contours, Normalized by $T_0 = 233$K, Using Heating Rate Source Term

fuel-air mixing and induction length could not be determined *a priori*, it was decided to center the peak heating within a cross-section located at approximately 2/3 of the combustor length. Heiser and Pratt's [25] estimate for the total heat imparted by reaction, $\eta_b f h_{pr} \dot{m} = 2.97 \times 10^8$W, was used where $\eta_b = 0.85$ was the assumed combustion efficiency, $f h_{pr} = 3510$kJ/kg is the stoichiometric heating value for the reaction, and $\dot{m}$ was the known mass flow rate entering the combustor. This estimated heating rate was taken as the peak value, which was then distributed throughout the aft end of the combustor as shown by the temperature profile of Figure 4.10.

Using this approach, peak temperatures of up to 30 times freestream or nearly 7000K were obtained. This result was unrealistically high as the adiabatic flame temperature (AFT) for the H_2-O_2 reaction is on the order of 3300K [31]. This extreme heating caused the flow to choke nearly back to the sonic point with Figure 4.11(a) showing local Mach numbers in the core flow dipping to approximately 1.2. This same effect overcame the constant-pressure geometry, elevating peak pressures in the aft end of the combustor to $178P_0$ or 2.9 times the mean value at the combustor inflow

(a) Mach Contours

(b) Pressure Contours Normalized by $P_0 =$ 684Pa
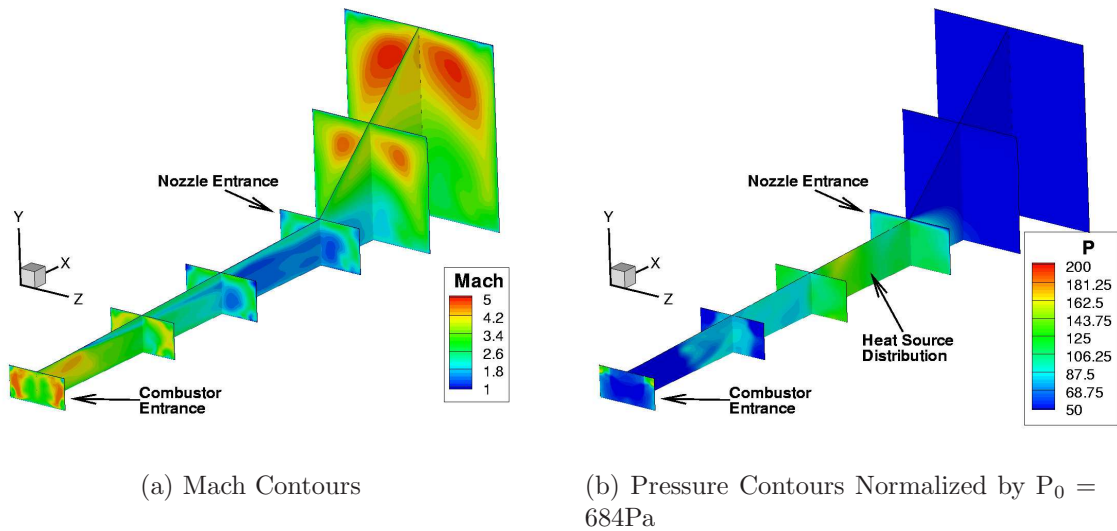
Figure 4.11:   Normalized Contours of Selected Flow Properties in Combustor and Expansion Nozzle Using Distributed Heating Rate Source Term

plane. This outcome reinforced the difficulty of using this approach to achieving accurate thermochemistry results for complex engineering problems such as the scramjet engine. However, the Q_C results were still useful for comparison purposes as the they represented the highest performance the combustor could achieve based solely on geometrical considerations. Of course, the limitations embodied in the actual combustion physics preclude this from occurring.

The finite rate chemistry model was expressly developed to overcome the limited physical basis inherent in the volumetric heat source term, especially as applied to geometries and scales of practical engineering interest. Therefore, it was expected to produce the most realistic result for the scramjet tested, even if it did not produce the best performance. However, the first question to answer was whether or not combustion occurred, and if so, to what extent. Stable, efficient combustion has traditionally been one of the greatest challenges to achieving scramjet propulsion. The scramjet geometry used was predicted to have significant efficiency issues because the structured grid required by the computational model would not easily facilitate the inclusion of a detailed fuel injection and flameholding/mixing system. Recalling from
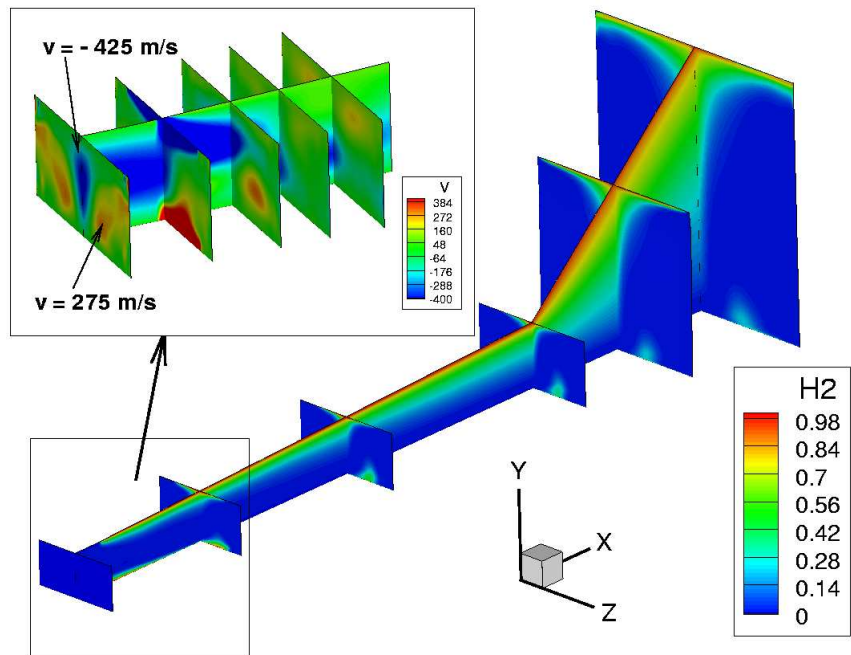
(a) Y_{H_2} with v-Velocity Contours in Inset
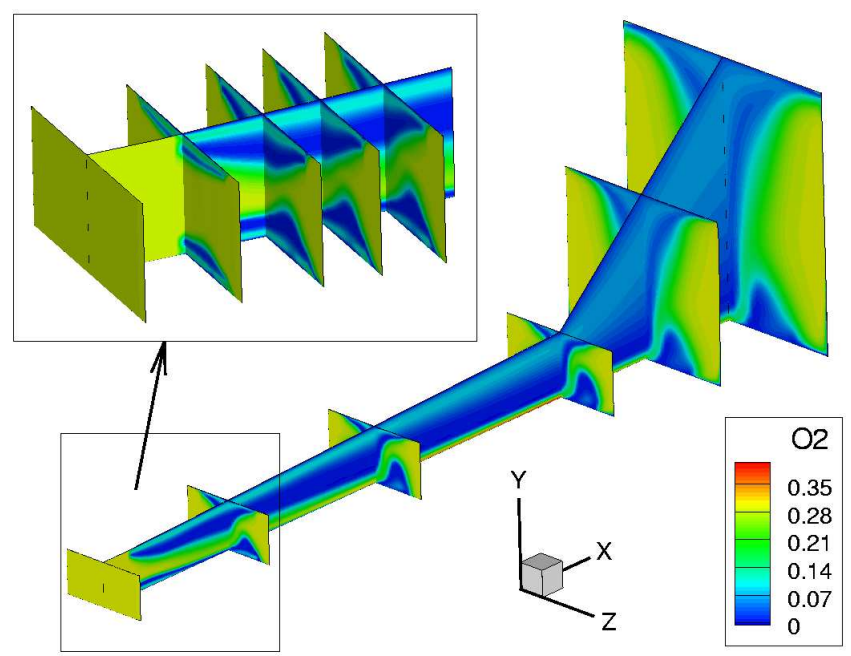
(b) Y_{O_2}

Figure 4.12:   Reactant Species Mass Fractions in Combustor and Expansion Nozzle Using Finite Rate Chemistry Model

Section 3.2 that 1/2 atm is the minimum pressure for efficient H_2–O_2 combustion, additional difficulties were expected because the pressure just upstream of the fuel injectors was only $61.6P_0$ (or 0.42atm). These problems with efficient mixing and reaction were readily apparent from an examination of the flow with respect to the reactant species, H_2–O_2, as seen in Figure 4.12. Looking at the v-velocity contours in the inset of Figure 4.12(a), the flow entering the combustor was highly non-uniform from the 3D shock-train compression through the inlet-isolator. As can be seen the core flow was characterized by significant momentum in the -Y direction. To either side of the core flow were lesser regions of upward flowing momentum, with the overall effect at the fuel injection plane being a 3D, shearing flow with a net downward motion. This downward motion enhanced the H_2 injection from the top of the combustor but suppressed the bottom injector, pushing the inflowing H_2 laterally towards the sidewalls as shown in the main panel of Figure 4.12(a). As Figures 4.12(a) and (b) both show, a majority of the injected H_2 remained trapped against the top of the combustor. At their peak, values of Y_{O_2} of up to 0.11 were found near the upper wall, but this amounted to a fuel-air equivalence ratio of 36, i.e. 36 times richer than the stoichiometric mixture. In effect, this hydrogen fuel was doing little more than providing wall cooling.

Not all of the fuel was wasted, though, as a substantial reaction zone was also present as seen in the reaction-driving OH concentrations of Figure 4.13(a) and the water vapor products of Figure 4.13(b). The sonic fuel injection at high pressure (6.8 times the mean inflow pressure) combined with the shearing core flow easily caused a shock-induced ignition that was especially strong in the vicinity of the bottom injector. This was readily visible by the peak OH contours in the inset of Figure 4.13(a). The reaction zone propagated downstream the entire length of the combustor, sandwiched between the upper and lower fuel jets. While moving downstream, it gradually weakened as the build up of H_2O and depletion of reactants worked to quench the reaction. By the midpoint of the combustor, Y_{OH} values in the reaction zone had fallen to 0.005 or slightly less than half of their peak value in the vicinity of the fuel

injectors. The levels continued to slowly drop, such that by the time the flow entered the expansion nozzle peak values were 0.004. Thereafter, they dropped quickly to below 0.001 as the rapid expansion quenched the combustion reaction and then "froze" the chemical composition. The frozen flow effect was evident for all the species but was particularly noticeable in the similarity of the H_2O nozzle cross sections as seen in Figure 4.13(b). Further evidence of the extent of reaction was found in the thermodynamic properties. For example, a look at the pressure contours of Figure 4.14(a) clearly showed the high pressure region in the fuel injection region. More subtle, but still clearly visible, was the fact that immediately downstream of the fuel injection region the pressure began a continuous decrease. From this, it was evident the reaction as a whole was not progressing very efficiently, as insufficient heat was being released to raise the pressure and balance the geometric expansion as designed. This fact was readily confirmed by the temperature profile of Figure 4.14(b) where even in the heart of the fuel injection region temperatures barely reached 2400K. Recalling the reaction AFT is approximately 3300K, the lack of a suitable mixing/flame holding device was an obvious shortfall in the combustor design, a flaw that was only brought to light by the thermochemistry model. As a final note, a look at the aft end of Figure 4.14 showed that because of the incomplete combustion, the flow was overexpanded in the upper portion of the nozzle, near the top wall. Just as with the cold flow nozzle, this overexpansion caused a significant drop in overall performance.

A quantitative method of evaluating performance, in addition to the qualitative discussion just concluded, was used in order to complete the comparison between the combustion models and the baseline cold flow. This method used the same quasi-1D reduction of the data and control volume formulation described in Chapter II and applied to the baseline inlet of Subsection 4.4.1. This comparison is summarized graphically for the flow properties by Figure 4.15 which is presented here for completeness as it also served as the source for the averaged property data discussed in the previous paragraphs. A closer look at each subfigure clearly shows the influence of the fuel injection and ignition in the chemistry model. Pressure and temperature

(a) Y_{OH}
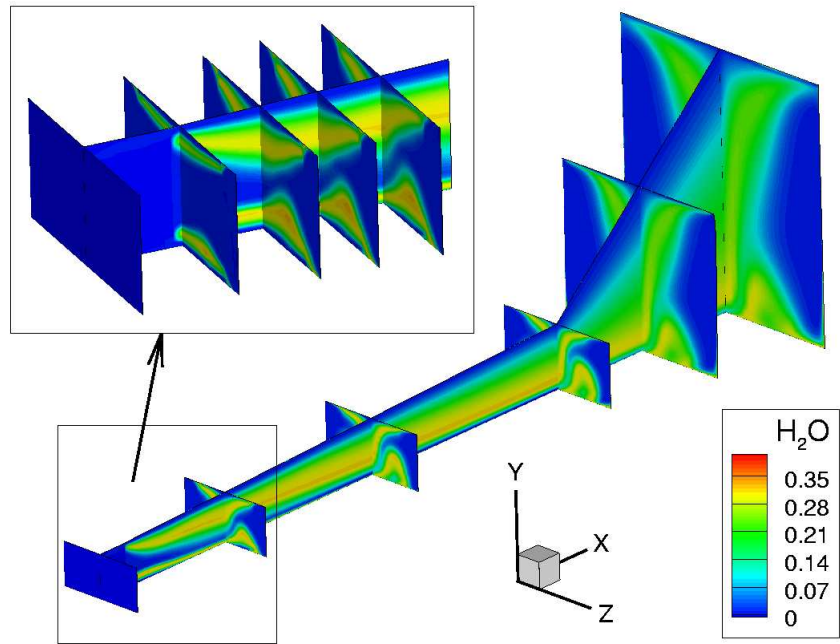
(b) Y_{H_2O}

Figure 4.13:   Product Species Mass Fractions in Combustor and Expansion Nozzle Using Finite Rate Chemistry Model
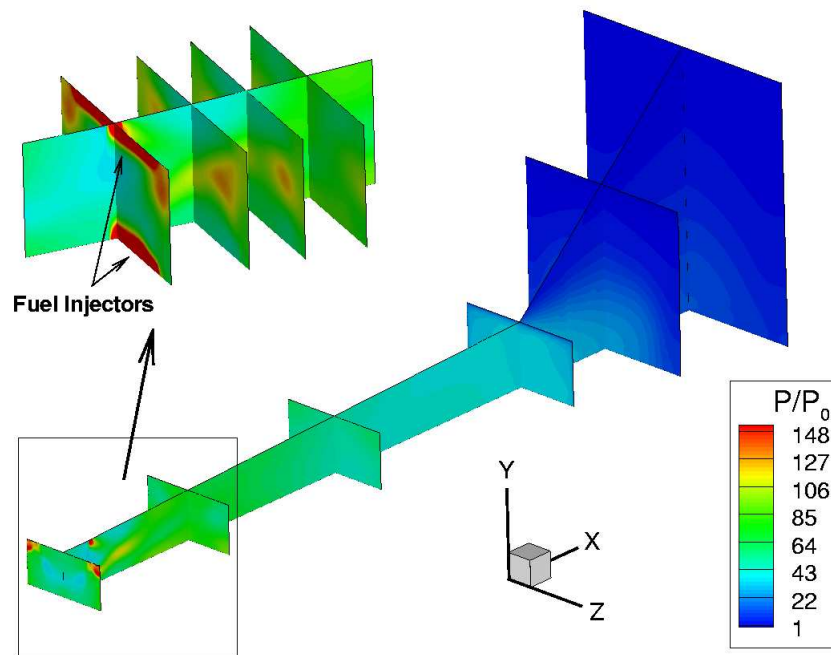
(a) P/P_0
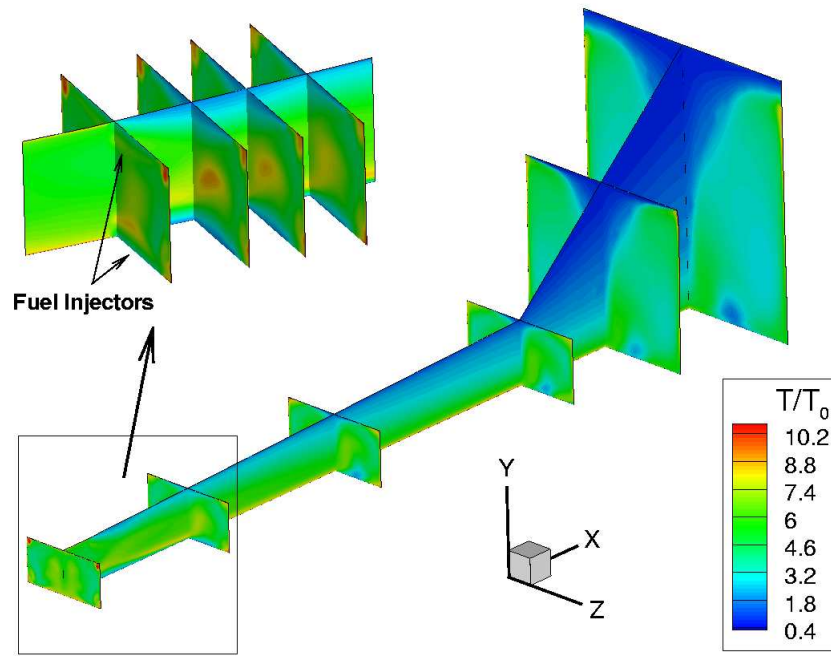
(b) T/T_0
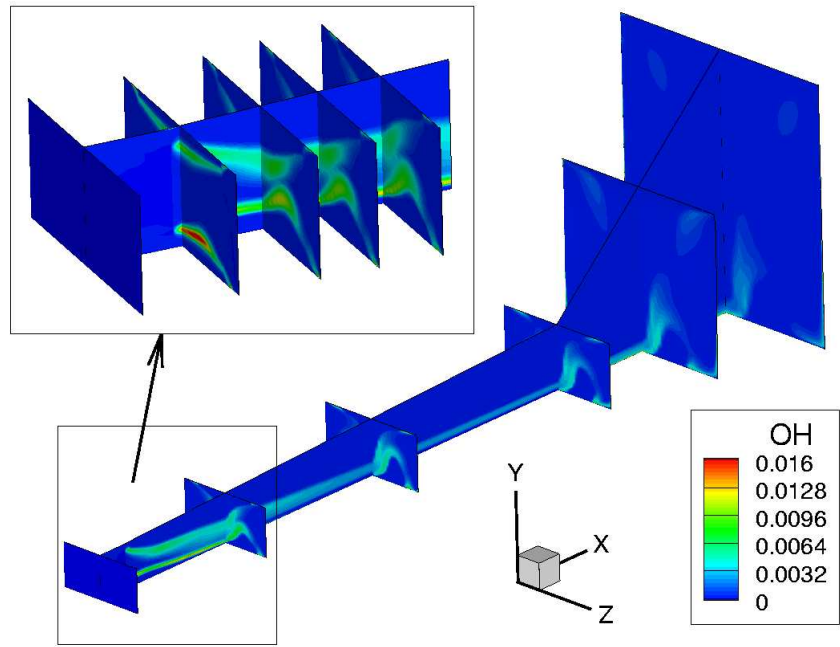
Figure 4.14: Normalized Pressure and Temperature Profiles in Combustor and Expansion Nozzle Using Finite Rate Chemistry Model ($P_0 = 684$Pa, $T_0 = 233$K)

spike at 70% above their inflow values and then monotonically decrease until reaching the expansion nozzle. As would be expected, the Mach number and velocity for all the combustor models followed a trend as the inverse of the pressure and temperature. The impact of the nozzle was likewise evident as pointed out in the figure. Other than the fuel injection spike, what was most striking from these subfigures was just how different the Q_C results were from both of the other models. It was clearly evident that the Q_C method had released an unrealistic amount of heat into the combustor with *average* temperatures and pressures reaching 4865K and 90.2kPa, respectively, in the center of the heat release distribution.

Of course, with all of this energy imparted to the flow, the Q_C model far outperformed the chemistry model with respect to thrust and efficiency as demonstrated in Table 4.3. (Note, the Baseline case in this table refers to the cold flow model and the values include the contributions of the internal inlet and isolator.) Regarding forces, the Q_C model imparted 4.6 times the axial force compared to the chemistry model and 41% more vertical force. Yaw was relatively insignificant for all cases, being two orders of magnitude lower for the heat release models and practically non-existent for the baseline case. While 116.7MW of heat passed out through the walls of the cold flow model due to frictional heating, a net of 112.0MW of heat was added by the thermochemistry model, and an astounding 6 times that amount of combustion heat was added by the Q_C distribution. Because the heat addition process typically improves the total pressure ratio, it was not a surprise that this was the result here. What was unexpected was by how much the Q_C model outperformed the other models. Due to the fact it added energy without any inherent losses, it had a π_c of 2.7 times the chemistry model and nearly 11 times the cold flow model.

4.5 Summary of Results, Conclusions and Recommendations Regarding the Thermochemistry Model

Stable, efficient combustion has traditionally been one of the greatest challenges for achieving scramjet propulsion. To address this challenge, a portion of this
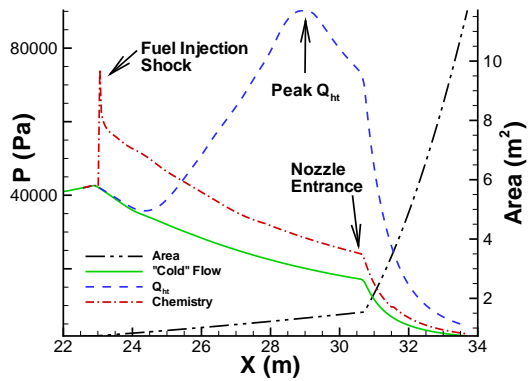
(a) Pressure
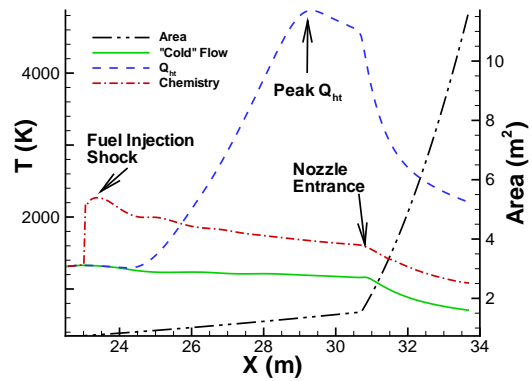
(b) Temperature
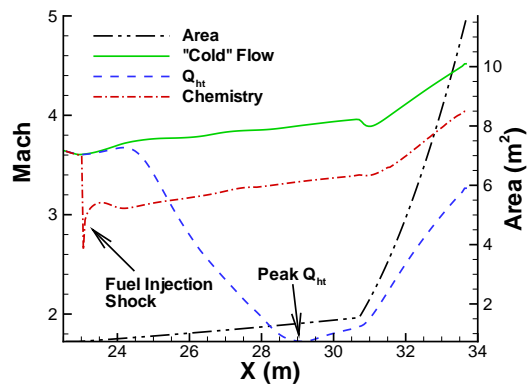
(c) Mach Number
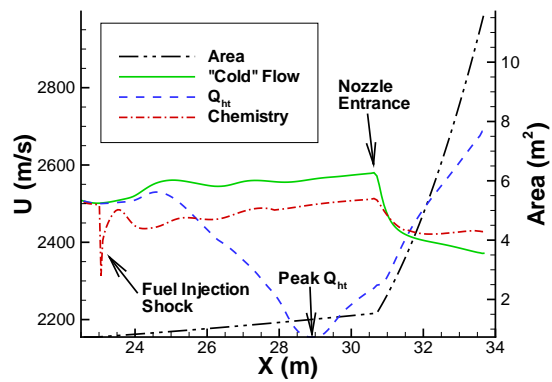
(d) u-Velocity

Figure 4.15:   Comparing Cross-sectional Averages of Dimensional Pressure, Temperature, Mach Number and u-Velocity Profiles in Combustor and Expansion Nozzle

Table 4.3: Scramjet Combustor Performance Comparison without MGD

Property	Units	Baseline	Q_C	Chemistry
Axial Force	kN	-104.9	150.4	32.76
Vertical Force	kN	274.6	305.8	216.5
Yaw Force	N	6.0	1360.0	-344.0
Wall Heat Transfer, $\dot{Q}_w$	MW	-116.7	669.2	112.0
Total Pressure Ratio, π_c	–	0.03	0.32	0.12

research broke new ground in demonstrating the first coupling of a finite rate chemistry and MGD solver for scramjet applications. In addition, the coupling algorithm was implemented in a general way such that it can be used or turned off as needed, allowing computational expense to be balanced against a particular application's requirements. The successful implementation of this computational tool, overcame two significant shortfalls in the AFRL research code: (1) the major assumption the gas was non-reactive air, and (2) chemical combustion could only be represented by a simple volumetric heating rate source term in the energy equation.

As part of the thermochemistry model verification, a 1D, supersonic H_2–O_2 combustion nozzle was modelled. The problem was well-known and had been addressed in prior work, and it provided a challenging test of the algorithm's capabilities since it required solving the challenging kinetics problem of ignition in a very lean mixture. The results exceeded expectations as the model exactly matched the predicted ignition point and only differed by 0.5% with respect to the well-accepted STANJAN software regarding equilibrium water production. The unit problem also demonstrated the advantage of coupling the finite rate chemistry to the fluid dynamics for real world applications. With this problem, it was clearly evident how the supersonic inflow dominated the combustion thermodynamics once the initial deflagration had been pushed out of the domain. In summary, all of these results demonstrated the accuracy of this loosely-coupled algorithm and chemical kinetics model in the context of supersonic combusting flow.

With the successful outcome of the unit problem, the method was incorporated into the scramjet combustor geometry defined in Chapter III. The baseline inlet flowfield without MGD interaction, common to all three of the combustors tested, was characterized first. The inlet performed marginally well insofar as it increased the mean static pressure to $57P_0$ at the inlet throat while limiting the static temperature rise to $5.1T_0$, however, this pressure was still 23% below the minimum desired at the combustor inlet. This shortfall was due to the quasi-1D inlet analysis that failed to account for the adverse 3D effects that led to cowl spillage and regions of expansion and separation. Solving these issues is the focus of Chapter V.

The inlet characterization was followed by a comparison of three combustors models that shared identical geometries but differed fundamentally in that they operated: (1) as a cold flow simulation, (2) with the pre-existing volumetric heat source term, or (3) with the finite rate chemistry algorithm. While for the most part the cold-flow simulation was unremarkable, it did provide the first indication the expansion system had geometric design issues. From the normalized pressure contours of both the cold-flow and chemistry models it was clear the expansion nozzle was significantly overexpanded during these modes of operation with nearly the entire upper half of the outflow plane having a ratio of $P/P_0 < 1$. Additionally, the large transverse velocity components implied a significant portion of the exit plane momentum was not directed in the axial direction, causing a negative impact on thrust and performance. Because engine-airframe integration was not part of this research, incorporating a higher fidelity expansion system geometry was left as a suggestion for future research.

With respect to the two heat addition models tested, the Q_C model reached peak temperatures of up to 30 times freestream (nearly 7000K), or twice the theoretical limit. This resulted in the flow being choked nearly back to the sonic point with peak pressures in the aft end of the combustor 2.9 times greater than the mean value at the inflow plane. While this method did produce the most thrust for the geometry used, the unrealistic outcome actually reinforced the difficulty of using this approach

to achieving accurate results for complex engineering problems such as the scramjet engine.

Among other things, the thermochemistry model corroborated pre-existing concerns that the geometry used would have significant efficiency issues due to the fact the structured grid solver precluded the inclusion of a detailed fuel injection and flameholding/mixing system. Throughout the combustor, much of the injected H_2 remained trapped against the top wall, an effect only observable with the use of the chemistry modelling tool. In effect, this hydrogen fuel was doing little more than providing wall cooling. In spite of this, a substantial reaction zone was also present as seen in the wide-ranging extent of the water vapor product of combustion. A shock-induced ignition in the vicinity of the fuel injectors was especially strong near the bottom injector. The reaction zone propagated downstream the entire length of the combustor, sandwiched between the upper and lower fuel jets. The zone gradually weakened as the build up of H_2O and depletion of reactants worked to quench the reaction. Immediately downstream of the fuel injection region the pressure began a continuous decrease, additional evidence to support the conclusion the reaction as a whole was not progressing very efficiently. This was attributed to insufficient heat release (peak temperatures in the reaction zone were barely 2400K) to raise the pressure and balance the geometric expansion as designed. Beyond any doubt, the lack of a suitable mixing/flame holding device was an obvious shortfall in the combustor design, again an issue only brought to light by the thermochemistry model.

The overall results can be summed up in a few conclusions and recommendations for future research efforts. First, the loosely coupled approach to incorporate finite rate chemistry was very successful with respect to modelling supersonic combustion flow problems and is recommended over the code's pre-existing approaches for these problems. A recommendation for furthering the thermochemistry model would be to add a species diffusion term, primarily to extend applicability to the subsonic regime. In addition, higher fidelity models of viscosity and thermal conductivity exist for multi-species flows that could be used in place of the single-equation Sutherland

model described in Chapter II. With regard to the actual scramjet design tested here, the combustor with chemistry was conclusively shown to accurately reflect the performance of a real engine. One caveat was that several problems with the geometry were identified that could be traced back to the initial quasi-1D design iteration. Because it was outside the scope and timeline of this research to undertake multiple design iterations, it is recommended that future work use the current geometry as a baseline upon which to make improvements. Finally, in a related specific conclusion, under-compression and flow separation in the inlet was recognized as a good location to test localized MGD flow control techniques.

V. Localized Electromagnetic Flow Control

5.1   *A Review of Previously Published Selected Concepts and Applications*

In recent years, numerous methods of using EM fields to locally improve scramjet flow have been proposed. Additionally, a few more ambitious proposals have been made to use these same concepts to both provide electrical energy to power the flow ionizer and augment the vehicle's thrust. Because scramjet vehicles are geometrically optimized for a single design point, it is assumed a significant portion of their mission will be spent operating at off design conditions. In addition, even while operating at on-design conditions there will be regions of locally ill-conditioned flow due to geometric or other constraints. Therefore, localized flow control aims to mitigate these ill-conditioned regions or enhance favorable flow qualities. These flow control techniques may be the deciding factor in success or failure for a particular engine design.

Two localized approaches featured prominently in the literature: maintaining the shock-on-cowl-lip condition and boundary layer transition and control. The former of these is a design imperative as it is the most effective way of maintaining the proper mass flow of air into the engine. Macheret and associates at Princeton University have completed a great deal of analytical and some numerical work on this application. One idea they have explored is to operate a near-surface MGD system just upstream of the cowl that would use electron beams to ionize the flow [47]. The Lorentz force would then be used to increase or decrease the flow momentum at the cowl to maintain the shock-on-cowl-lip at off-design Mach numbers. Although their model was limited to 2D, inviscid flow, they were able to maintain the desired flowfield at Mach numbers of 2 less than the design point of 8. However, the penalty for using MGD was an increase in total pressure loss which could be considered as a drag penalty. The investigation of this drag penalty was left as future work. A second method Macheret, et al, have investigated is to achieve the same effects by creating a *virtual cowl* of heated air in front of the cowl lip [49, 50, 73]. Although the heating mechanism is unspecified, the

authors point out that it is possible that RF or microwave energy could be supplied to an area pre-ionized by an electron beam or laser. If this is the case, then at best MGD effects could prove both a satisfactory heating mechanism and a source of additional electrical power. Even if the Joule heating from MGD interaction is not adequate for this application, it could still serve as the electrical power supply for whatever heating system is chosen.

Manipulating the boundary layer is another local flow control application that preliminary studies have demonstrated may benefit from MGD application. This is especially true with respect to controlling the transition from laminar to turbulent flow as well as increasing the near wall flow momentum to prevent separation and potential inlet unstart. The shock structure within 3D inlet flows is incredibly complex as several researchers [21, 28, 37, 39] as well as this research have shown. Sidewall interaction, low momentum vortical structures and large areas of flow separation are common detrimental features. These structures are detrimental to the flow as they increase total pressure losses, prevent a smooth flowfield at the combustor entrance, and in the worst instances may cause inlet unstart. The next section identifies how the application of MGD to a scramjet inlet can improve the inlet efficiency as measured by the efficiency metrics discussed in Chapter II as well as increase the pressure entering the combustor, a critical requirement for efficient combustor operation.

5.2 *Improving Engine Performance by Application of Localized Inlet Flow Control*

Prior to this effort, only simulations without the application of EM fields had been conducted on the flight-scale geometry. As illustrated in Subsection 4.4.1, sidewall and corner flow-induced vortical structures throughout the internal diffuser were observed. Large areas of expanded flow downstream of the inlet shoulder (opposite of the cowl lip on the body side) led to a sizeable separation zone, and the expansion fans at the inlet throat further decreased the average pressure entering the combustor. The question then arose as to whether MGD could be applied in this situation

to mitigate or prevent the formation of this separation zone, improving the overall inlet flow field and specifically the flow entering the combustor. Two concepts were considered. The first concept was the use of an MGD generator to increase pressure, especially in the cowl shoulder region, to better match that of the reflected shock. Alternatively, an MGD accelerator was considered in order to increase flow momentum in the portions of the inlet subject to locally expanding flow. This was hypothesized to be especially helpful when focused on the low momentum boundary layer where the adverse pressure gradient initiated flow separation.

Thirty-two different cases of localized EM fields and corresponding regions of specified conductivity were applied immediately downstream of the cowl shoulder on the body side in an effort to mitigate this performance loss. In all cases, the $\vec{B}$ field was uniform and aligned in the +Y direction, and the $\vec{E}$ field was likewise uniform but aligned in the -Z direction. Four different distributions for σ were explored; the two primary cases, referred to as Case 1 and Case 2, respectively, appear as the contoured regions in Figures 5.1(a) and 5.1(b) . As can be seen, these two cases differed only in the axial extent of the plasma volume. For both of these cases, an additional subcase was also explored wherein the conductivity was centered just outside the boundary layer as in Figure 5.1(c). This subcase simulated an electron beam with the maximum conductivity centered several centimeters from the wall. The conduction current density, $\vec{j}$, was given by Ohm's Law in Equation 2.26 and was therefore in the $\pm Z$ direction depending on the magnitude of the non-dimensional load factor, k, which was tested at values of 0.0, 0.7, 1.0, and 1.3. The Lorentz force as given by $\vec{j} \times \vec{B}$ was then in the -X direction (or decelerating the flow) for $k < 1$ and in the +X direction (accelerating) for $k > 1$. Finally, interaction parameters of $Q = 1$ and 5 were examined at the prescribed freestream flight conditions in order to gauge the effect of increasing $\vec{B}$.

    5.2.1 Synopsis of Baseline Case.   The baseline case referred to here is the converged scramjet inlet flowfield prior to the application of the EM fields described
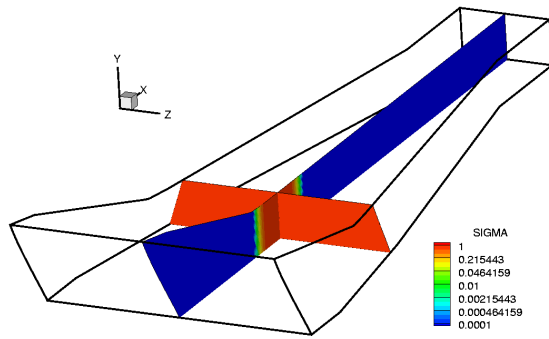
(a) Case 1
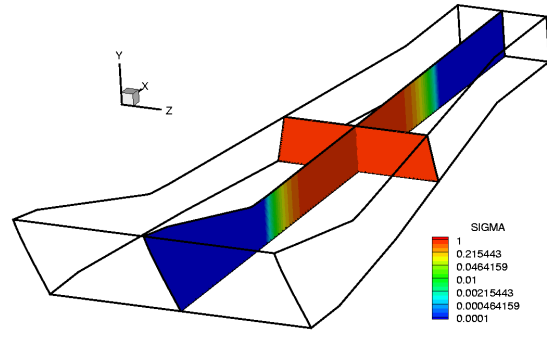
(b) Case 2
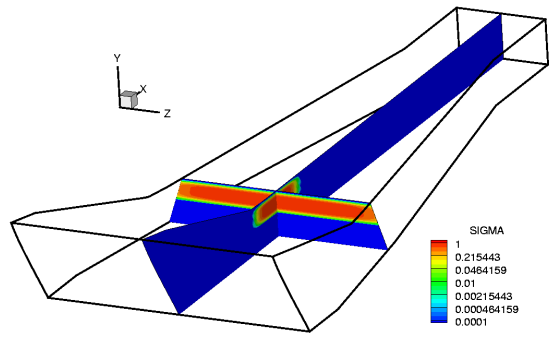
(c) Case 1B

Figure 5.1:   Full Cross-section Non-Dimensional Conductivity (SIGMA) Profiles in Inlet
(a) Case 1: Conductive region is limited to upstream of separation region.
(b) Case 2: Conductive region extends from cowl lip to inlet throat.
(c) Case 1B: Conductive region centered outside of boundary layer.

in detail in Subsection 4.4.1. For reference, Table 5.1 represents pertinent details on this flow including averaged flow properties at the exit plane, the drag force, and the efficiency metrics defined in Section 2.6.

Table 5.1:   Pertinent Baseline Scramjet Inlet Results

Property	Units	Value
Mach	–	3.7664
γ	–	1.3624
Temperature	K	1218.5
Pressure	kPa	40.303
U-velocity	m/s	2566.9
Drag	kN	86.254
Wall Heat Transfer, $\dot{Q}_{ht}$	MW	-69.553
Total Pressure Ratio, π_c	–	0.1519
KE Efficiency, η_{KE}	–	0.8868
Non-dim. Entropy Rise, $\Delta s/C_p$	–	0.4827
Adiabatic Compression Eff., η_C	–	0.7525

5.2.2 Results from Conductivity Case 1.   The addition of EM fields had limited effect on the outflow properties, with the exception of the $k = 0$ parameter cases, which experienced extreme dissipative heating. This heating resulted in average temperatures 24% and 77% above baseline for $Q = 1$ and $Q = 5$, respectively. This was due to the fact that, with no external load applied, all of the extracted electrical energy had to be dissipated within the flow itself. The accelerator case, $k = 1.3, Q = 5$, also experienced additional heating, but to a lesser extent, due to the deposition of additional external energy. For this case, the $Q = 5$ interaction elevated the temperature 18% above baseline. For the remaining parameters, Mach number, γ, and temperature were virtually unchanged from the baseline case. The pressure showed the same trends as temperature but to a lesser degree. For $k = 0$, pressures increased above baseline by 12% and 54%, and for $k = 1.3$ with $Q = 5$, the pressure increase was 16%. As Figure 5.2 showed, only the $k = 0.0, Q = 5$ case experienced substantial gains in pressure upstream of the inlet throat, due to the EM interaction upstream of the separation region. The expansion at the inlet throat, however, was seen to
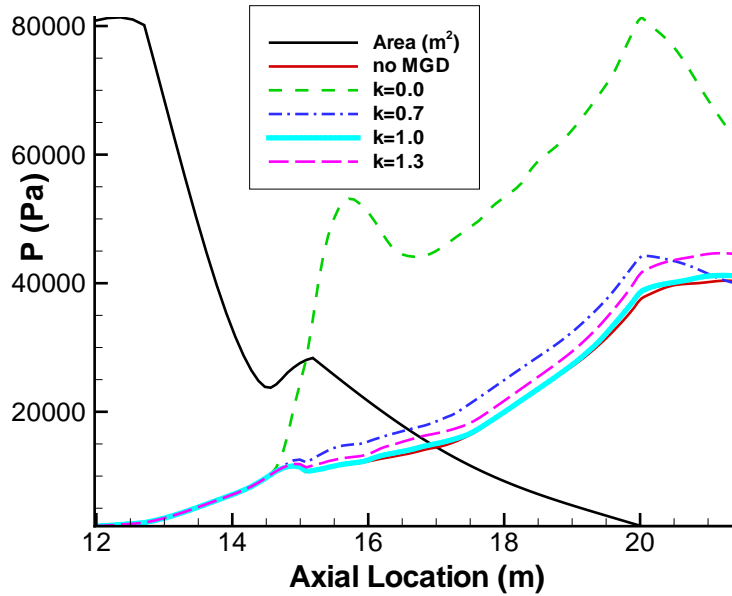
Figure 5.2:   Mean Inlet Pressure for Case 1 with Varying k and $Q = 5$

have a dominating influence on the flow, drastically reducing any potential pressure increases.

With the exception of $k = 0$ and $k = 1.3$ with $Q = 5$, the efficiencies for Cases 1 and 1B were only marginally impacted as seen in Figure 5.3. (Note: in these comparison bar charts to follow, the numbers 1, 1B, etc. refer to the conductivity profile, while "kX.X" refers to the load factor and Q the interaction parameter used.) The greatest impact on efficiency was $k = 0$ with $Q = 5$, where π_c was reduced to 3% of the freestream value and η_C decreased by 6.7% with respect to baseline. Changes in $\Delta s / C_p$ and η_{KE} were similarly affected with an increase of 49% and decrease of 4%, respectively, for this case. In an interesting result, it was noted that the largest increase in η_{KE}, 8% above baseline, occurred for $k = 1.3, Q = 5$. This makes sense from the perspective that energy external to the inlet was being added in a manner that was increasing the kinetic energy and thus momentum in the inlet, as desired.

Following the same trend discussed above, the parameter $k = 0, Q = 5$ was seen in Figure 5.4 to have the greatest drag at 158% greater than baseline, corresponding
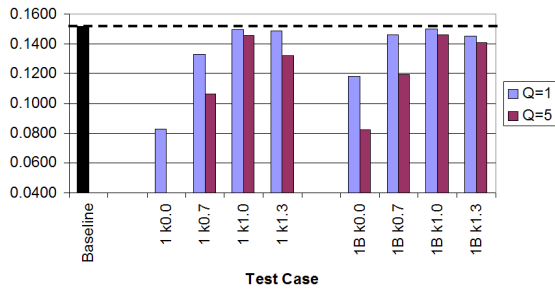
(a) Total Pressure Ratio
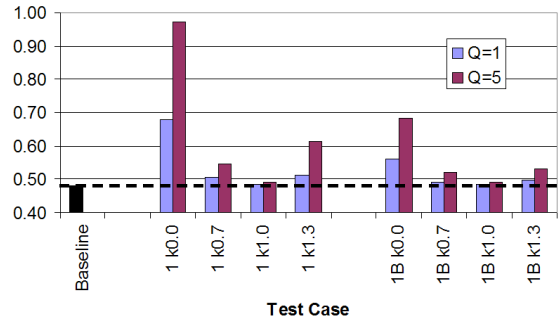
(b) Dimensionless Entropy Rise
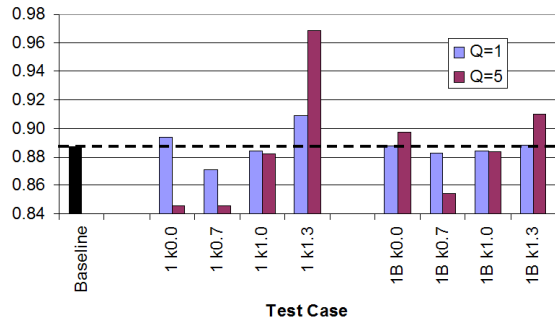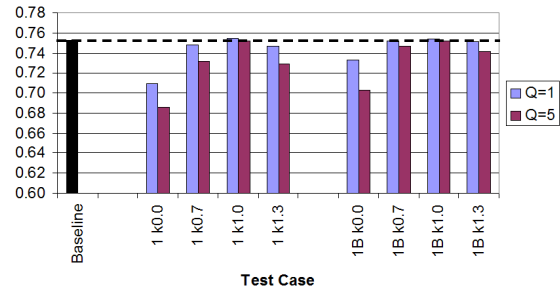
(c) KE Efficiency

(d) Adiabatic Compression Efficiency

Figure 5.3:   Inlet Efficiency Metrics for Cases 1 and 1B
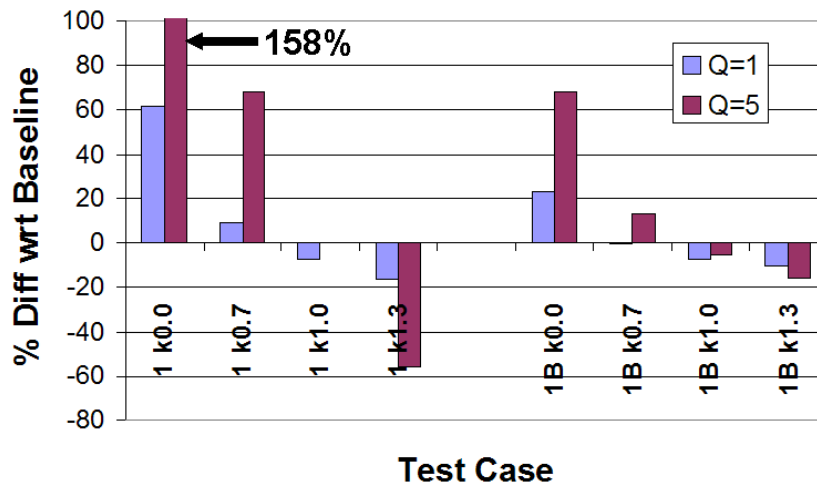
Figure 5.4:   Comparison of Net Inlet Drag for Conductivity Case 1

(a) Case 1 Inlet with k=0, Q=5

(b) Inlet without MGD Flow Control
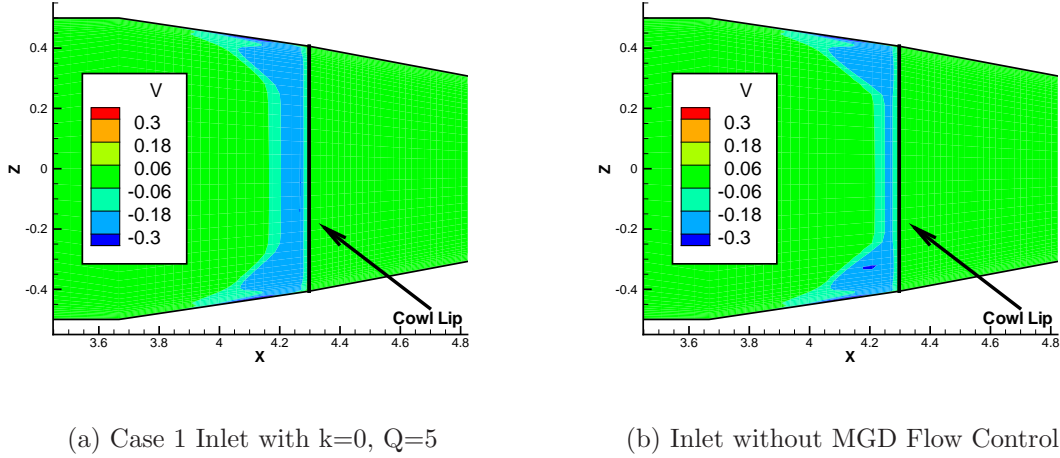
Figure 5.5:   v/V$_0$ Contours Demonstrating Mass Spillage in Cowl Lip Vicinity

to the highest Lorentz Force at -111.0kN. For constant k, higher Q meant higher Lorentz force as expected. Also, as one would expect, increasing the departure from $k = 1$ increased the Lorentz force. This was readily apparent in the overall axial force imposed on the inlet. At $k = 1$, the interaction was minimal and the net drag was actually reduced 7% below baseline. The biggest decrease in drag occurred, as expected, for $k = 1.3$, where the positive Lorentz force for $Q = 1$ was 10kN and for $Q = 5$ was a 42kN. This resulted in drag reductions of 16% and 56%, respectively, with respect to baseline. In an unexpected result, it was observed that as k went to zero there was a significant increase in mass flow spillage out of the inlet at the cowl lip. This was unique to Case 1 and was due to the full cross-section conductivity profile that extended upstream of the cowl lip plane. In effect, the Lorentz force was acting to bypass up to an additional 18kg/s of air around the cowl. This additional bypassed mass flow slightly mitigated the Lorentz force-induced drag increase. In effect, it was acting as a thrust, just as it would in a bypass turbofan engine. This additional spillage was easily visualized by comparing the increased thickness of the spillage contours for the $k = 0, Q = 5$ parameters as seen in Figure 5.5(a) to those of the inlet without MGD as seen in Figure 5.5(b).
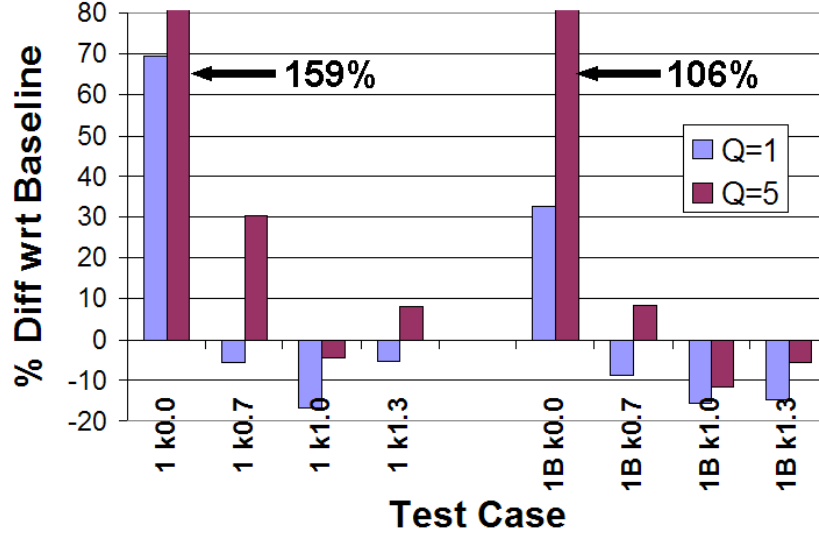
Figure 5.6: Comparison of Normalized Heat Transfer for Conductivity Cases 1 and 1B

As discussed previously in Section 2.6, the time rate of energy change in the control volume, dE/dt, is equal to the heat transfer rate in through the CV, $\dot{Q}_{ht}$, plus the EM energy interaction, $\dot{W}_{EM} = \vec{E} \cdot \vec{j}$. All of the EM cases deposit some energy into the flow through dissipation, with the amount increasing as k departs from a value of 1. Interestingly, while all cases had a net heat transfer out of the CV, some of the MGD cases exhibited less overall heat transfer than the baseline case. With the exception of $k = 0$, all of the $Q = 1$ cases had 5%–17% less as seen in Figure 5.6. These decreases were attributable to the fact that the stagnation region due to separated flow was being moved slightly farther away from the wall, while at the same time the low interaction of $Q = 1$ was contributing only 25%–30% of its $Q = 5$ amount. A close-up examination of the separation region revealed this unexpected result; a result that would later take on even more significance in the plasmas limited to the near wall region. From Figures 5.7(a) and (b) it was evident the EM cases caused the separation region to actually grow compared to the baseline case. However, this same effect caused the stagnant flow to also move away from the wall, creating a buffer zone of relatively lower temperatures next to the wall as seen

in Figures 5.7(c) and (d). It was this change in the heat distribution that caused an additional small decrease in wall heat transfer.

Conversely, the maximum value of 180MW (or 159% above baseline) occurred for $k = 0, Q = 5$. $k = 0.7$ and 1.3 cases put roughly the same amount of dissipation into the flow on the order of 9 and 34MW for $Q = 1$ and 5, respectively. However, whereas dissipation made up roughly 40% of the total $\dot{W}_{EM}$ for $k = 0.7$, it comprised only 27% of the total for $k = 1.3$. Therefore, as an overall measure, the generator case at $Q = 5$ reflected an overall greater heat transfer rate through the CV boundaries. The $k = 1$ cases put the least amount of dissipation into the system (on the order of 1.2MW–3.6MW) because $k = 1$ represents the open circuit case where the conduction current is approximately zero. Joulean dissipation varies directly with the current, thus the lower the current (i.e. k closer to 1) the less the flow is heated.

Regarding the ionization model, the conductivity region filled approximately 3.0m³ with values of σ ranging between 0.63 and 0.86 mho/m. B-fields were on the order of 3.3T for $Q = 1$ and 7-8T for $Q = 5$. Net power generation was simply the difference between the generated electric power, P_{gen}, and the ionization power, P_{ion}, as defined in Section 2.7. Referring to Figure 5.8, only the $k = 0.7$ cases demonstrated a meaningful net power generation with 18MW for $Q = 1$ and 82MW for $Q = 5$. The required power for ionization, P_{ion}, was on the order of 1.3 - 1.5MW for all cases. The enthalpy extraction ratio, η_g, which was defined in Section 2.6, was typically in the range of 10% - 20% but was a max of 31% for the $k = 0.0, Q = 5$ generator as shown in Figure 5.9. The $k = 1.3, Q = 5$ accelerator actually increased the enthalpy by 1%. Recall from Section 2.6, however, that this measure includes changes due to both EM-interaction as well as geometric compression.
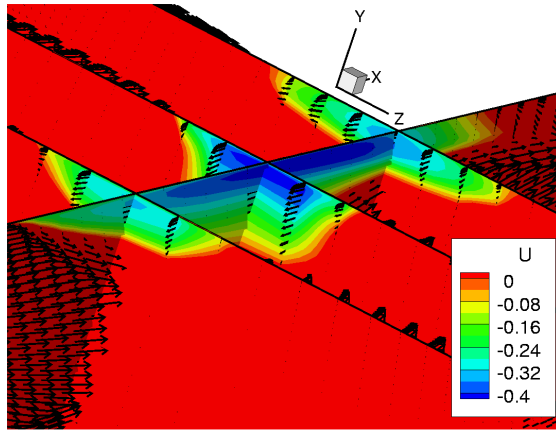
(a) Baseline u/V_0 Contours
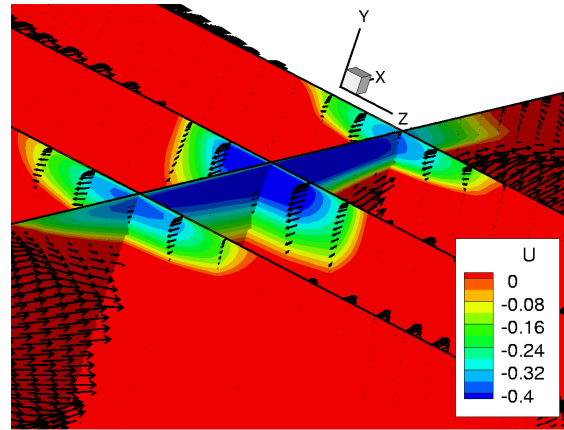
(b) Case1, k=0.7, Q=1 u/V_0 Contours
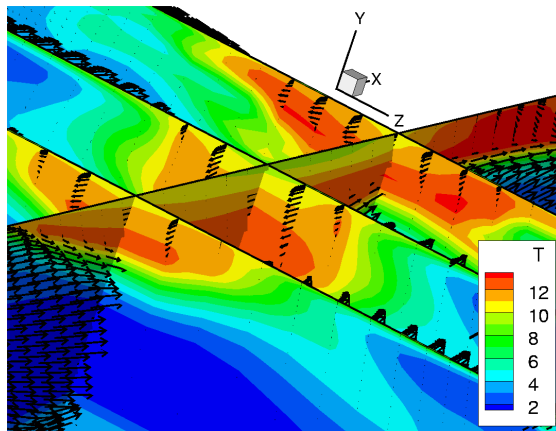
(c) Baseline T/T_0 Contours
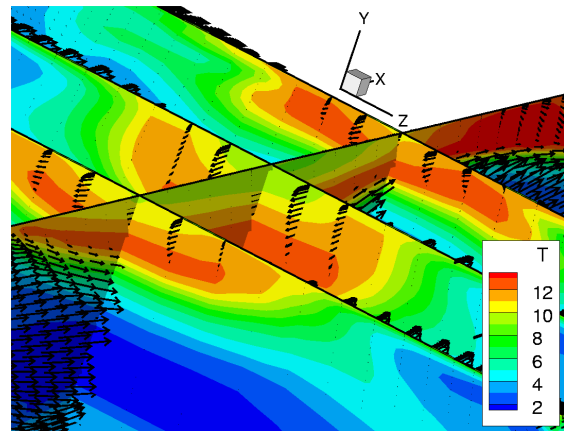
(d) Case1, k=0.7, Q=1 T/T_0 Contours

Figure 5.7:   Impact of EM Interaction on Inlet Separation Region where Arrows Represent the Normalized Local Velocity Vector
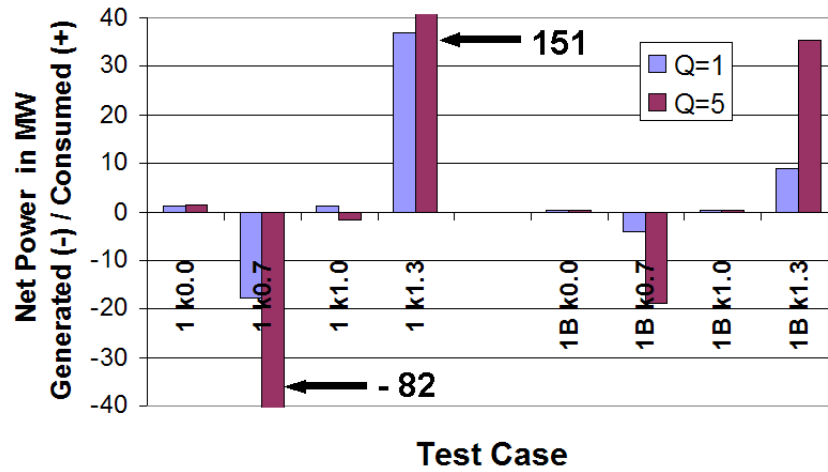
Figure 5.8: Comparison of Net Electric Power Generated/Required for Conductivity Cases 1 and 1B as Defined by $P_{gen} - P_{ion}$
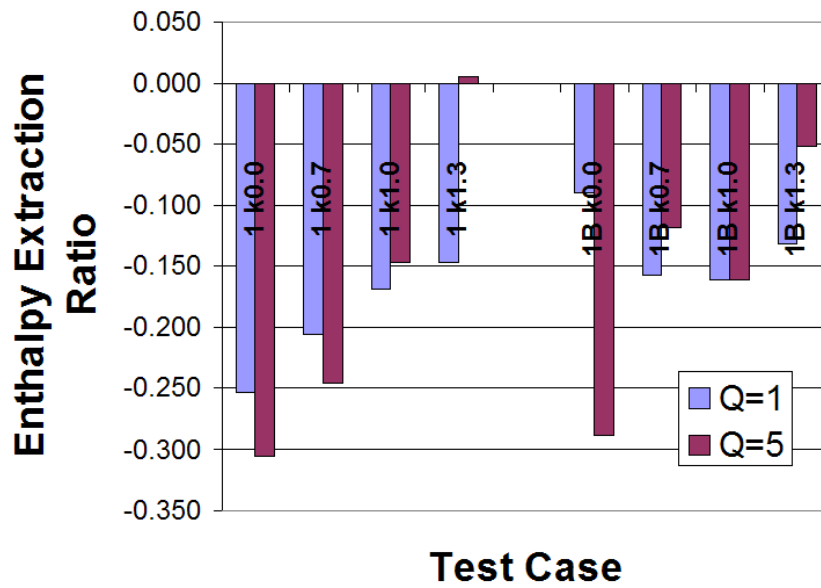
Figure 5.9: Comparison of Enthalpy Extraction/Addition for Conductivity Cases 1 and 1B

5.2.3 Results from Conductivity Case 1B. This case differed from Case 1 in that the conductivity was limited to the near-wall region of the cowl shoulder. Case 1B, with a plasma volume of 1.44m^3, more accurately simulated an electron beam ionization source with the maximum conductivity centered several centimeters from the wall and then falling off rapidly in the direction normal to the wall. As in Case 1, the addition of EM fields had a small, but noticeable, effect on the outflow properties, primarily with respect to temperature and pressure increases. However, the magnitude of these changes was much less than for the same EM interaction applied to Case 1. For example, the greatest change in exit pressure occurred for $k = 0.7, Q = 5$ and amounted to a 6.7% increase above the baseline inlet. This was to be expected in light of Case 1, as the interaction regions for 1B was only 48% of Case1. However, forces, heat transfer and EM terms did vary for differing parameters as applied to Case 1B, as discussed below.

Referring back to Figure 5.4, drag varied from 16% less than baseline for the $Q = 5$ accelerator to 68% more than baseline for the $k = 0.0, Q = 5$ parameters. Overall, these numbers reflected the same trends seen in Case 1 but typically at magnitudes of 1/3 to 2/3 of their Case 1 counterparts. As with Case 1, for a given k, there was an obvious change in drag for increased Q, due to the increasing Lorentz force. The near-wall conductivity region (being limited to the opposite side of the flow field away from the cowl lip) was unable to induce any additional mass spillage. Therefore, there was no contribution to thrust due to bypassed air flow as seen in Case 1. Regarding heating, all of the EM cases deposited energy into the flow through dissipation, but typically in less amounts than for Case 1. This was reflected in the heat transfer rates out of the control volume (Figure 5.6). For Case 1B, the minimum and maximum $\dot{Q}_w$ was 59MW and 143MW. The same trends as for Case 1 were seen in that $k = 0$ by far produced the most Joulean dissipation, $k = 1.3$ and $k = 0.7$ were comparable, and $k = 1.0$ produced the least amount. It was interesting to note that at $Q = 1$ Cases 1 and 1B had very similar values of wall heating for corresponding k values (with the exception of the $k = 0$ parameter). This fact demonstrated that

the placement of EM-interaction near the wall was the driving factor in determining the wall heat transfer. Overall, the targeted conductivity application did appear to be a relatively efficient method of limiting the overall drag increase due to Lorentz force. However, further work is recommended in order to determine the optimum distance off the wall to target the electron beam ionization in order to minimizing the additional wall heat load while retaining the drag reduction benefit.

Conductivity for these cases was somewhat higher than in Case 1, ranging between 0.85 and 0.97 mho/m. This was because densities near the wall were less than in the core flow, which from Equations 2.74– 2.76 implied conductivity should be higher as $\sigma \propto 1/\sqrt{\rho}$. By the same reasoning, the required P_{ion} per unit volume was also less than for Case 1. B-fields were on the order of 3T for $Q = 1$ and 6.5-7T for $Q = 5$. Once again, as seen in Figure 5.8, only the $k = 0.7$ MGD generator cases demonstrated a substantial net power generation after ionization. A net of 4.1MW was produced for $Q = 1$ and 19MW for $Q = 5$ which was 23% of that produced for the corresponding parameters applied to Case 1. The required power for ionization was on the order of 0.5MW for all cases. The enthalpy extraction ratios, η_g, were generally comparable to Case 1, which in light of the differing volumes of the interaction region, revealed that enthalpy extraction due to EM interaction was not as significant as other mechanisms such as wall heat transfer.

5.2.4 Summary of Conductivity Cases 1 and 1B.   From this analysis, it appeared that neither Case 1 nor 1B were effective at significantly increasing the mean pressure at the outflow plane or improving the efficiency measures. One exception to this conclusion regarding pressure for $k = 0.0, Q = 5$ must be made. Even in this case, the quasi-1D plot of Figure 5.2 revealed that the pressure increase from the EM interaction upstream of the separation region was substantially reduced by the sidewall expansion into the isolator. Several notable improvements were observed, though. Placement of the EM-interaction region near the wall was the most important factor in determining the wall heat transfer. Furthermore, targeting the conductivity
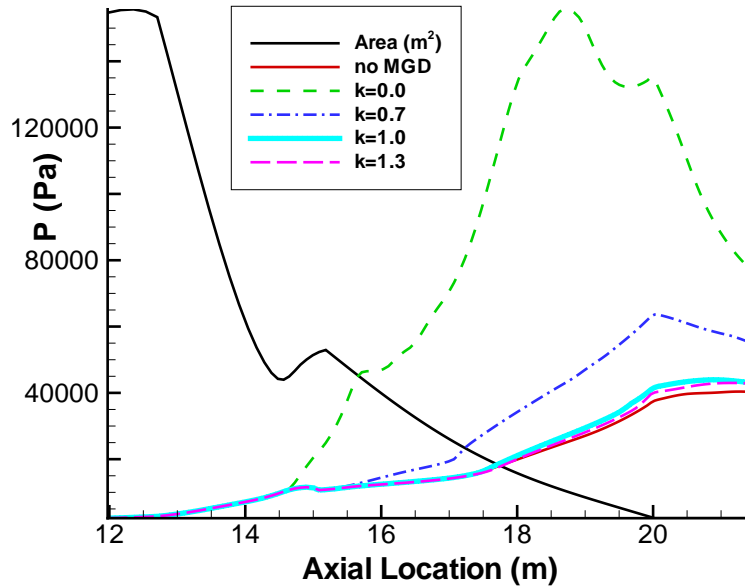
Figure 5.10: Mean Inlet Pressure for Case 2 with Varying k and $Q = 5$

in this region was a relatively efficient method of minimizing drag increase with respect to the baseline inlet. However, these two conclusions together meant further work is recommended in order to determine the optimum distance off the wall to target the electron beam ionization. Finally, the additional mass flow spillage caused by placing the interaction region near the cowl lip had a noticeable impact on the inlet flow. While developing a mass flow rate active control system along the lines of Macheret's conceptual work [47], was beyond the scope of this work, this computational modelling serves as the first high fidelity proof of this potential application.

   5.2.5   *Results from Conductivity Case 2.*   Case 2 continued the conductivity region downstream through the separation region until reaching the inlet throat as shown in Figure 5.1(b). This plasma was about 2.6 times the volume of the Case 1 plasma, or 7.59m^3. Consequently, the impact to forces, heat transfer and, in contrast to Case 1, exit plane flow properties was significant and varied greatly with the different parameters. For example, as shown by Figure 5.10 the exit plane pressure was 30kPa, or 74%, above the baseline case for $k = 0.0, Q = 5$. Other than the $k = 0.0$
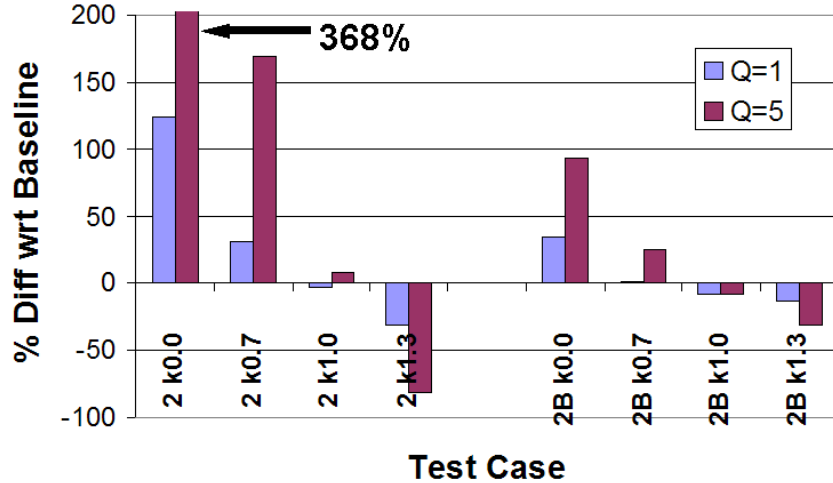
Figure 5.11:   Comparison of Net Inlet Drag for Conductivity Case 2 and 2B

parameter, $k = 0.7$ cases showed appreciable pressure increases of 18% and 25% for $Q = 1$ and 5, respectively. However, all of these pressure rises were accompanied by a large amount of dissipative heating, resulting in a maximum mean temperature of 3265K for the $k = 0, Q = 5$ case. It was apparent from these results and a review of Figures 5.2 and 5.10 that raising the pressure in the isolator was accomplished most effectively by modifying the sidewall expansion fans into the inlet throat.

Looking further at the drag forces and heating, the accelerator parameters of $k = 1.3, Q = 5$ reduced the net inlet drag to 16kN (or 81% less than baseline), as shown in Figure 5.11, but at the substantial cost of 240MW of electrical power put into the system. While all cases resulted in overall inlet drag, the $k = 1.3, Q = 1$ case reduced the baseline value by 31%, at a cost of only 30% of the electrical power consumed at $Q = 5$. As k decreased (or Q increased for a given k), the drag increased, reaching a maximum value of -404kN (a 368% increase with respect to baseline) for $k = 0, Q = 5$. This made sense in both respects as a decreasing k and/or increasing Q means an increasing Lorentz force in the negative axial direction. The increased mass flow spillage of Case 1, and its effect on drag, was not seen with Case 2 because as discussed in Subsection 5.2.2, only Case 1 extended the MGD interaction region upstream of the cowl lip plane. Regarding $\dot{Q}_w$ and the results presented in Figure 5.12,
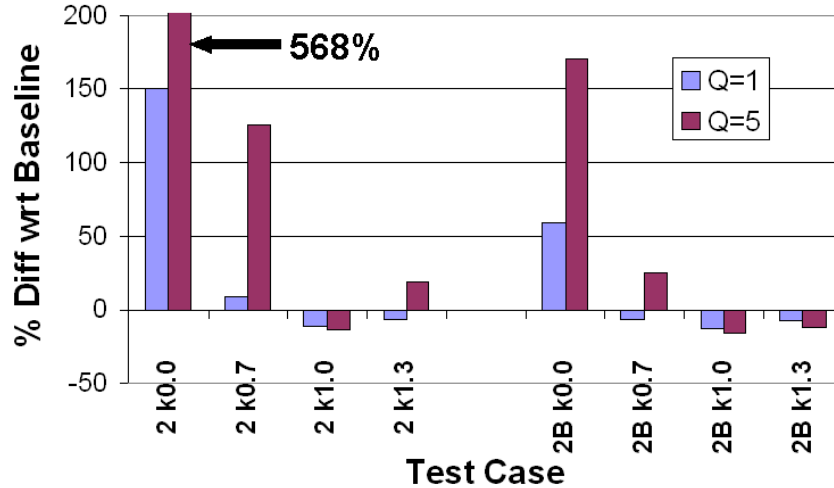
Figure 5.12:   Comparison of Wall Heat Transfer for Conductivity Cases 2 and 2B

all cases resulted in heat transfer out of the CV. Just as with Case 1, small decreases were seen with respect to baseline for parameters that resulted in a relatively low level of EM interaction. As seen previously with Case 1, increasing the EM energy interaction always results in increased dissipative losses regardless of whether the device acts as a generator or an accelerator. The trend in heating was the same as for Case 1 in that the greater the departure from $k = 1$, the higher the dissipation and subsequent heating. The peak value was an astounding $465MW$ for the $k = 0, Q = 5$ case.

Finally, conductivity and B-field values for this case were comparable to those of Case 1 because the density increased slowly through this portion of the inlet. Values of σ ranged between 0.51 and 0.79 mho/m, and B-fields were on the order of 3.5T for $Q = 1$ and 7.5-9.2T for $Q = 5$. The $k = 0.7$ cases generated a net 39MW and 151MW of electrical power for $Q = 1$ and 5, respectively as depicted in Figure 5.13. In addition to the $k = 0.7$ cases, the $k = 1, Q = 5$ case demonstrated a net power generation after ionization of 25MW. These large values of P_{gen} are important, because there are other electrical power requirements that must be met aside from the ionization power requirements. However, these power requirements (e.g. electromagnet power supplies and control circuitry) were outside the scope of this modelling effort. With the plasma
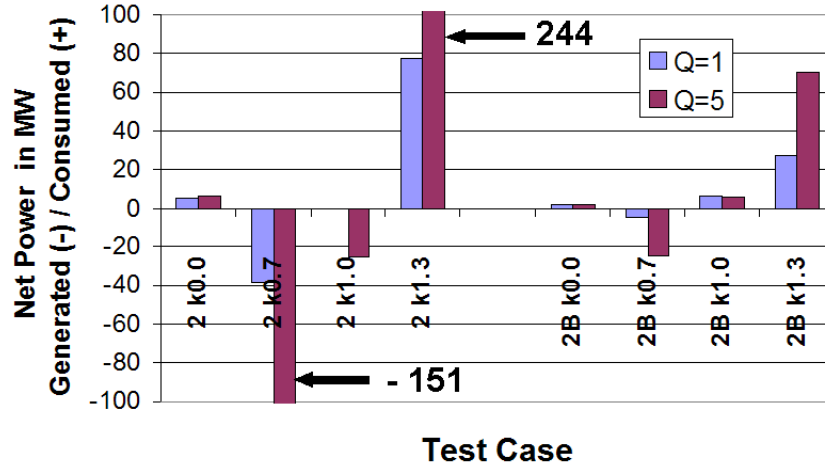
Figure 5.13: Comparison of Net Electric Power Generated/Required for Conductivity Cases 2 and 2B

volume being 2.6 times greater than that of Case 1, the required power for ionization was on the order of 4.1-6.3MW for all cases. This was up to approximately 3–4 times the required P_{ion} of Case 1, demonstrating that in light of the axially increasing inlet density, the per unit volume cost of producing the plasma was approximately the same for both Case 1 and 2.

  5.2.6 Results from Conductivity Case 2B.   Although not explicitly pictured, referring back to Figure 5.1, one can visualize Case 2B as being a combination of the near wall profile of 1B extended axially to the same point as Case 2. Case 2B had a plasma volume of 3.76m^3. Focusing the EM interaction in the near-wall and especially the separated-flow region, resulted in slight increases in the exit flow pressures and temperatures. Exit Mach numbers decreased by less than 10% with respect to baseline for all but the $k = 0.0, Q = 5$ case which decreased by 20%. Efficiencies relative to the baseline inlet were similar to their Case 1B counterparts as seen in Figure 5.14. The decreases in efficiency measures were not as great as those for Case 2 because of the smaller, targeted interaction region. Likewise, results from Case 2B did not exhibit the adversely large heat loads and electrical power requirements seen in Case 2.

(a) Total Pressure Ratio
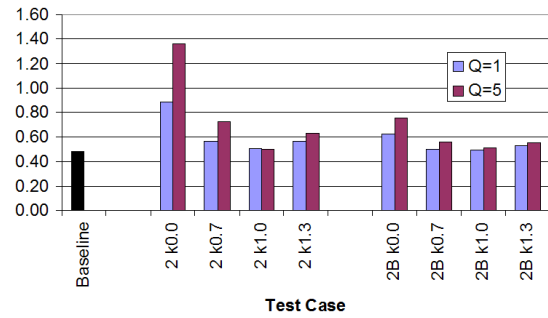
(b) Dimensionless Entropy Rise
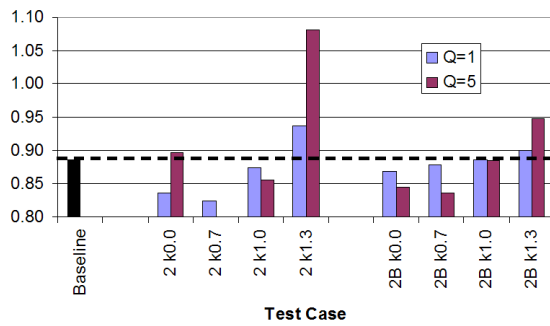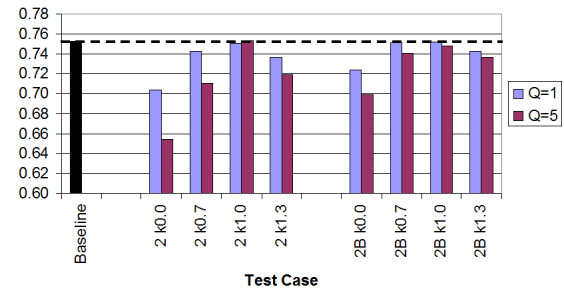
(c) KE Efficiency

(d) Adiabatic Compression Efficiency

Figure 5.14:   Inlet Efficiency Metrics for Cases 2 and 2B

Table 5.2: Selected Results for MGD Accelerators, $k = 1.3, Q = 5$

Property	Units	Case 2	Case 2B
p_e	kPa	42.8	41.8
T_e	K	1418	1316
Axial Force	kN	-16.1	-60.1
Wall Heat Transfer, $\dot{Q}_{ht}$	MW	-82.9	-61.4
Net Power	MW	244	70.0
Total Pressure Ratio, π_c	–	0.1838	0.1506
Non-dim Entropy Rise, $\Delta s/C_p$	–	0.6241	0.5522
KE efficiency, η_{KE}	–	1.0805	0.9476
Adiabatic Compression Eff., η_c	–	0.7188	0.7357

For example, Table 5.2 compares the $k = 1.3, Q = 5$ accelerator parameters for Cases 2 and 2B. Case 2B had significantly less EM work done, resulting in less heat generation and lower electrical power requirements. Of course, due to the inevitable Joulean dissipation, there was a measurable temperature rise in all instances as also reflected in Table 5.2. Though not shown in Table 5.2, the $k = 0, Q = 5$ parameters had the most negative impact to compression efficiency, with Case 2B being 5.4% less efficient than baseline. Still, this was a marked improvement over the 9.9% lower efficiency for the same parameters applied to Case 2.

The drag results for Case 2B varied widely, but as seen in Figure 5.11, it was a minimum of 31% less than baseline at $k = 1.3, Q = 5$. A maximum drag value of 94% greater than baseline was obtained for Case 2B when $k = 0.0, Q = 5$. From Figure 5.12, heat transfer out through the walls was a minimum for $k = 1.0, Q = 5$, with a value of 58MW, 16% less than baseline. Maximum $\dot{Q}_w$ corresponded to the $k = 0, Q = 5$ parameter (as in the other cases), having a specific value of 188MW (177% above baseline). Trends for heating and drag followed the other cases. Conductivity was somewhat higher than in Case 2, ranging between 0.77 and 0.98 mho/m. As with Case 1B, B-fields were on the order of 3T for $Q = 1$ and 6–7.5T for $Q = 5$. Once again, Figure 5.13 revealed that only the $k = 0.7$ cases demonstrated a net power generation after ionization with Case 2B producing a net of 5MW for $Q = 1$ and 24MW for $Q = 5$. The required power for ionization was on the order of 1.6-1.8MW

for all cases. Referring back to Figure 5.14, the MGD accelerators for Cases 2 and 2B showed marginal improvement in flow properties as well as significant drag reduction and increased η_{KE}. However, these cases also required a very large electrical power input. This detrimental factor was reduced to a great extent by localizing the plasma region to the near wall in Case 2B, resulting in an electrical power requirement of 27 and 70MW, for $Q = 1$ and $Q = 5$, respectively.

5.3 Summary of Results, Conclusions and Recommendations Regarding Localized EM Flow Control

With respect to the specific application presented here, localized MGD flow control was marginally successful in mitigating the pressure losses due to the expansion around the cowl shoulder. The $k = 0.0, Q = 5$ parameter, in particular, was able to significantly raise the average inlet pressure. Yet, the penalty in terms of drag and heating excluded its consideration as a viable solution to the problem. All other parameters for Cases 1 and 1B were not effective at significantly increasing the mean pressure at the outflow plane or improving the inlet efficiency. Gains incurred by these parameters from the EM interaction upstream of the separation region were all but negated by the sidewall expansion into the isolator at the inlet throat.

Placement of the EM-interaction region near the wall was the most important factor in determining the wall heat transfer, and targeting the conductivity to this region did appear to be a relatively efficient method of limiting drag increases. However, further work is recommended in order to determine the optimum distance off the wall to target the electron beam ionization. Finally, with respect to Case 1 only, the additional mass flow spillage caused by placing the interaction region near the cowl lip had a noticeable impact on the inlet flow. This computational model provided the first high fidelity verification of the potential of using MGD to modulate the mass flow rate into the engine.

For the MGD generator cases of $k = 0.7$, meaningful electrical power generation was achieved. Although it only slightly increased the flow pressure going into the

isolator, MGD acceleration, particularly for Case 2B, was able to efficiently reduce the net inlet drag. It did this while minimizing the increase in heat transfer and decrease in overall efficiency measures. This was due primarily to increasing the flow momentum as it passed through the sidewall expansion into the inlet throat. Therefore, it was concluded the use of an MGD accelerator to locally increase flow momentum was an effective approach to improve flow into the isolator of this scramjet model. Further, if the P_{ion} requirement is of prime consideration, limiting the ionized flow to the near-wall region is an acceptable compromise.

VI. Application of MGD Energy Bypass to Flowpath

6.1 Introduction

A significant discussion in Chapters I and II, and in particular Section 1.2, explained the theory behind MGD power generation systems and the energy bypass concept. The reader is referred back to these parts of the document for details. In summary, the MGD energy bypass method is a concept for both producing vehicle electrical power and improving the scramjet's performance. Theoretically, it does this by efficiently removing a portion of the inlet's high stagnation enthalpy, converting it to electrical power, and returning it directly to the expansion system. In this way, the inlet compression is accomplished more efficiently than by the shock train alone. Therefore, the combustor can impart more energy into the flow before running into stagnation temperature limits. This application has been well documented in References [10, 21, 34–36, 43, 54, 60].

The research documented in this chapter tested this application to a level of computational fidelity never before attempted. The next section documents the results for MGD power generation in this engine by first examining the traditional configuration wherein the MGD generator is placed upstream of the combustor. In addition, the concept of combustor-based MGD power generation was explored. This concept, widely pursued in the 1960's in the context of commercial electrical power generation [70], has recently reappeared as a promising concept for scramjet engines as proposed by Macheret, et al [50, 73, 74], among others. The isolator-based generator with the highest electrical power generation was selected for the MGD energy bypass system and several different accelerators were analyzed as described in Section 6.3. Finally, both of these sections are summarized and several conclusions and recommendations specific to this chapter are presented.

6.2 MGD Power Generation

6.2.1 The Conventional Bypass Approach: MGD Power Generation Upstream of the Combustor. Two approaches were taken to characterize the performance of isolator-based MGD power generation in this engine. The first approach was a parameter based study similar to that of Chapter V's localized flow control. This approach, which specified the electric field, was done in order to test a wide range of conductivity profiles and load factors (k) at a single interaction parameter ($Q = 1$). The second approach applied higher fidelity to select cases by specifying electrode locations and their electric potential and solving for the resulting electric field and conduction current as described in Section 2.1. In addition to $Q = 1$, the second approach tested the higher magnetic field strengths associated with $Q = 5$. Among other results, it will be shown that electrode placement was critical to successful power generation, and that there was a large difference in performance depending on the load factor, k, and interaction parameter, Q, used.

Numerous runs of the isolator-based MGD generator were performed. Most of these runs specified the electric field. Runs were first delineated by how far the conductivity region extended downstream from the inlet throat as a percentage of the isolator length. Three lengths were tested, 20%, 60% and 100%, as shown in Figures 6.1(a)–(c). As in Chapter V, both a full cross-section profile, referred to here as Case 1E, and a near-wall profile, referred to as Case 2E (e.g. Figure 6.1(d)), were compared. For each conductivity profile, load factors of 0.6, 0.7, and 0.8 were tested. Additional runs were made where the electrode location and electric potential was specified. Since the best results for the specified electric field runs occurred at full isolator length, each electrode run evenly spaced four electrodes along this length as seen in Figure 6.2. Half of the runs placed the electrodes on the +/- Z-faces (referred to as 'K-elec' runs), while the remaining runs placed the electrodes on the +/- Y-faces ('J-elec'). As with the first approach, $k = 0.6$, 0.7, and 0.8 were examined, but this time at both $Q = 1$ and 5. As a final note regarding the problem setup, the baseline inlet without MGD characterized in Subsection 4.4.1 and used in Chapter V was again

used here for determining the performance changes due to the MGD generators. While efficiency metrics are presented in the same manner as in Chapter V, changes in forces and heating are presented as percentage differences with respect to this baseline.

(a) Case 1E-20%

(b) Case 1E-60%

(c) Case 1E-100%

(d) Case 2E-100%
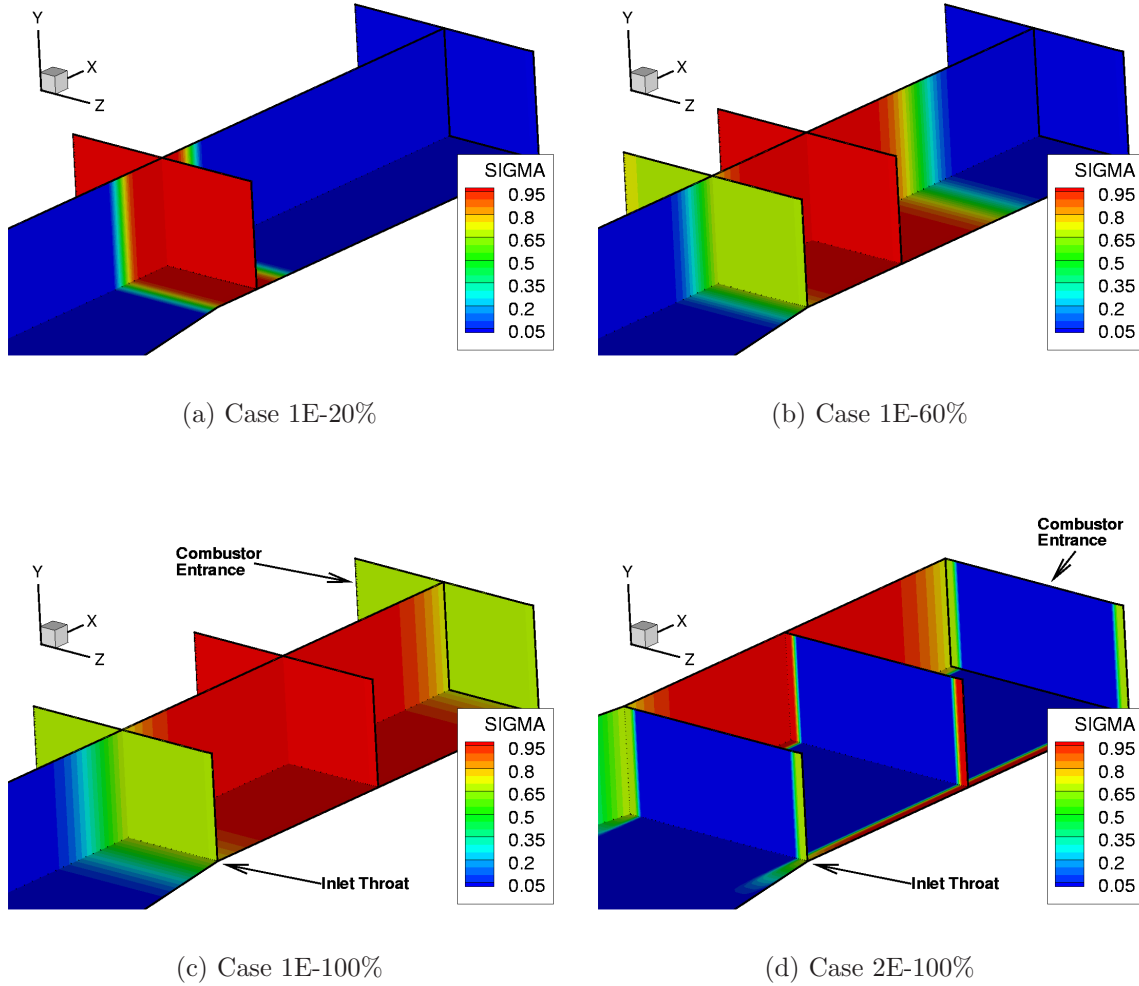
Figure 6.1:   Conductivity Profiles for Isolator-Based Generators with Specified Electric Field

MGD power generation is first and foremost about efficient conversion of flow enthalpy into electrical power. As seen in Figure 6.3, a significant difference was found between methods as well as between individual runs. Beginning with a look at the specified $\vec{E}$-field cases (Case 1E and Case 2E), several expected results were obtained

(a) K-elec   (b) J-elec
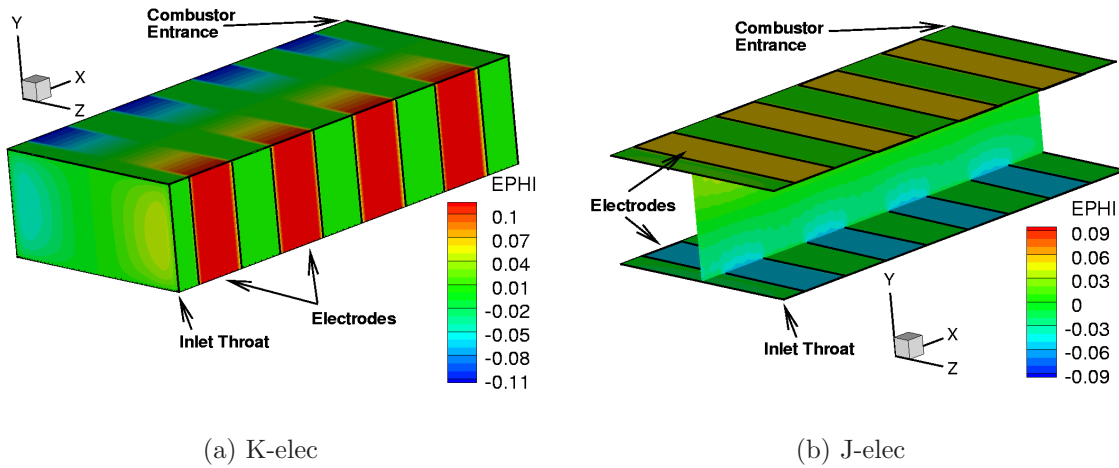
Figure 6.2: Electrode Configurations for Isolator-Based Generators with Specified Electric Potential
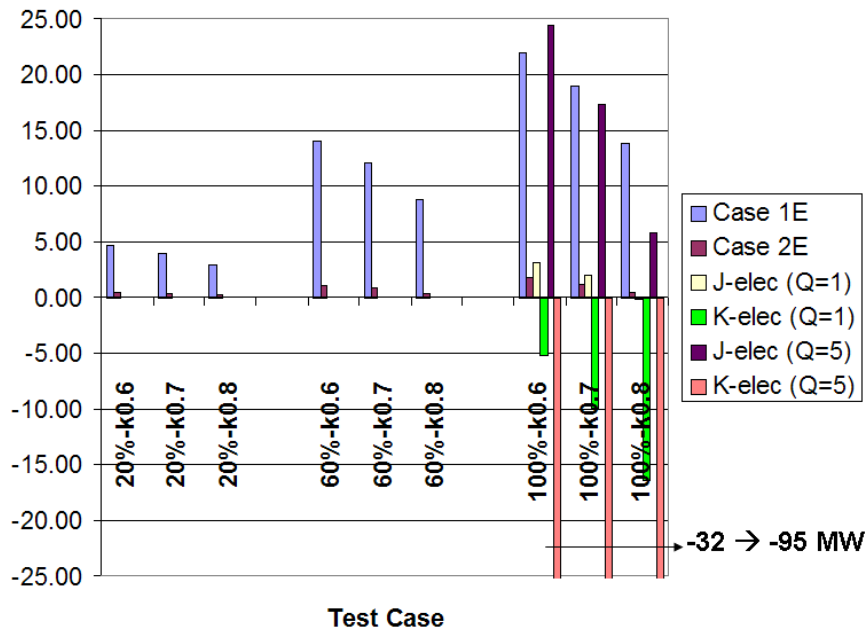
Figure 6.3: Comparison of Electrical Power Generation/Consumption for Isolator-Based MGD Generators

that were in keeping with reduced-order analytical treatments. For example, in an ideal MGD generator, it can be shown that P_{gen} is related to k by Equation 6.1 [70]. Power is then a quadratic function of k with maximum power generation occurring at $k = 0.5$. With respect to a decreasing value of k, all of the results supported this. This included the K-elec cases which experienced a net power consumption; albeit a consumption that decreased as k approached 0.5. The unique circumstances that generated this result will be explained shortly.

$$P_{gen} = \sigma V^2 B^2 k(1 - k) \qquad (6.1)$$

Equation 6.1 describes the power generated per unit volume, such that an increase in the plasma volume (e.g. through increasing the axial extent of the generator) made for a substantial increase in power extraction. Comparing Case 1E to 2E further demonstrated that co-locating the bulk of the plasma volume in the center of the channel was a more efficient means of producing power. For example, comparing Cases 2E to 1E where $k = 0.6$, it was seen that, regardless of the axial extent of the generator, the plasma volume ratio was 20%–23%. However, the ratio of total power produced was only 9.5%. Referring again to Equation 6.1, it was clear that the dependence of P_{gen} on V^2 meant that localizing the plasma to the near wall region (where V was relatively small) was relatively inefficient. This result also makes sense from the perspective that the useful work portion of the EM interaction is given by $\vec{V} \cdot (\vec{j} \times \vec{B})$. Therefore, if the plasma volume is limited to the near wall region, where $\vec{V}$ is small in a viscous flow, then relatively little power will be extracted. While current technology is getting close to realizing the centimeter-scale, near wall $\vec{B}$ field strengths of 4.0–4.4T that typified Case 2E, extending these fields across a real scramjet isolator, with distances on the order of a meter, will require a substantial scientific breakthrough. In the end, Case 100%-k0.6 produced the most power but with a required magnetic field strength of 10.5T and conductivity of 0.40mho/m.

In every respect, the specified $\vec{E}$-field cases behaved as theory would suggest, but at first glance the same could not be said in all regards for the electrode-based cases. As the applied $\vec{B}$-field grew (i.e. Q increasing), the EM-interaction increased roughly as $|\vec{B}|^2$, which was expected. For the J-elec cases, increasing Q from 1 to 5 increased the total P_{gen} by factors from 3–4.5 as k decreased from 0.8 to 0.6. For the K-elec cases, the net power consumption was increased by factors from 7–12 as the nominal load factor decreased from 0.8 to 0.6. As was seen in Figure 6.3 and further quantified here, the net EM-interaction was opposite between the J-elec case which generated electricity and the K-elec case which required additional electricity from an external source. This result was unexpected as only two changes were made between the two configurations. First, the electrodes were placed on different walls and the $\vec{B}$ field was realigned accordingly ($+B_y$ for K-elec and $-B_z$ for J-elec, respectively). Second, a higher electrode potential was used for the K-elec configuration to maintain the same nominal k in spite of the greater distance between the cathode and anode of each electrode pair.

Analysis uncovered the cause for the significantly different performance. For every J-elec run, greater than 50% of the total EM-interaction took the form of work done by Lorentz Forces on the fluid. The opposite was true for all of the K-elec runs, where dissipation accounted for over half of the total interaction. In fact, for the K-elec case of $k = 0.8$ and $Q = 5$, dissipation was 63% of the total interaction, or 1.8 times the corresponding J-elec case. Recall from Subsection 2.4, the EM energy interaction, $\vec{E} \cdot \vec{j}$, consists of the sum of the Joulean dissipation and the rate at which the Lorentz Force does work on the gas as shown again here in Equation 6.2.

$$\vec{E} \cdot \vec{j} = |\vec{j}|^2 / \sigma + \vec{V} \cdot (\vec{j} \times \vec{B}) \tag{6.2}$$

Furthermore, positive values of $\vec{E} \cdot \vec{j}$, such as occurred with the K-elec configuration mean the external circuit is supplying electricity to the gas, as occurs in an MGD accelerator. However, in an accelerator, the $\vec{V} \cdot (\vec{j} \times \vec{B})$ work term would be positive

with a magnitude that would typically exceed the dissipation. In every K-elec case tested, however, the Lorentz work term was negative. This combination of positive $\vec{E} \cdot \vec{j}$ and negative $\vec{V} \cdot (\vec{j} \times \vec{B})$ is only possible if the applied electric field, $\vec{E}$, is aligned with the induced electric field, $\vec{V} \times \vec{B}$, rather than opposed to it. To verify this was what had occurred, plots of the conduction current, $\vec{j}$, and $\vec{E} \cdot \vec{j}$ were examined for both J-elec and K-elec configurations. Figure 6.4 shows that the K-elec configuration experienced this reversed $\vec{E}$ field condition throughout a significant portion of the plasma volume, but especially near the electrically insulated wall regions between successive electrodes. (Plots for J-elec reflected this condition, also, but to a substantially smaller magnitude and extent than that seen with K-elec.) Due to $\vec{V} \times \vec{B}$, the largest current component acted in the +Z–direction as seen in Figure 6.4(a). Especially strong j_z currents were clearly visible at the electrode-insulator junctions. In light of this, if the configuration was truly acting as an MGD generator, the applied $\vec{E}$ field should have been aligned predominantly in the -Z–direction. Figure 6.4(b), though, reveals large areas where $\vec{E}$ was aligned with $\vec{j}$, confirming that the device was operating as neither a generator nor an accelerator. Rather, external electrical energy was deposited into the gas in a direction that reinforced the -X–directed Lorentz Force and added additional dissipation (i.e. heating).

The obvious issue, then, was determining the mechanism causing substantial portions of the $\vec{E}$ field to reverse from the direction set by the specified electrode potential. A similar effect, but to a lesser degree, was documented by Gaitonde near the MGD generator walls of the AFRL scramjet [21]. The $\vec{E}$ field reversal was attributed to the vanishing induced field that occurred as $\vec{V}$ went to zero at the wall. In order to maintain the overall current direction and continuity, the local $\vec{E}$ field was reversed. It was believed this effect was compounded in the current research for two reasons. First, electric potential differences at the electrode-insulator interface may not have been subjected to the optimum numerical filtering as described in Reference [23]. This numerical instability would account for the large values of current seen at the electrode-insulator interfaces, in turn, leading to increased regions

(a) j$_Z$ Normalized by $V_0 B_0$ (b) $\vec{E} \cdot \vec{j}$ Normalized by $\rho_0 V_0^3$
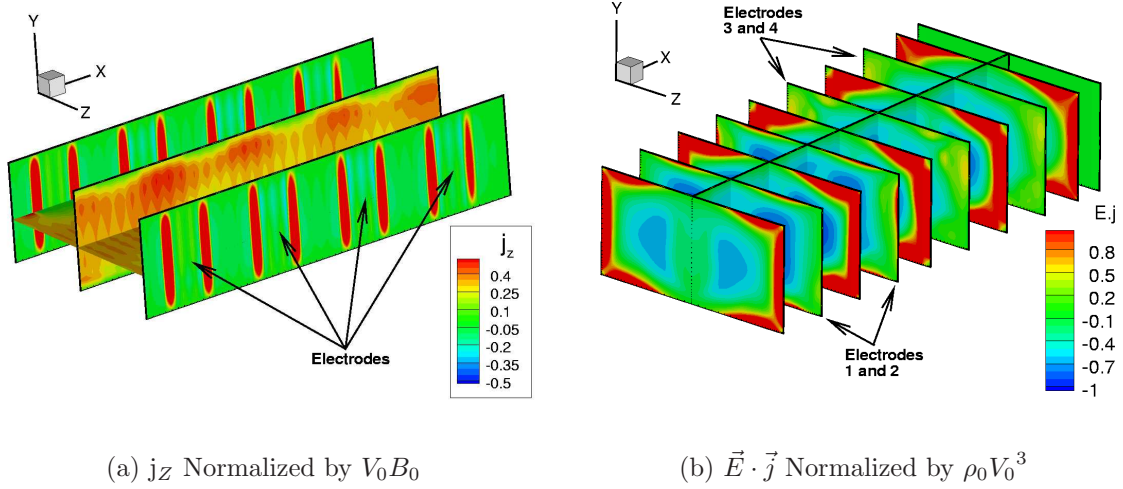
Figure 6.4:   Profiles of Normalized Conduction Current and Net EM Energy Interaction for the K-elec Configuration. ($k = 0.6$(nominal), $Q = 5$)

of reversed $\vec{E}$ fields. Second, the difference between K-elec and J-elec was that they assumed the same mean flow velocity, but because of the larger electrode spacing with K-elec, the applied electrode potential was much greater. This exacerbated the numerical instability along the electrode interface also contributing to the increased areas of $\vec{E}$ field reversal observed. In the end, this effect was obviously not intended and was caused by a numerical issue rather than a fundamental problem with the K-elec configuration. However, it emphasized the inherent difficulty of modelling the EM boundary conditions and highlighted the need to further develop the fidelity of the electrode modelling in the current computational approach.

In spite of this, it was still useful to compare the proper MGD generator performance of the J-elec configuration to that of K-elec. This is because changing flow conditions in a real scramjet will cause significant variations in load factor, leading to difficulties in maintaining proper EM field application. As can be from comparing the net power generation of the J-elec configuration to the consumption of the K-elec configuration (see Figure 6.3), this was exactly the kind of phenomena that made or broke the performance of the realistic MGD generators. The net power consumption with the K-elec cases significantly impacted the flow properties in several

ways as well, due to the large amounts of Joulean dissipation. Figures 6.5(a) and (b) clearly demonstrate this effect on both the decreased Mach number and increased temperature in the isolator with respect to both the baseline case and the J-elec case. The J-elec case did experience additional heating associated with its localized regions of reversed $\vec{E}$ field, but as can be seen, the effect was substantially less. Finally, a look at Figures 6.5(c) and (d) showed that pressure and velocity were also notably impacted. The combined effects of the Joulean dissipation and Lorentz Force (which was significant in the core flow regions of both J-elec and K-elec) acted to drive the mean pressures higher and velocities lower.

Bearing all of this in mind, the performance results came as no surprise. For example, a look at the drag in Figure 6.6(a), showed that all of the $Q = 1$ cases had about 10%–20% more drag than the baseline inlet. However, the $Q = 5$ cases for the J-face electrodes nearly doubled the drag, while the K-face electrodes had closer to 130% of the baseline drag. This last result regarding K-elec was irrespective of the nominal load factor used in determining the electrode potential; being a further manifestation of the mismatched EM field configuration which only contributed increased Lorentz force drag and substantially greater dissipation. This increase in dissipation for the K-elec cases was manifested in heat transfer rates in excess of 130% of baseline for $Q = 5$ as given in Figure 6.6(b). This was more than double that of the J-elec configuration with the same parameters.

Taken together, all of this added drag and heating reduced most of the overall inlet performance measures with respect to the no-MGD baseline. All four of these measures are graphed in Figure 6.7. From this figure, it can be seen that as a stand alone system component the MGD generators reduced the inlet efficiency in every metric with the exception of the kinetic energy efficiency for the K-elec, Q=5 cases. This particular result was spurious and attributable to the inordinate amount of heat put into the isolator that if it were possible to get it back out through an isentropic expansion would result in an increase in kinetic energy. On the positive side, for $Q = 1$ the efficiencies were fairly insensitive to the particular case configuration. From this, it
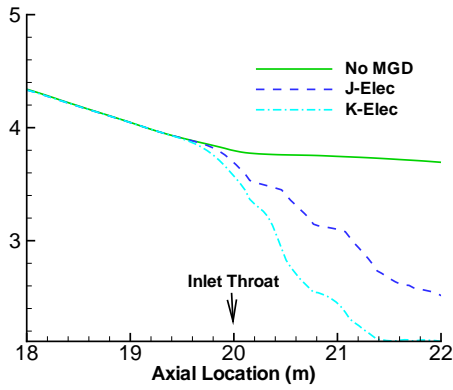
(a) Mach Number
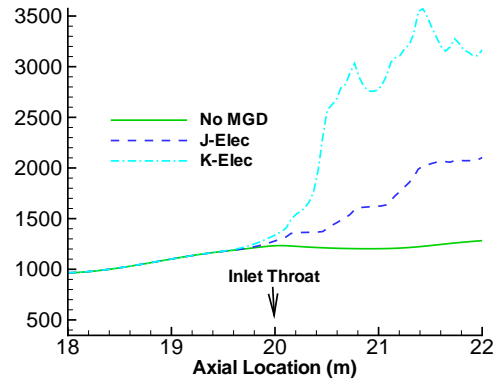
(b) Temperature (K)
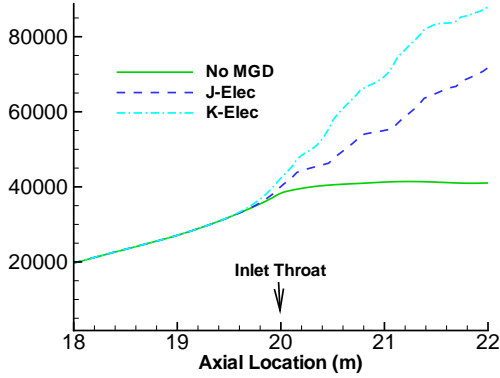
(c) Pressure (Pa)
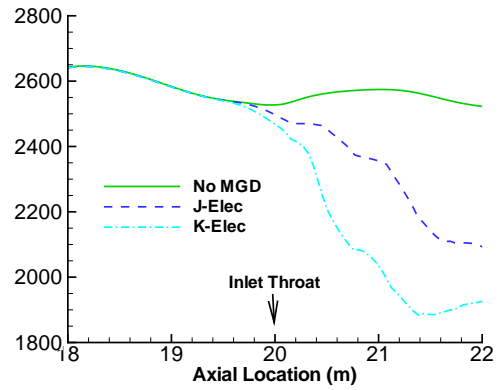
(d) u-Velocity(m/s)

Figure 6.5:   Comparison of Selected Cross-Sectional Averaged Flow Properties for Isolator-Based MGD Power Generation with Specified Electrodes. ($Q = 5$)

(a) Drag
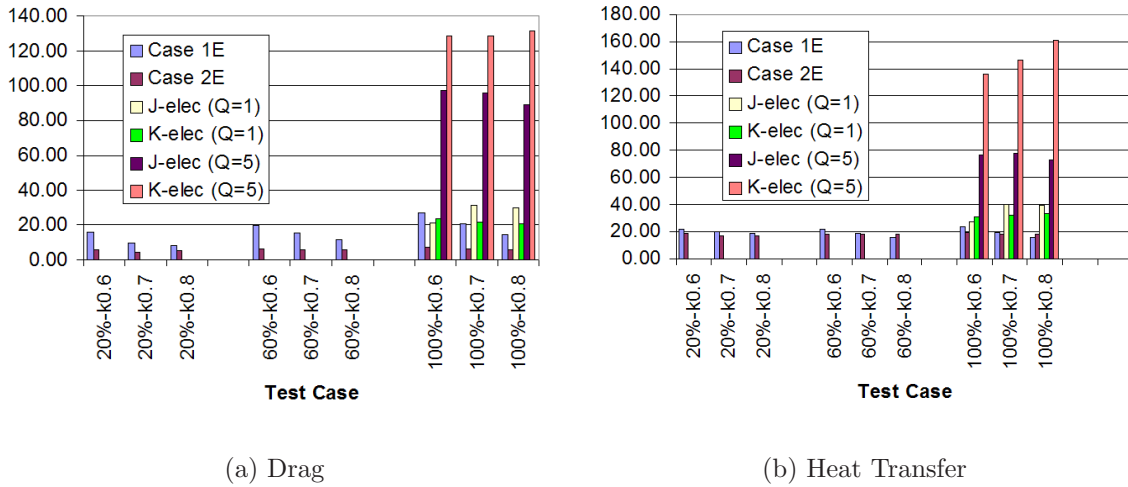
(b) Heat Transfer

Figure 6.6:   Increase in Inlet Drag and Heat Transfer Relative to Baseline for Isolator-Based MGD Power Generation

could be concluded that if the primary purpose for MGD power generation is to supply onboard electrical components, smaller generators with lower interaction parameters (i.e. lower system power requirements) should be considered. Moreover, it is more important to focus the interaction region in the core flow, where the useful work was a greater proportion of the overall interaction. However, if the goal is to maximize the work extraction with the goal of bypassing it directly to the expansion system, then the interaction parameter and plasma volume should be maximized. In light of this, it was decided to take the $Q = 5$, J-elec case as the MGD generator portion of the MGD Energy Bypass systems analyzed in Section 6.3. Compared to the same configuration at $Q = 1$, this case produced 7.9 times the electrical power, a result 11% better than the highest generating (but less realistic) specified $\vec{E}$-field models.

(a) π_c

(b) $\Delta s / C_P$

(c) η_{KE}
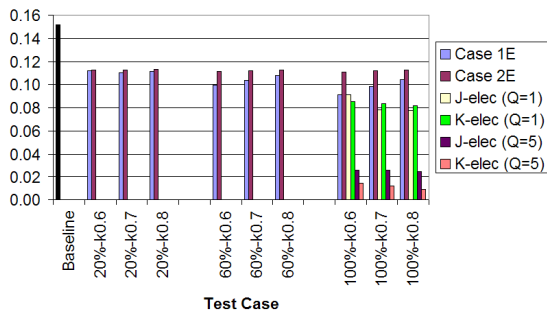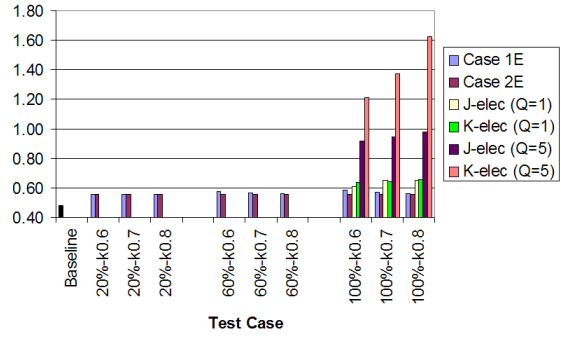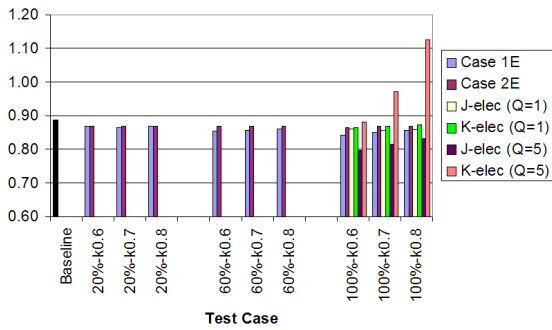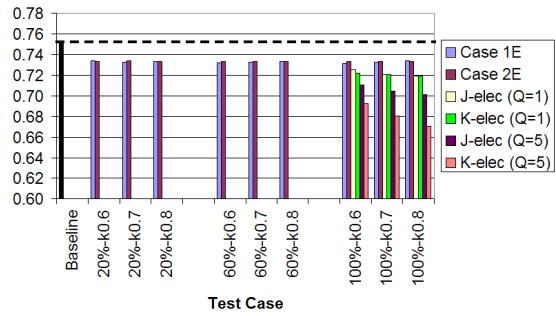
(d) η_C

Figure 6.7:   Comparison of Inlet Efficiencies for Isolator-Based MGD Power Generation
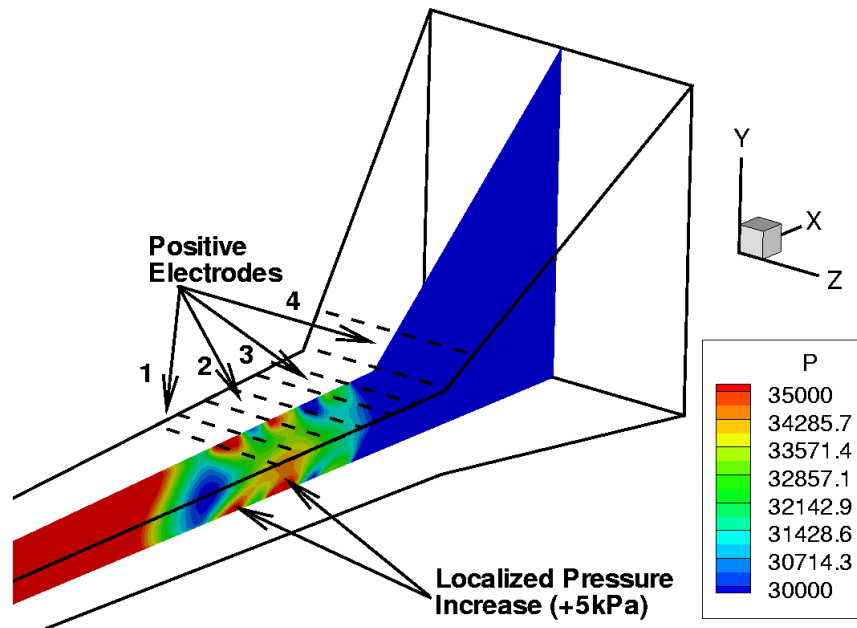
Figure 6.8: Combustor-based MGD Electrode Placement Super-Imposed on Results for Z-Midplane Pressure Contours Using Four Electrode Case (Note: Negative Electrodes Not Shown for Clarity)

6.2.2 Combustor-Based MGD Power Generation. Three configurations were used in order to test the combustor-based alternative to MGD power generation. All three configurations used the higher fidelity approach wherein paired electrodes with specified potential were placed in the aft end of the combustor, and in one case, extending into the beginning of the expansion nozzle. All three configurations used the farthest forward electrode pair (number 1 in Figure 6.8). The configurations were delineated by adding additional electrode pairs such that there was a total of two, three, or four pairs of electrodes, respectively. Because of the issue with $\vec{E}$ field reversal described in the previous section, the electrodes were placed on the +/- Y-faces as seen in Figure 6.8. Every configuration tested assumed $Q = 5$ and a nominal $k = 0.6$ in order to maximize power extraction and provide the same basis for comparison with the isolator-based MGD generators. Each electrode case was initialized from the same converged solution to the finite rate chemistry combustor and run for an identical computational time. Two additional cases were tested for

comparison purposes. The baseline configuration provided the scramjet performance without any MGD flow control, combining the baseline inlet with the finite rate chemistry combustor. Finally, a case (referred to as Isogen) was run using the isolator-based, J-Elec MGD Generator at $k = 0.6$ and $Q = 5$ and the finite rate chemistry modelled combustor. Its purpose was to provide a basis for determining the relative merit of the combustor-based MGD generators.

As expected, the addition of each electrode pair increasingly impacted the combustor flow field properties as shown by Figures 6.9(a)–(d). Taken as a whole, the figure shows that the localized effects caused by subsequent electrode pairs added to the effects due to upstream electrodes creating a cumulative effect on flow properties. This cumulative effect was not simply additive, however. Without a doubt, the single biggest effect was caused by the first electrode pair (EP1). For example, EP1 decreased the average cross-sectional Mach number by 11% to 2.90, but going from EP1 to EP4 only caused an additional 6.9% decline. This effect was visible in the remaining line plots as well, and the cause was clearly evident in the centerline pressure contours of Figure 6.8. In the forward portion of this figure, a decreasing pressure gradient is seen at the trailing end of the combustion reaction zone. This phenomena was discussed in detail in Section 4.4.2, and referring to the baseline case in Figures 6.9(c), it was seen the pressure continued to decrease all the way through the end of the domain. However, the addition of the MGD generator in this location caused localized pressure increases in the vicinity of the electrodes, where the conduction current, and therefore, the Lorentz Force was greatest. In fact, the pressure increases coinciding with EP1 and EP2, began to take on the sharply defined appearance of a small shock wave.

Regarding the performance of the combustor-based generators, electrical power generation, axial force, heat transfer, and total pressure ratio were compared to each other as well as the baseline and isolator-based generator cases. To begin, electrical power generation was examined. It was apparent from the results presented in Figure 6.10 that the combustor-based generation was superior in this regard. Foremost,
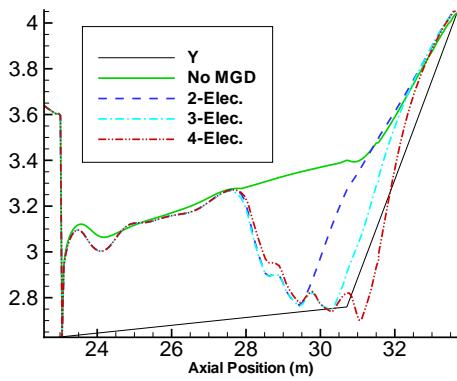
(a) Mach Number
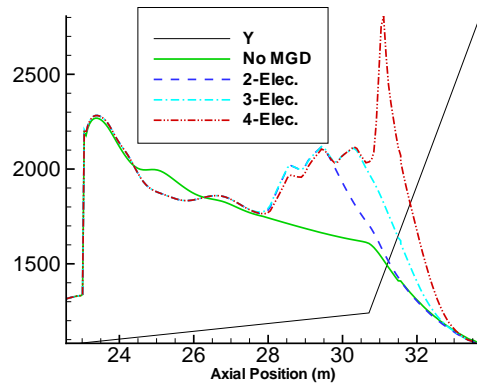
(b) Temperature (K)
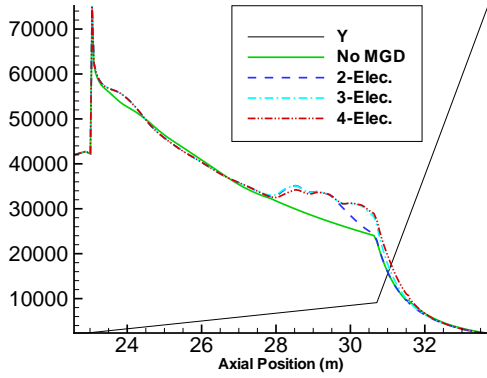
(c) Pressure (Pa)
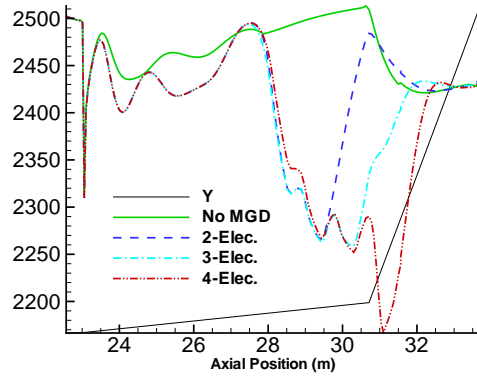
(d) u-Velocity(m/s)

Figure 6.9:   Comparison of Selected Cross-Sectional Averaged Flow Properties for Combustor-Based MGD Power Generation with Specified Electrodes. ($Q = 5$)
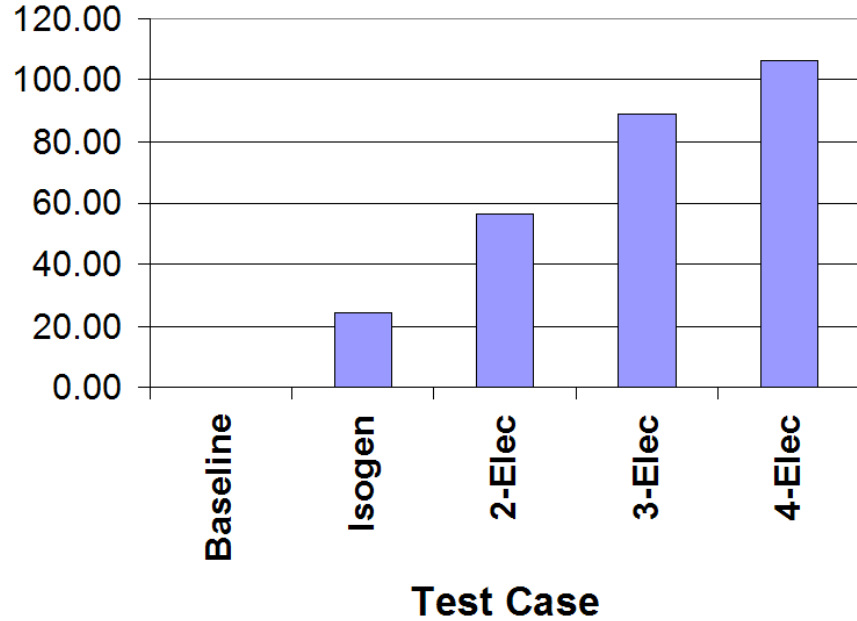
Figure 6.10:   Net Electrical Power Production (in MW) for Combustor-Based MGD Generators

the plasma volume in the 2-Elec case was 56% greater than for the isolator-based generator, and similarly the 4-Elec case had 3.7 times the isolator-based volume. However, considering the power generation per unit volume, it was seen that the combustor-based cases had values of 12, 10, and 9 MW/m^3 while the isolator-based case only achieved 8 MW/m^3. This was attributable to the lower density in the aft end of the combustor which decreased the ionization cost. For example, the required ionization power density for Elec2 was 578kW/m^3, while for the isolator generator case, it was 991kW/m^3.

Axial force results slightly favored the combustion-based generators as well although the presence of any MGD generator resulted in a total drag increase. Figure 6.11(a) shows that the total axial force (inlet plus combustor and expansion surface) on the baseline engine resulted in an overall drag of 63.7kN. The reasons for this poor performance was discussed at length in Chapter IV, but in summary neither the combustor nor expansion surface geometries approached their predicted results. However, it was still useful to use this result to evaluate the MGD system impacts.

In this regard, it was seen that the net effect of the isolator-based generator was an overall drag increase of 33% to 84.6kN. The aft generators performed marginally better in this regard with total drag ranging from 80.0kN – 80.8kN. Heat transfer, however, favored the isolator-based generator, with the exception of the 2-Elec case. As seen in Figure 6.11(b), the heat transfer for both of these cases was 44% above the baseline combustor value. However, in the case of the isolator-based generator this was an added heat load above that already incurred in the isolator. As expected, the remaining combustor-based cases increased their heat transfer into the gas as the number of elctrodes and the volume of the interaction region increased. Finally, a look at total pressure ratio again favored the combustor-based generators. It should be noted, that the ratio for the overall engine was taken as the product of the inlet and combustor ratios. Figure 6.11(c) showed that the overall efficiency with respect to this metric was low for all cases, with a value of 1.3% for the isolator-based generator and 1.8% for both the baseline and combustor-based generator engines. In light of this, the combustor-based generators were felt to be slightly more efficient.
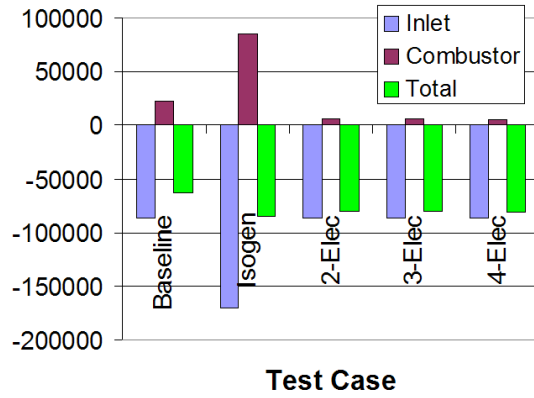
(a) Axial Force (N)
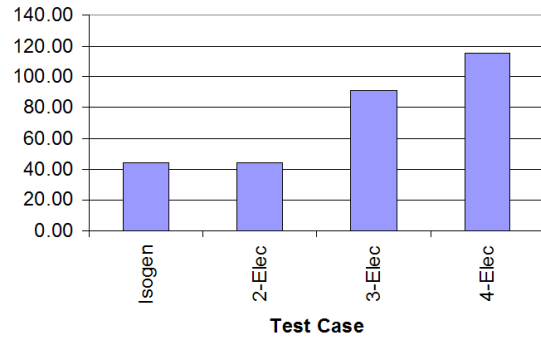
(b) Heat Transfer Relative to Baseline Case
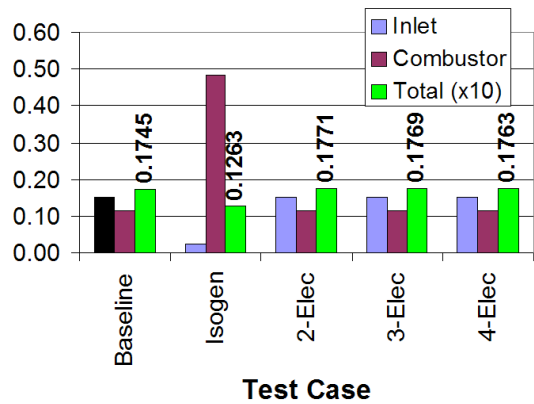
(c) Total Pressure Ratio

Figure 6.11: Comparison of Component and Total Axial Force, Control Volume Heat Transfer, and Total Pressure Ratio for Combustor-Based MGD Power Generation Using Specified Electrodes. ($Q = 5$)

6.3 MGD Flow Acceleration and Energy Bypass

Numerous cases were run with nominal load factors, k, greater than one in an attempt to characterize the effectiveness of MGD acceleration in the aft end of the combustor and obtain a self-powered MGD bypass system. In addition, for every load factor tested interaction parameters, Q, of 1 and 5 were also tested to examine the impact of increasing the $\vec{B}$ field. The specified electrode method was used for all cases using the same configuration as the two and four electrode pair cases from the combustor-based generation runs (refer to geometry in Figure 6.8).

Although all of the cases used a specified electrode potential based on $k > 1$ and a mean value of the local velocity, it was found that values of $k = 1.1$ and $k = 1.3$ actually acted in a generator fashion. Referring back to the discussion of Subsection 6.2.1, what happened in these cases was that the specified potential produced an E-field that, in large areas of the interaction region, had a smaller magnitude than $\vec{V} \times \vec{B}$. In other words, the Lorentz force was acting in the -X direction and net work was being extracted from the flow, consistent with an MGD generator. Of all the cases tested, only those with $k = 2.0$ established a strong enough electric field to cause a net Lorentz force in the +X direction and deposit positive work into the flow. Because of this, only these latter cases were subjected to the complete performance analysis presented here.

Even more so than with the combustor-based MGD generators, it was helpful to look at how the accelerators affected the flow properties. In fact, as seen in the temperature profiles of Figure 6.12(a), the primary effect of all the MGD accelerators was made clearly evident. In all instances, the accelerators increased the static temperature in the interaction region as would be expected. Even at $Q = 1$, the effect was significant with the peak temperature change relative to baseline being 120K and 250K for the 2-Elec and 4-Elec cases, respectively. However, at $Q = 5$ the heating was extreme with peak differences of 800K and 1370K respectively. This last result was 50% greater than the same effect produced by the upstream generator and 65%

greater than the temperature rise due to the fuel injection shock. From this, it was concluded that a significant portion of the energy put back into the flow was in the form of random thermal energy. To verify this, calculations were made to determine the breakdown of the total interaction between Joulean dissipation and useful work. Where typical combustor-based generator results showed useful work extraction made up 67%–75% of the total interaction, accelerators only achieved about 50%–55%, or about half of the entire input was dissipated as heat. Because the electric field is acting to produce a net current flow opposite that induced by the plasma motion, significantly larger overall energy inputs are need to induce a significant useful work contribution. As was seen here, as the energy input increased to accomplish this, the thermal heating likewise increased in greater proportion. This was obviously not a tenable solution, as temperature limits in a real engine would have been easily exceeded well before significant acceleration would be achieved. In fact, examination of the average velocity components (as shown in Figure 6.12(b)) aptly demonstrated this effect. Even with the large interaction of the 4-Elec, $Q = 5$ case the maximum acceleration only achieved a Δu of 85m/s. When accompanied by the heating, the net effect was a decrease in the Mach number entering the expansion nozzle as seen in Figure 6.12(c). For $Q = 5$, this decrease amounted to approximately 0.3.

From the flow field results for the MGD accelerators, it was expected that the performance of the overall MGD bypass configurations tested would be less than what would be needed to account for the increased drag due to the upstream power generation. In fact, the control volume analysis clearly demonstrated that for the configurations tested, none of the bypass systems could achieve an overall engine thrust. Bearing in mind that even the baseline engine suffered a net drag penalty due to the less than optimal combustor and expansion system geometry, it was more useful to once again look at the total axial force relative to the baseline case. As can be seen in Figure 6.13(a), all of the MGD bypass engines demonstrated approximately 33% more net drag than the baseline engine. In effect, the significant drag penalty induced by the MGD generator was not recovered by reinserting electrical energy
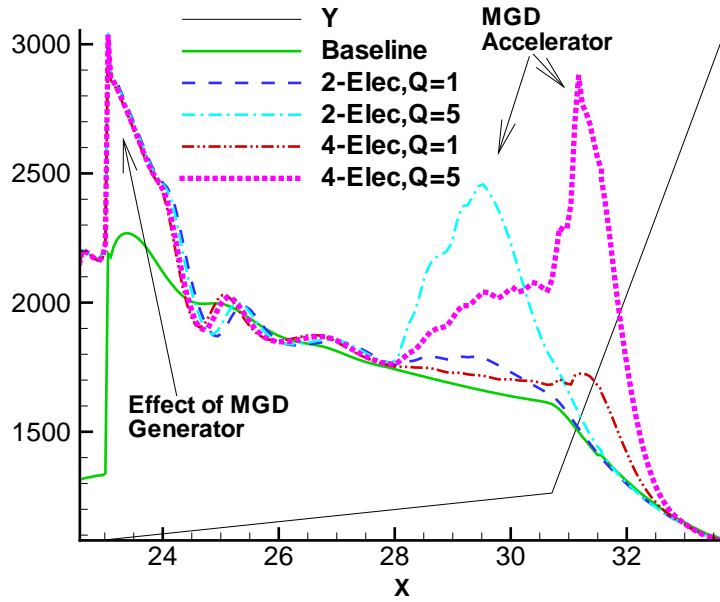
(a) Temperature (K)
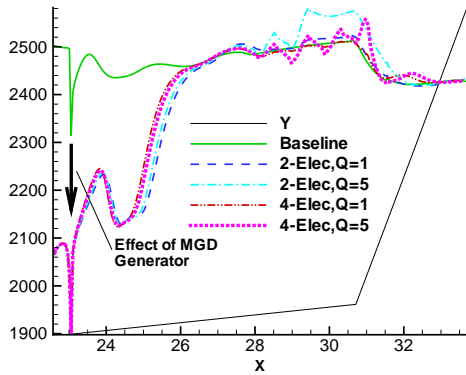
(b) u-Velocity (m/s)
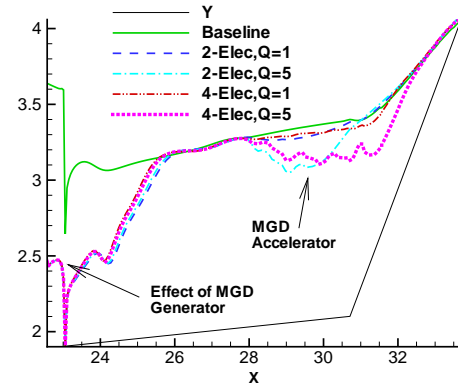
(c) Mach Number

Figure 6.12:   Comparison of Selected Cross-Sectional Averaged Flow Properties for $k = 2.0$ MGD Acceleration with Specified Electrodes.

into the flow. To make matters worse, because the MGD accelerators performed so inefficiently with respect to producing useful work, substantially more energy had to be put into the flow than had been taken out of the generator to produce the results seen. From Figure 6.13(b), it was seen that none of the MGD bypass systems as a whole had a net margin of positive electrical power production. Even the relatively minor interactions from the $Q = 1$ accelerators produced system-level power deficits of 8MW–10MW, which were insignificant compared to the 150MW-class deficits of the $Q = 5$ systems.

In light of these results, it was easy to conclude that for the configurations tested, MGD acceleration was ineffective for improving the performance of this scramjet. Furthermore, when taken as an overall system, the energy bypass concept was unable under any circumstance to be self-powered. While these conclusions must be kept in the context of the segmented Faraday electrodes tested, it is felt that the physics of MGD flow acceleration will in most configurations result in a disproportionate amount of electrical energy being required to produce useful flow work and acceleration. In addition, this work will always be accompanied by a significantly greater fraction of the total energy input being dissipated as heat as compared to a similarly sized MGD generator. However, it is recommended that any future work in the area of MGD acceleration and energy bypass be directed towards the examination of alternative electrode configurations (e.g. Hall current electrodes or diagonally offset Faraday electrodes).

(a) Axial Force (N)
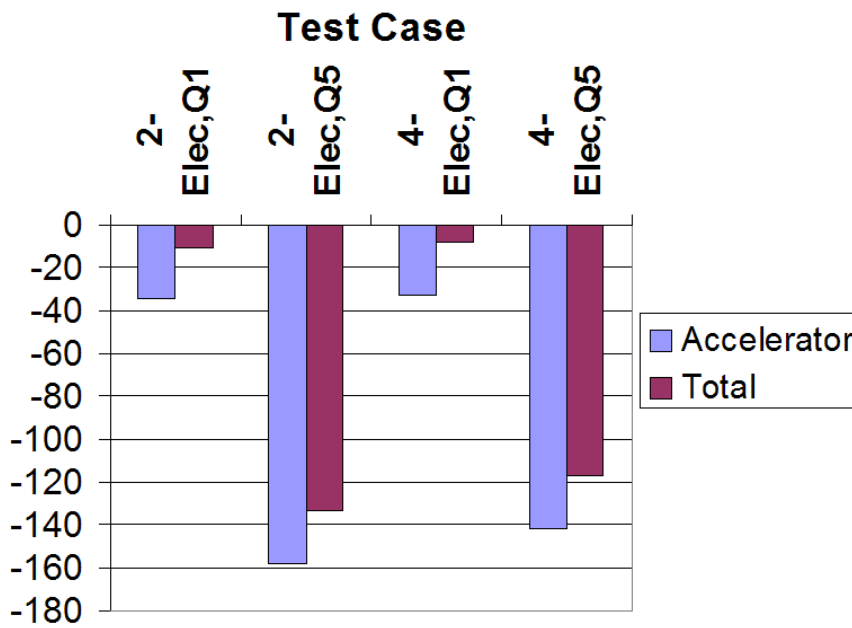
(b) Net Electrical Power in MW (Negative Values Denote Consumption)

Figure 6.13: Comparison of Component and Total Axial Force and Net Electric Power Balance for MGD Energy Bypass Scramjets Using Specified Electrodes.

6.4 Summary of Results, Conclusions and Recommendations Regarding MGD Power Generation and Energy Bypass

Regarding MGD power generation in general, and in particular, generation upstram of the combustor, MW-class electrical power generation was achieved, even for the relatively small interaction parameter of $Q = 1$. However, this positive result came with performance penalties in terms of a drag increase with respect to baseline that varied anywhere from 10% to nearly double the baseline inlet value. This added drag, as well as dissipation induced heating, reduced most of the overall inlet performance measures with respect to the no-MGD baseline. From this, it was concluded that if the primary purpose for MGD power generation is to supply onboard electrical components, smaller generators with lower interaction parameters (i.e. lower system power requirements) should be considered. Moreover, it is more important to focus the interaction region in the core flow, where the useful work was a greater proportion of the overall interaction. However, if the goal is to maximize the work extraction with the goal of bypassing it directly to the expansion system, then the interaction parameter and plasma volume should be maximized. Finally, comparing combustor-based MGD power generation to its isolator-based counterpart revealed that the combustor-based generators performed moderately better, in spite of localized pressure increases in the vicinity of the electrodes which indicated the presence of small shock waves.

During the course of examining the Faraday electrode configurations, it was found that the research code's method of specifying electric potential required making some assumptions regarding the average local flow velocity. The difficulty with this approach is that $\vec{V}$ is never constant and thus there existed electrode configurations with substantial areas of reversed current flow. The net effect was in many configurations MGD generators actually acted as accelerators and vice versa. In light of this fact, it is recommended that future work focus on more accurate methods of modelling the electrode potentials, including consideration of the modelling of the external electric circuit in its entirety.

Finally, with respect to MGD acceleration and specifically the MGD energy bypass concept, it was easy to conclude that for the configurations tested, MGD acceleration was ineffective for improving the performance of this scramjet. Furthermore, when taken as an overall system, the energy bypass concept was unable under any circumstance to be self-powered. Although this research focused on the segmented Faraday electrode configuration, the physics of MGD flow acceleration will in most configurations result in a disproportionate amount of electrical energy being required to produce useful flow work and acceleration. In addition, this work will always be accompanied by a significantly greater fraction of the total energy input being dissipated as heat as compared to a similarly sized MGD generator. However, it is recommended that any future work in the area of MGD acceleration and energy bypass be directed towards the examination of alternative electrode configurations (e.g. Hall current electrodes or diagonally offset Faraday electrodes).

VII. Summary, Conclusions, and Recommendations

7.1 Summary

Prior to this work, the analysis of electromagnetic (EM) flow control through the application of magnetogasdynamics (MGD) relied upon simplified analytical treatments and reduced dimensional numerical studies. These key limitations included unrealistic flowpath geometries, calorically perfect gases, and inviscid, 2D flow solvers. As a consequence, not all of the pertinent flow physics were included and thus the conclusions reached were limited in applicability. The effort concluded here contributes directly to the advancement of this research field by removing these limitations, applying the first comprehensive three-dimensional analysis of EM flow control to a flight-sized, scramjet engine.

The starting point for this research was a CFD code developed by the Air Force Research Laboratory (AFRL) to model the full, three-dimensional set of coupled Navier-Stokes and Maxwell's equations [20]. Since the Mach 10 scramjet flow under consideration can be considered a collision-dominated, weakly ionized plasma, the typical MGD assumptions hold. The key assumption in this case was low electrical conductivity and that the magnitude of the applied magnetic field was high. This condition defines the low magnetic Reynold's number regime, which allowed the Lorentz Force and EM interaction to be coupled to the Navier-Stokes' equations as simple source terms. This coupling allows the use of conventional CFD techniques could be employed. For this research, the Roe flux difference splitting scheme with the vanLeer harmonic limiter and central differencing were used for spatial discretization, while an implicit Beam-Warming method was used for temporal discretization. To account for turbulent flow, the widely used $k - \epsilon$ model, modified for use with MGD, was included.

Regarding the CFD modelling of the EM fields, all of the research conducted specified the magnetic flux density, $\vec{B}$, at all points and assumed it was invariant in both time and space. The plasma conductivity, σ, was time invariant as well, with a scalar value whose spatial growth and decay was held constant by a three-

dimensional Gaussian distribution. Two methods of calculating the electric field, $\vec{E}$, were employed. The first approach was the same as for $\vec{B}$, wherein $\vec{E}$ was initialized and then held invariant. This approach was simpler to implement and had a distinct advantage in lower computational expense. However, the solutions obtained demonstrated that it was likely to produce less realistic results. The second approach used a higher fidelity approach, specifying the locations and electric potential for wall-based electrodes. A Poisson solver was used with this approach to enforce current continuity and obtain the $\vec{E}$ field. The advantage of this method was that it created an $\vec{E}$ field that was coupled to the flow, such that as the EM interaction altered the flow, the flow would simultaneously change the $\vec{E}$ field until reaching equilibrium. This results in a more realistic capturing of the flow physics, but at a significant increase in computational time. Where the first approach could converge the typical 750,000 point domain in less than a week using a Cray X1 supercomputer, it was common for the latter approach to take 2 weeks to converge the same problem. More importantly, accurately capturing the physics at electrode-insulator boundaries presented problems with some MGD device configurations, as did difficulties in applying optimized numerical filtering.

As a final note, all of the electrode-based models tested used a segmented Faraday configuration where paired electrodes of opposite potential were placed on opposing wall boundaries. Because of this configuration, Hall current effects were not included in this research.

Before EM flow control was considered, the key physical processes common to scramjet engines were explored and incorporated into the development of a first-of-its-kind open source scramjet geometry. First, this was done through the development of a quasi-1D computational design tool. Verification of this tool was performed by comparison with similar computational models followed by application to the simplified AFRL scramjet geometry given in Reference [21]. This computational code was then applied to appropriately size the engine to support the requirements of the Military Spaceplane concept [82], a proposed Air Force program for a hypersonic vehicle with

global reach. Once this was accomplished, various analytical methods and experimental data were taken from literature and applied to convert the quasi-1D design to a 3D geometry. Finally, an initial computational run of the engine was completed and analyzed. Based on this analysis, which included a grid convergence study, improvements to the geometry were made in order to establish the baseline performance model. This baseline model would be the starting point for the all of the remaining research.

Two significant additions to the existing code were made to support the goals of this research. The first was the creation of a post-CFD analysis tool that allowed for a dimensional analysis of the EM impacts to the system and its performance. Key to this addition was the inclusion of an electron beam model and routines to perform cross-sectional and cell-based averages of flow and EM properties. These results were then cast into a form suitable for taking a control volume approach that was used to determine overall performance values, e.g. forces, heat transfer, and total pressure ratios.

The second major addition was the development and verification of a finite rate thermochemistry model. The primary purpose for undertaking this portion of the research effort was because stable, efficient combustion has traditionally been one of the greatest challenges to achieving scramjet propulsion. A portion of this research broke new ground in demonstrating the first coupling of a finite rate chemistry and MGD solver for scramjet applications. In addition, the coupling algorithm was purposefully generalized such that it could be used or turned off as needed, allowing computational expense to be balanced against a particular application's requirements. The successful implementation of this computational tool, overcame two significant shortfalls in the AFRL research code: (1) the major assumption the gas was non-reactive air, and (2) chemical combustion could only be represented by a simple volumetric heating rate source term in the energy equation.

Culminating the research effort, a detailed computational analysis of this engine in the context of both localized MGD flow control applications and the MGD energy bypass system were explored. Regarding local EM flow control, this research explored the possibility of mitigating a region of separated flow within the internal inlet and increasing the average pressure entering the combustor. Two MGD concepts were considered to address this issue: increasing pressure in the cowl shoulder region to better match that of the reflected shock, or increasing flow momentum in the boundary layer to overcome the adverse pressure gradient. A parametric study tested these concepts by varying the spatial distribution of the plasma region, the load factor, k, and the interaction parameter, Q. In summary, localized MGD flow control was marginally successful in raising the average pressure entering the combustor, and even more successful at reducing overall inlet drag.

The system-level MGD research was tested to a level of computational fidelity never before attempted. Three distinct applications were investigated: (1) stand-alone MGD power generation performed upstream of the combustor, (2) stand-alone combustor-based MGD power generation, and (3) a full MGD energy bypass system. Regarding MGD power generation in general, and in particular, generation upstram of the combustor, MW-class electrical power generation was achieved, even for the relatively small interaction parameter of $Q = 1$. However, this positive result came with performance penalties in terms of a drag increase with respect to baseline that varied anywhere from 10% to nearly double the baseline inlet value. This added drag, as well as dissipation induced heating, reduced most of the overall inlet performance measures with respect to the no-MGD baseline. Comparing combustor-based MGD power generation to its isolator-based counterpart revealed that the combustor-based generators performed moderately better, in spite of localized pressure increases in the vicinity of the electrodes which indicated the presence of small shock waves.

With respect to MGD acceleration and specifically the MGD energy bypass concept, none of the configurations tested improved the performance of this scramjet with respect to net axial force. Rather, as compared to the baseline engine all of the

bypass engines experienced a net drag increase of approximately 33%. Furthermore, none of the bypass engines could be considered self-powered. In every case, the power produced by the most powerful generator tested was insufficient to both ionize the flow and supply the power required by the MGD accelerators. While these conclusions must be kept in the context of the segmented Faraday electrodes tested, it is felt that the physics of MGD flow acceleration will in most configurations result in a disproportionate amount of electrical energy being consumed to produce useful flow work and acceleration. In addition, the flow work will always be accompanied by a significantly greater fraction of the total energy input being dissipated as heat as compared to a similarly sized MGD generator.

7.2   Conclusions

Based upon this research effort, the following conclusions were reached:

1. *Coupling the thermochemistry with the fluid dynamics captured phenomena unseen by either model alone, improving the overall accuracy of the simulation.* Using this approach, results from the model problem exceeded expectations, matching the predicted ignition point and differing by only 0.5% with respect to the well-accepted STANJAN software.

2. *The loosely coupled approach to incorporate finite rate chemistry was very successful with respect to modelling supersonic combustion flow problems and is recommended over the existing polynomial gamma and heat source term approaches for these problems.* With regard to the actual scramjet modelling done, the inclusion of combustion chemistry resulted in the most accurate representation of a real engine.

3. *As a consequence, this successful addition to the AFRL computational electromagnetics code provides the only open-source model of fuel injection, mixing and combustion for MGD flow control applications.*

4. *The placement of the EM interaction region, and in particular the electrodes, is critical to successful exploitation of this technology.* The extent of the flow-EM interaction is only fully realized when the inherent complexity of the 3D, viscous flow physics is taken into account. 1D or 2D, inviscid solutions by themselves are inadequate for accurately capturing the impacts to performance in the scramjet engine. As an example, placement of the EM-interaction region near the wall was the most important factor in determining the wall heat transfer, and targeting the conductivity to this region was a relatively efficient method of limiting drag increases.

5. *MGD electrical power generation for the purpose of powering the vehicle's on-board electrical systems, to include the ionization source and any electromagnet requirements, is certainly feasible with a flight-sized engine.* This assumes of course that the weight and complexity of the magnet and associated ionization and control system does not prove prohibitive. For many of the MGD generator cases, MW-class electrical power generation was achieved, verifying the results of previous research. However, tying back to the previous conclusion, electrode placement was critical to successful power generation and there was a large difference in performance depending on the k and Q used.

6. *The use of an MGD accelerator to locally increase flow momentum was an effective approach to improve flow into the isolator of this scramjet model.* Although it only slightly increased the flow pressure going into the isolator, MGD acceleration, particularly for Case 2B, was able to efficiently reduce the net inlet drag. It did this while minimizing the increase in heat transfer and decrease in overall efficiency measures. This was due primarily to increasing the flow momentum as it passed through the sidewall expansion into the inlet throat.

7. *Combustor-based MGD power generation was superior to the inlet-based approach with respect to power density and overall engine efficiency.* For electrical power generation, then, an approach similar to that of ground-based, combustion-fired MGD generators should be pursued.

8. *For the electrode configurations tested, MGD acceleration was ineffective for improving the performance of this scramjet. Furthermore, when taken as an overall system, the energy bypass concept was unable under any circumstance to be self-powered.* MGD acceleration was shown to be ineffective in improving overall performance, with all of the bypass engines having approximately 33% more drag than baseline and none of them achieving a self-powered state. In light of this, it is difficult to conceive of a viable MGD energy bypass system.

7.3   Recommendations for Future Research

1. *It is recommended that this improved computational tool should be used to improve upon the current geometry and establish an optimized baseline upon which to further test flow control applications.* Several problems with the geometry were identified that could be traced back to the quasi-1D design iteration. The deficiencies with the greatest performance impact were the lack of a combustor flameholder and fuel-air mixing cavity as well as an oversimplified and over-expanded expansion nozzle. The structured grid used by the computational method precluded the addition of the complicated combustor geometry needed. Finally, these combustion and expansion components are the most difficult parts of the flow path to optimize and would require several more design iterations to significantly improve.

2. *Consideration should be given to adding species diffusion, thus extending applicability to the subsonic regime. In addition, higher fidelity models of viscosity and thermal conductivity could be incorporated.*

3. Future work in the area of MGD acceleration and energy bypass should be directed towards *the examination of alternative electrode configurations* (e.g. Hall current electrodes or diagonally offset Faraday electrodes).

4. In this regard, *a more detailed method of modelling the electrode potential should be undertaken that better accounts for the electrode-insulator boundary condition.*

This is necessary to eliminate detrimental effects such as near wall reversal of the $\vec{E}$ field that was seen with some electrode configurations.

5. In conjunction with the two prior recommendations, *the optimum distance off the wall to target the electron beam ionization should be investigated further.*

6. Finally, *long term research in this area should include modelling of the external electric circuit to understand the dynamic response of these flow control systems.* This modelling should include, as a minimum, a detailed analysis of the ionization and magnetic field generator power requirements as well as the load presented by the vehicle's overall electrical system.

Bibliography

1. *Stopping Powers for Electrons and Positrons*. Technical report, International Commission on Radiation Units and Measurements, 1984.

2. Abdel-Salam, T.M. and R.A. Carson. "Three-Dimensional Numerical Study of a Dual-Mode Scramjet Combustor". *37th AIAA Thermophysics Conference*, 1–10. AIAA, 2004.

3. Ault, D.A. and D.M. Van Wie. "Comparison of Experimental Results and Computational Analysis for the External Flowfield of a Scramjet Inlet at Mach 10 and 14". *AIAA Fourth International Aerospace Planes Conference*. AIAA, 1992.

4. Baurle, R.A. and D.R. Eklund. "Analysis of Dual-Mode Hydrocarbon Scramjet Operation at Mach 4 - 6.5". *Journal of Propulsion and Power*, 18(5):990–1002, 2002.

5. Ben-Yakar, A. and R.K. Hanson. "Cavity Flame-Holders for Ignition and Flame Stabilization in Scramjets: An Overview". *Journal of Propulsion and Power*, 17(4):869–877, 2001.

6. Berry, S.A. and A.H. Auslender. "Hypersonic Boundary-Layer Trip Development for Hyper-X". *Journal of Spacecraft and Rockets*, 38(6):853–863, 2001.

7. Bityurin, V.A., A.N. Bocharov, and J.T. Lineberry. "Results of Experiments on MHD Hypersonic Flow Control". *35th AIAA Plasmadynamics and Lasers Conference*, 1–15. AIAA, 2004.

8. Brichkin, D.I., A.L. Kuranov, and E.G. Sheikin. "The Potentialities of MHD Control for Improving Scramjet Performance". 1–11. AIAA 1999-4969.

9. Bruno, C. and P.A. Czysz. *An Electro-Magneti-Chemical Hypersonic Propulsion System*. Technical report, AIAA, 1998.

10. Burakhanov, B.M., A.P. Likhachev, S.A. Medin, V.A. Novikov, V.I. Okunev, V.Y. Rickman, and V.A. Zeigarnik. "Advancement of Scramjet Magnetohydrodynamic Concept". *Journal of Propulsion and Power*, 17(6):1247–1252, 2001.

11. Cockrell, C.E.J., W.C. Engelund, R.D. Bittner, T.N. Jentink, A.D. Dilley, and A. Frendi. "Integrated Aeropropulsive Computational Fluid Dynamics Methodology for the Hyper-X Flight Experiment". *Journal of Spacecraft and Rockets*, 38(6):836–843, 2001.

12. Curran, E.T. "Scramjet Engines: The First Forty Years". *Journal of Propulsion and Power*, 17(6):1138–1148, 2001.

13. Curran, E.T. and S.N.B. Murthy. *Scramjet Propulsion*, volume 189 of *Progress in Astronautics and Aeronautics*. AIAA, 2000.

14. D'Ambrosio, D. and D. Giordano. "Electromagnetic Fluid Dynamics for Aerospace Applications. Part I: Classification and Critical Review of Physical Models". *35th AIAA Plasmadynamics and Lasers Conference*, 1–14. AIAA, 2004.

15. Davis, D.L. "Numerical Analysis of Two and Three Dimensional Recessed Flameholders for Scramjet Applications", 1996.

16. Dornheim, M.A. "A Breath of Fast Air". www.aviationnow.com, 2004.

17. Earp, B.E. *Magnetogasdynamic Flow Control of a Mach Reflection*. Master's thesis, Air Force Institute of Technology, 2004.

18. Evans, J.S. and Jr. Schexnayder, C.J. "Influence of Chemical Kinetics and Unmixedness on Burning in Supersonic Hydrogen Flames". *AIAA Journal*, 18(2):188–193, 1980.

19. Fisher, S.A. "Three-Dimensional Flow Effects in a Two-Dimensional Supersonic Air Intake". *Journal of Propulsion and Power*, 2(6):546–551, 1986.

20. Gaitonde, D.V. "Development of a Solver for 3-D Non-Ideal Magnetogasdynamics". *30th AIAA Plasmadynamics and Lasers Conference*, 1–15. AIAA, 1999.

21. Gaitonde, D.V. "Three-Dimensional Flow-Through Scramjet Simulation with MGD Energy Bypass". *41st AIAA Aerospace Sciences Meeting and Exhibit*, 1–19. AIAA, 2003.

22. Gaitonde, D.V. and J. Poggie. "An Implicit Technique for 3-D Turbulent MGD with the Generalized Ohm's Law". *32nd AIAA Plasmadynamics and Lasers Conference*, 1–17. AIAA, 2001.

23. Gaitonde, D.V. and J. Poggie. "Elements of a Numerical Procedure for 3-D MGD Flow Control Analysis". *40th AIAA Aerospace Sciences Meeting and Exhibit*, 1–17. AIAA, 2002.

24. Goyne, C.P., J.C. McDaniel, T.M. Quagliaroli, R.H. Krauss, and S.W. Day. "Dual-Mode Combustion of Hydrogen in a Mach 5, Continuous-Flow Facility". *Journal of Propulsion and Power*, 17(6):1313–1318, 2001.

25. Heiser, W.H. and D.T. Pratt. *Hypersonic Airbreathing Propulsion*. AIAA Education Series. AIAA, 1994.

26. Hoffman, K.A. and S.T. Chiang. *Computational Fluid Dynamics Volume II, 4th Edition*, chapter 16. Engineering Education System, 2000.

27. Holland, S.D. "A Computational and Experimental Investigation of a Three-Dimensional Hypersonic Scramjet Inlet Flow Field", 1991.

28. Holland, S.D. and J.N. Perkins. "Contraction Ratio Effects in a Generic Three-Dimensional Sidewall Compression Scramjet Inlet: A Computational and Experimental Investigation". *AIAA 22nd Fluid Dynamics, Plasma Dynamics, and Lasers Conference*, 1–18. AIAA, 1991.

29. Holland, S.D., W.C. Woods, and W.C. Engelund. "Hyper-X Research Vehicle Experimental Aerodynamics Test Program Overview". *Journal of Spacecraft and Rockets*, 38(6):828–835, 2001.

30. Hughes, W.F. and F.J. Young. *The Electromagnetodynamics of Fluids.*

31. Kanury, M. A. *Introduction to Combustion Phenomena*, 139. Gordon and Breach Publishers, 1995.

32. Kim, C.K., S.T. Yu, and Z.C. Zhang. "Cavity Flow in Scramjet Engine by Space-Time Conservation and Solution Element Method". *AIAA Journal*, 42(5):912–919, 2004.

33. Kuranov, A.L., V.V. Kuchinsky, and E.G. Sheikin. "Scramjet with MHD Control under "AJAX" Concept. Requirements for MHD Systems." *32nd AIAA Plasmadynamics and Lasers Conference*, 1–11. AIAA, 2001.

34. Kuranov, A.L. and E.G. Sheikin. "MHD Control on Hypersonic Aircraft under "AJAX" Concept. Possibilities of MHD Generator". *40th AIAA Aerospace Sciences Meeting and Exhibit*, 1–11. AIAA 2002-0490.

35. Kuranov, A.L. and E.G. Sheikin. "The Potential of MHD Control for Improving Scramjet Performance". *30th AIAA Plasmadynamics and Lasers Conference*, 1–9. AIAA 1999-3535.

36. Kuranov, A.L. and E.G. Sheikin. "Magnetohydrodynamic Control on Hypersonic Aircraft Under "Ajax" Concept". *AIAA Journal of Spacecraft and Rockets*, 40(2):174–182, 2003.

37. Lindsey, M.F. and R.J. McMullan. "Computational Study of MGD Flow Control on a Flight-Scale Scramjet". AIAA 2006-0371, 2006.

38. Lindsey, M.F., R.J. McMullan, and D.V. Gaitonde. "A Computational Thermochemistry Model for Scramjets with Electromagnetic Flow Control". AIAA 2005-3222, 2005.

39. Lindsey, M.F., R.J. McMullan, and D.V. Gaitonde. "Development of a Realistic 3-D Scramjet Flowpath for MGD Energy Bypass". AIAA 2005-1178, 2005.

40. Linstrom, P.J. and W.G. Mallard (editors). *NIST Chemistry WebBook, NIST Standard Reference Database Number 69.* National Institute of Standards and Technology, Gaithersburg MD, 20899, 1995.

41. Liston, G. "Quasi-1D Scramjet Code Results Comparison and Discussion", 2004. Personal correspondence with AFRL/PRA researchers.

42. Litchford, R.J., J.W. Cole, V.A. Bityurin, and J.T. Lineberry. *Thermodynamic Cycle Analysis of Magnetohydrodynamic-Bypass Hypersonic Airbreathing Engines.* Technical report, NASA TP-2000-210387, 2000.

43. Litchford, R.J., J.W. Cole, and J.T. Lineberry. "Thermodynamic Cycle Analysis of Magnetohydrodynamic-Bypass Hypersonic Airbreathing Engines". *Journal of Propulsion and Power*, 17(2):477–480, 2000.

44. Macheret, S.O., R.B. Miles, and G.L. Nelson. "Feasibility Study of a Hybrid MHD/Radiatively Driven Facility for Hypersonic Ground Testing". AIAA 1997-2429, 1997.

45. Macheret, S.O., M.N. Shneider, and R.B. Miles. "Potential Performance of Supersonic MHD Power Generators". *39th AIAA Aerospace Sciences Meeting and Exhibit*, 1–24. AIAA 2001-0795.

46. Macheret, S.O., M.N. Shneider, and R.B. Miles. "Energy-Efficient Generation of Nonequilibrium Plasmas and Their Applications to Hypersonic MHD Systems". AIAA 2001-2880, 2001.

47. Macheret, S.O., M.N. Shneider, and R.B. Miles. "Magnetohydrodynamic Control of Hypersonic Flows and Scramjet Inlets Using Electron Beam Ionization". *AIAA Journal*, 40(1):74–81, 2002.

48. Macheret, S.O., M.N. Shneider, and R.B. Miles. "Modeling of Air Plasma Generation by Repetitive High-Voltage Nanosecond Pulses". *IEEE Transactions of Plasma Science*, 30(3):1301–1314, 2002.

49. Macheret, S.O., M.N. Shneider, and R.B. Miles. *Scramjet Inlet Control by Off-Body Energy Addition: A Virtual Cowl*. 2002.

50. Macheret, S.O., M.N. Shneider, D.M. Van Wie, and R.B. Miles. "MHD Power Generation in Scramjet Engines in Conjunction with Inlet Control". *42nd AIAA Aerospace Sciences Meeting and Exhibit*, 1–24. 2004.

51. Mahoney, J. *Inlets for Supersonic Missiles*. AIAA Education Series. AIAA, 1990.

52. Mani, M., R.H. Bush, and P. Vogel. "Implicit Equilibrium and Finite-Rate Chemistry Models for High Speed Flow Applications". AIAA 1991-3299, 1991.

53. McEldowney, B., R. Meyer, N. Chintala, and A.I. V. "Measurements of Electrical Parameters of a Supersonic Non-Equilibrium MGD Channel". *34th AIAA Plasmadynamics and Lasers Conference*, 1–14. AIAA, 2003.

54. Mehta, U.B., D.W. Bogdanoff, and C. Park. *A Perspective on a Combined Magneto-Hydrodynamic-Scramjet Engine*. Technical report, NASA, 2001.

55. Meyer, R., B. McEldowney, N. Chintala, P. Palm, and I.V. Adamovich. "Experimental Studies of Plasma Assisted Ignition and MGD Supersonic Flow Control". *41st AIAA Aerospace Sciences Meeting and Exhibit*. AIAA, 2003.

56. Mitani, T., N. Chinzei, and K. Takeshi. "Reaction and Mixing-Controlled Combustion in Scramjet Engines". *Journal of Propulsion and Power*, 17(2):308–314, 2001.

57. NASA. "Guinness World Records Recognizes NASA X-43A Speed Record". NASA Dryden News Releases, 2004.

58. NASA. "Faster Than a Speeding Bullet: Guinness Recognizes NASA Scramjet". NASA News Release: 05-156, 2005.

59. Nishihara, M., R. Meyer, M. Cundy, W.R. Lempert, and I.V. Adamovich. "Development and Operation of a Supersonic Nonequilibrium MHD Channel". *35th AIAA Plasmadynamics and Lasers Conference*, 1–19. AIAA, 2004.

60. Park, C., D.W. Bogdanoff, and U.B. Mehta. "Theoretical Performance of Frictionless Magnetohydrodynamic-Bypass Scramjets". *Journal of Propulsion and Power*, 17(3):591–598, 2001.

61. Poggie, J. and D.V. Gaitonde. "Magnetic Control of Hypersonic Blunt Body Flow". *38th AIAA Aerospace Sciences Meeting and Exhibit*, 1–15. AIAA, 2000.

62. Poggie, J. and D.V. Gaitonde. "Computational Studies of Magnetic Control in Hypersonic Flow". *39th AIAA Aerospace Sciences Meeting and Exhibit*, 1–12. AIAA, 2001.

63. Poggie, J. and D.V. Gaitonde. "Magnetic control of flow past a blunt body: Numerical validation and exploration". *Physics of Fluids*, 14(5):1720–1731, 2002.

64. Powell, O.A., J.T. Edwards, R.B. Norris, and K.E. Numbers. "Development of Hydrocarbon-Fueled Scramjet Engines: The Hypersonic Technology (HyTech) Program". *Journal of Propulsion and Power*, 17(6):1170–1176, 2001.

65. Reinartz, B.U., J. van Keuk, T. Coratekin, and J. Ballmann. "Computation of Wall Heat Fluxes in Hypersonic Inlet Flows". *40th AIAA Aerospace Sciences Meeting and Exhibit*, 1–10. 2002.

66. Reynolds, W.C. "STANJAN Chemical Equilibrium Solver, v3.91 IBM-PC". Stanford University, 1987.

67. Riggins, D.W. "Analysis of the Magnetohydrodynamic Energy Bypass Engine for High-Speed Airbreathing Propulsion". *AIAA Journal of Propulsion and Power*, 20(5):779–792, 2004.

68. Rogers, R.C. and W. Chinitz. "On the Use of a Global Hydrogen-Air Combustion Model in the Calculation of Turbulent Reacting Flows". AIAA 1982-0112, 1982.

69. Rogers, R.C. and Jr. Schexnayder, C.J. *Chemical Kinetic Analysis of Hydrogen-Air Ignition and Reaction Times*. Technical report, National Aeronautics and Space Administration, 1981.

70. Rosa, R.J. *Magnetohydrodynamic Energy Conversion*. McGraw-Hill, 1968.

71. Sato, H. "The Hall Effect in the Viscous Flow of Ionized Gas between Parallel Plates under Transverse Magnetic Field". *J. Phys. Soc. of Japan*, 16(7):1427–1433, July 1961.

72. Schneider, S.P. and C. Skoch. "Streamwise-Vortex Instability and Transition on the Hyper-2000 Scramjet Forebody". *22nd AIAA Ground Testing Conference*, 1–16. AIAA, 2003.

73. Shneider, M.N. and S.O. Macheret. "Modeling of Plasma Virtual Shape Control of Ram/Scramjet Inlet and Isolator". *35th AIAA Plasmadynamics and Lasers Conference*, 1–19. AIAA 2004-2662, 2004.

74. Shneider, M.N. and S.O. Macheret. "Hypersonic Aerodynamic Control and Thrust Vectoring by Nonequilibrium Cold-Air MHD Devices". AIAA 2005-0979, 2005.

75. Sutton, G.W. and A. Sherman. *Engineering Magnetohydrodynamics*. McGraw-Hill, 1965.

76. Tannehill, J.C., D.A. Anderson, and R.H. Pletcher. *Computational Fluid Mechanics and Heat Transfer*. Taylor and Francis, 2 edition, 1997.

77. Townend, L.H. "Domain of the Scramjet". *Journal of Propulsion and Power*, 17(6):1205–1213, 1991.

78. Turchak, A., A. Kuranov, and A. Korabelnikov. "Hypersonic Technologies of the "AJAX" Concept". AIAA 2002-5184, 2002.

79. Uenishi, K., R.C. Rogers, and G. Northam. "Three Dimensional Computations of Transverse Hydrogen Jet Combustion in a Supersonic Airstream". AIAA 1987-0089, 1987.

80. Van Wie, D.M. and D.A. Ault. "Internal Flowfield Characteristics of a Scramjet Inlet at Mach 10". *Journal of Propulsion and Power*, 12(1):158–164, 1996.

81. Vassberg, J.C., M.A. DeHaan, and A.J. Sclafani. "Grid Generation Requirements for Accurate Drag Predictions Based on OVERFLOW Calculations". *16th AIAA Computational Fluid Dynamics Conference*, 1–27. AIAA, 2003.

82. Vick, C.P., S.D. Berman, and C. Lindborg. *Military Spaceplane, X-40 Space Maneuver Vehicle, Integrated Tech Testbed*. Federation of American Scientists, 1999.

83. White, F.M. *Fluid Mechanics*, chapter 3. McGraw-Hill, 2 edition, 1986.

84. White, F.M. *Viscous Fluid Flow*, 29. McGraw-Hill, 2 edition, 1991.

Vita

Major Martin F. Lindsey graduated from Georgetown High School in Georgetown, Texas, in 1989. He received his Bachelor of Science Degree in Aerospace Engineering, specializing in astronautics, from the University of Texas at Austin in 1993. Immediately thereafter, he reported to the United States Air Force Officer Training School, Lackland Air Force Base, Texas, from which he graduated as a Distinguished Military Graduate and was commissioned as a Second Lieutenant in September 1993.

Maj Lindsey served in several mission support and operational specialties while simultaneously pursuing professional education. Beginning with a tour as a Minuteman III ICBM maintenance officer in Minot, North Dakota, he served in various leadership positions including being the Maintenance Supervisor for the 742d Missile Squadron and culminating in the Chief of the Maintenance Operations Center. In this capacity, he was responsible for directing real-time maintenance scheduling, prioritization and operations for 150 ICBMs and 15 launch control centers. During this tour he began taking coursework towards his Masters of Aerospace Engineering from Auburn University, Alabama. At the same time, he completed the Federal Aviation Administration requirements to be granted Commercial, Instrument, and Certificated Flight Instructor certificates.

In 1998, he was reassigned to Vandenberg AFB, California, for training as a space and missile operator. Upon graduation as the Top Graduate and recipient of the Air Education and Training Command Commander's Trophy, he was assigned to serve as a space launch operator at Cape Canaveral Air Force Station, Florida. During four years at the Cape, Maj Lindsey served in several capacities for a variety of organizations and launch platforms. As the Atlas Operations Flight Commander in the 3rd Space Launch Squadron, he was responsible for all Air Force launch base operations for the Atlas II/III launch system. Then, he was part of the initial Air Force team to bring the Delta IV Evolved Expendable Launch Vehicle to operational capability with a successful first flight in November 2002. It was during this assignment,

that Maj Lindsey completed his Masters of Aerospace Engineering and then went on to further earn a Masters of Science in Space Systems from the Florida Institute of Technology.

At the end of 2002, he was assigned to the Air Force Institute of Technology at Wright-Patterson AFB, Ohio, where he was enrolled as a student in the aeronautical engineering doctoral program. Upon graduation he will be assigned to the Computational Aerodynamics Center at the Air Force Research Laboratories, Aeronautical Vehicles Directorate, also at Wright-Patterson AFB.

Permanent address: 2950 Hobson Way
Air Force Institute of Technology
Wright-Patterson AFB, OH 45433

1. REPORT DATE *(DD–MM–YYYY)*	2. REPORT TYPE	3. DATES COVERED *(From — To)*
23–03–2006	Doctoral Dissertation	Jan 2003 — Mar 2006

4. TITLE AND SUBTITLE

Assessing the Potential for Improved
Scramjet Performance Through Application of
Electromagnetic Flow Control

5a. CONTRACT NUMBER

5b. GRANT NUMBER

5c. PROGRAM ELEMENT NUMBER

6. AUTHOR(S)

Lindsey Martin F., Maj, USAF

5d. PROJECT NUMBER

2003-014

5e. TASK NUMBER

5f. WORK UNIT NUMBER

7. PERFORMING ORGANIZATION NAME(S) AND ADDRESS(ES)

Air Force Institute of Technology
Graduate School of Engineering and Management (AFIT/EN)
2950 Hobson Way
WPAFB OH 45433-7765

8. PERFORMING ORGANIZATION REPORT NUMBER

AFIT/DS/ENY/06-05

9. SPONSORING / MONITORING AGENCY NAME(S) AND ADDRESS(ES)

AFOSR/NA
Dr. John Schmisseur
801 N. Randolph Street, Rm 732
Arlington, VA 22203-1977 (703) 696-6962

10. SPONSOR/MONITOR'S ACRONYM(S)

11. SPONSOR/MONITOR'S REPORT NUMBER(S)

12. DISTRIBUTION / AVAILABILITY STATEMENT

Approved for public release; distribution unlimited.

13. SUPPLEMENTARY NOTES

14. ABSTRACT

Hypersonic flight using scramjet propulsion bridges the gap between turbojets and rockets. Recent efforts focus on magnetogasdynamic (MGD) flow control to mitigate the problems of high thermomechanical loads and low efficiencies associated with scramjets. This research is the first flight-scale, three-dimensional computational analysis of a realistic scramjet to assess how MGD flow control improves scramjet performance. Developing a quasi-one dimensional design tool culminated in the first open source scramjet geometry. This geometry was tested with the Air Force Research Laboratory's electromagnetic computational code. To increase fidelity, an algorithm was developed to incorporate thermochemistry, resulting in the only open-source model of combustion in an MGD controlled engine. A control volume analysis with electron beam ionization was presented for the first time with this approach. Local MGD control within the inlet affected drag and heat transfer and was marginally successful in raising combustor inflow pressure. MGD acceleration to increase flow momentum was effective at improving flow into the scramjet's isolator. Combustor-based MGD generators proved superior to inlet generators with respect to power density and engine efficiency. MGD acceleration was ineffective in improving performance with all the MGD engines having approximately 33% more drag than baseline and none of them achieving self-powered operation.

15. SUBJECT TERMS

Supersonic Combustion Ramjet Engines, Magnetogasdynamics, Computational Fluid Dynamics, Hypersonic Vehicles

16. SECURITY CLASSIFICATION OF:			17. LIMITATION OF ABSTRACT	18. NUMBER OF PAGES	19a. NAME OF RESPONSIBLE PERSON
a. REPORT	b. ABSTRACT	c. THIS PAGE			Richard J. McMullan (ENY)
U	U	U	UU	176	19b. TELEPHONE NUMBER *(include area code)* (937) 255–3636, ext 4578